UNIVERSITY OF SOUTHAMPTON

Faculty of Engineering and Physical Sciences
School of Physics and Astronomy

Gamma-Ray Imaging with Coded Masks

Volume 1 of 1

by

Alessandra Costantino

Master of Science

ORCiD: 0000-0001-8585-9196

A thesis for the degree of
Doctor of Philosophy

June 2023

University of Southampton

Abstract

Faculty of Engineering and Physical Sciences
School of Physics and Astronomy

Doctor of Philosophy

Gamma-Ray Imaging with Coded Masks

by Alessandra Costantino

Coded masks are frequently used imaging techniques for imaging in X- and gamma-ray astronomy. Instead of traditional optics, coded mask telescopes use a heavy metal plate with a pattern of apertures which modulate the incoming radiation, which is then recorded by a position sensitive detector. A map of the sky is then obtained by decoding the detector image, normally by means of cross-correlation. The technique is designed to operate with static pointings, during which an image of the mask is accumulated on the detector. In this thesis an alternative method of reconstruction is proposed where each detected photon is projected back to all the regions of the sky that it may have originated from. This photon-by-photon approach allows the production of images even when the telescope is moving. This thesis presents the sky maps obtained applying the back-projection method to a prototype data set collected by INTEGRAL/ISGRI during slews in a 10 orbit period in October 2010. Analysing the entire INTEGRAL slew data set would permit the use of approximately 65Ms of data so far unexplored observations. Production of all-sky maps, source lists and flux-calibrated light-curves have all been demonstrated. The second part of this thesis applies the same back-projection method to near-field medical gamma-ray imaging. Medical imaging could benefit from the high sensitivity that coded aperture images have demonstrated in astronomy, overcoming limitations imposed by collimators. Furthermore, the intrinsic depth perception of coded mask cameras makes it possible to obtain 3D images of a source distribution with just one or two views. A 3D near-field coded mask camera was designed, assembled and tested. The back-projection algorithm was applied to data obtained with isotopes typically used in nuclear medical imaging. Coded-mask medical imaging systems have the potential to reduce the scan time or patient dose and the footprint of the scanning systems. The successful reconstruction of multiple point sources and extended sources with a large field of view using two simultaneous camera views was demonstrated.

Contents

List of Figures

List of Tables

Declaration of Authorship

I declare that this thesis and the work presented in it is my own and has been generated by me as the result of my own original research.

I confirm that:

1. This work was done wholly or mainly while in candidature for a research degree at this University;
2. Where any part of this thesis has previously been submitted for a degree or any other qualification at this University or any other institution, this has been clearly stated;
3. Where I have consulted the published work of others, this is always clearly attributed;
4. Where I have quoted from the work of others, the source is always given. With the exception of such quotations, this thesis is entirely my own work;
5. I have acknowledged all main sources of help;
6. Where the thesis is based on work done by myself jointly with others, I have made clear exactly what was done by others and what I have contributed myself;
7. Parts of this work have been published as:

   Costantino, A. ; Bird, A.J. (2019). *Constructing an IBIS/ISGRI Slew Survey*, Proceedings of 12th Integral Conference

   Costantino, A. ; Bird, A. J. ; Schuffham, J. ; Guy, M. (2022) . *A Back-Projection Approach to Coded Aperture Imaging for SPECT Applications* , Proceedings of SPIE Medical Imaging 2022, DOI : 10.1117/12.2610979

Signed:..... Date:.....

Acknowledgements

I would like to thank my supervisor Prof. Tony Bird for giving me the opportunity to move to the UK to study for a PhD. Your support throughout the project has been invaluable and you were always ready to give a word of encouragement, a piece of advice, or a healthy dose of English humor whenever it was needed.

I would like to thank Symetrica, for collaborating with us in the preparation and execution of the tests on the 2V-CAM. Special thanks to Ian Della Rocca, for his help with the data acquisition software used in the experiments. Thank you to the nuclear medicine departments of the Royal Surrey County hospital and the Southampton General Hospital. The space and resources provided by these hospitals to carry out enabled the experimental testing of 2V-CAM. The technical and scientific support of the hospital staff was of great help during testing. I Special thanks to James Schuffham from Royal Surrey County Hospital and Gemma Lewis and Timothy Melhuish from Southampton General Hospital for the preparation and handling of the experimental test samples.

Thank you to the mechanical workshop of the Physics Department at University of Southampton for the technical support in all the stages of 2V-CAM design.

I would like to thank my family, and especially my parents, for being the safe place I could always call home during this difficult journey. I can't imagine how hard it is to see your child move to a different country to pursue their dream career, but you have never failed to show me unwavering and unconditional support.

Thank you Ed for inspiring me to always be curious, keep learning new skills and take on new projects. I have always admired your thirst for knowledge in such a broad range of topics and it has truly changed the way I view Science and Technology. Thanks also for all the help and support during my PhD. It has been a long journey, but you never stopped believing in me even when I was doubting myself.

Finally, I would like to thank the Astronomy department of the University of Southampton and especially my fellow PhD students. Moving to another country is never easy, but you have welcomed me like a second family and I have learned so much from each and every one of you.

To Stefano

Definitions and Abbreviations

CT	Computed Tomography
ET	Emission Tomography
FCFOV	Fully Coded Field of View
FOV	Field of View
FWHM	Full Width at Half Maximum
GTI	Good Time Interval
IJD	Integral Julian Date
LOR	Line of Response
MJD	Modified Julian Date
MURA	Modified Uniformly Redundant Array
OSA	Off-Line Scientific Analysis
PCFOV	Partially Coded Field of View
PIF	Pixel Illumination Fraction
PPM	Photon-by-Photon Mode
PSF	Point Spread Function
PSLA	Point Source Location Accuracy
SACF	Self Auto-Correlation Function
scw	science window
SPECT	Single Photon Emission Computed Tomography
SPP	Single Pixel Projection
SPV	Single Pixel Variance
URA	Uniformly Redundant Array

Chapter 1

Introduction

1.1 High Energy Astrophysics and Coded Mask Telescopes

1.1.1 The sky in the X-rays and gamma-rays

Observation of the sky in the X-ray and gamma-ray bands has had a fundamental role in the discovery and understanding of some of the most extreme physical phenomena in our Universe. High energy electromagnetic radiation is emitted by a variety of celestial objects, through distinct processes and mechanisms.

X-ray Binary Systems

A great number of sources in the X-ray sky are composed of accreting binary systems. These systems consist of a star gravitationally bound to a compact object, which is usually a neutron star or a black hole. The compact object acquires mass from the star, which is normally a main sequence star or, in some cases, a red giant. According to the mass and spectral type of the star, which is also referred to as donor, binary systems are divided into two broad classes: high mass X-ray binaries (HMXBs) contain a young companion of spectral type O or B with mass greater than 8 solar masses. Low mass X-ray binaries (LMXBs) instead have a donor which is of spectral type later than B and with mass less than two solar masses. In HMXBs the mass transfer occurs mainly via stellar wind. The donor start emits stellar wind driven by the radiation pressure while the compact object captures a fraction of the wind and converts the potential energy of the accreted matter, composed of plasma, into X-rays. LMXBs accrete matter mainly through Roche lobe overflow of the donor star, which creates an accretion disk around the compact objects. Both neutron star

and black hole binary LMXB present an X-ray spectral continuum that can be modeled with the sum of two components: a thermal component which dominates under 10 keV, and a non thermal component, which dominates at higher energies. The first component, also called 'soft component' results from the accumulation of matter onto the central object under its gravitational pull. The accretion material forms an optically thick disk around the central object. The viscous forces present in the accreting material dissipate the heat and the radiation emission from accretion can be modeled with a black body spectrum from the surface of the disk. Neutron star systems may show a second black-body component emitted from the neutron star surface. The second component is harder and normally modeled with a power-law and is thought to be due to non-thermal emission from a comptonized corona around the compact object. Binary systems are believed to go through different spectral states which affect the relative importance of the two components.

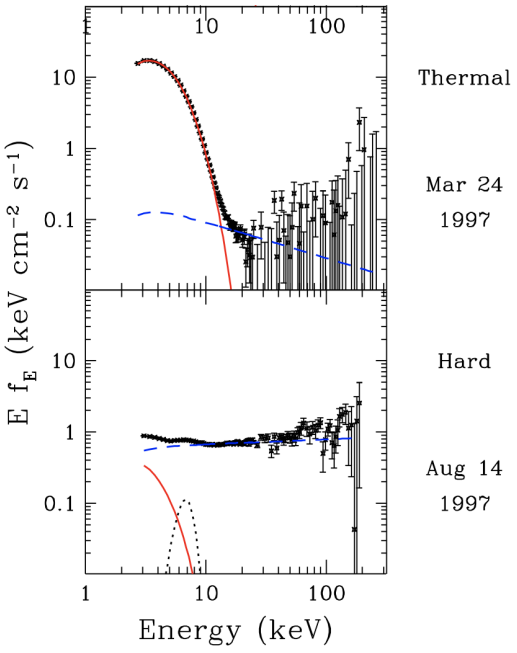

FIGURE 1.1: Sample spectra of black-hole binary GRO J1655–40 illustrating two outburst states: thermal and hard (1). Historically these states are also denoted as 'high' and 'low'. These names reflect the flux up to 10 keV, because the first observations were carried out exclusively in this band

1.1 shows, as an example, the X-ray spectra of the black-hole X-ray binary GRO J1655–40 measured by the Rossi X-ray Timing Explorer (RXTE) NASA telescope and published by Remillard and McClintock (1) The source was observed going through different states. The spectrum was modeled with a thermal component (red, solid

line) and a power-law component (blue, dashed line). A Fe Kα line originating from the accretion flow is also necessary to model the spectrum. The relative importance of the different components varies over time as the source goes through different states. Observation of X- and gamma-ray emission from binary systems provides insight into the accretion mechanisms and the environment in the innermost regions of the accretion disk (2).

Active Galactic Nuclei

Active Galactic Nuclei (AGN) are also very commonly observed in the X-ray and gamma-ray bands. AGN encompass several types and classes of galaxies, sharing a key feature, which is the presence of a supermassive black hole at their centre. All active galaxies have an extremely bright central region, outshining the stellar emission from the rest of the galaxy. AGN emit radiation across the spectrum, ranging from radio to gamma-ray wavelengths. The mechanism believed to be the main source the continuum emission with energies up to X-rays and gamma-rays observed in AGN is non-thermal and called synchrotron-self-Compton. High energy electrons from plasma in the inner regions of the accretion disk radiate synchrotron photons under the effect of the magnetic field of the central black hole. The same population of electron then upscatters the synchrotron photons to high energies through inverse Compton processes. The high energy cutoff of the inverse Compton spectrum depends on the temperature of the plasma in the accretion disk and the energy distribution of the electrons. The photons emitted in AGN with this mechanism are observed up to energies between a few hundred keV and TeV energies. Figure 1.2 shows the spectrum of a very well known AGN, Markarian421, sampled at different stages of an outburst happened in February 2017. The spectrum clearly shows the two components: the synchrotron emission at lower energies and the inverse Compton at higher energies. The spectra, publised by Banerjee et al. (3), show how the change flux influence the spectral shape of the source. This implies that the environment of the accretion flow in proximity of the central black hole have an effect on the AGN emission in all wavebands. Observation at different energies, including X-rays and gamma-rays is crucial to a better understanding of extreme phenomena occurring close to the central engine of AGN (2)

Supernovae and Supernova Remnants

Supernova (SN) explosions are also responsible for the emission of X-rays in different stages of their formation. In the expanding stage of the SN the material originating from the precursor and the interstellar matter are heated by the shockwave. This generates hot plasma which reaches temperatures over 10^6K and emits

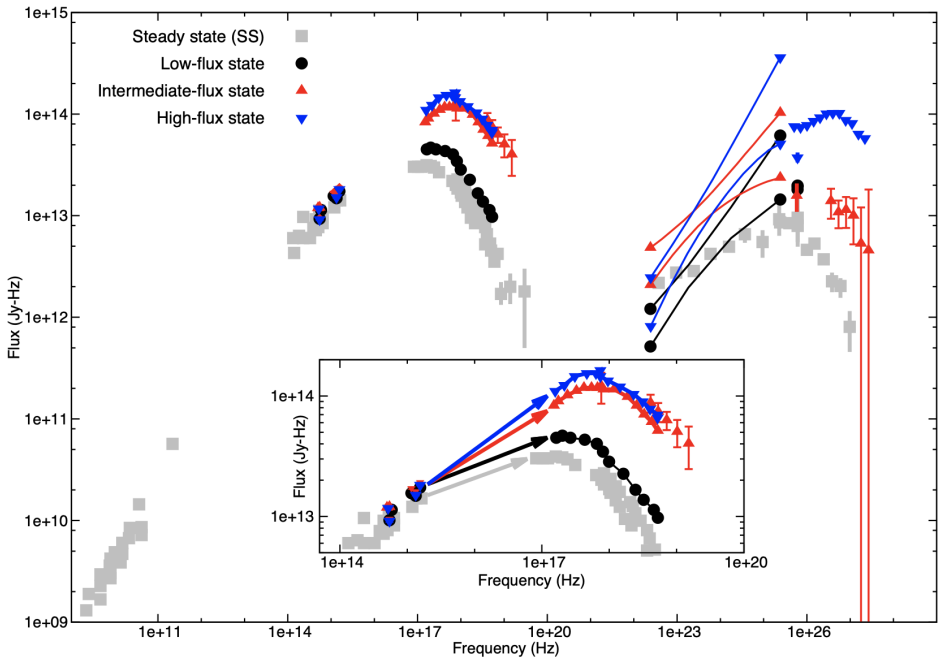

FIGURE 1.2: Multi-wavelength spectrum of the TeV AGN Markarian421 during different phases of an outburst: square (grey)– steady state data, circle (black) low-flux state, triangles (red) intermediate-flux state, inverted triangles (blue) high-flux state. A spectral hardening can be seen in X-ray and TeV bands as the source became brighter, highlighting the connection between variations in observed flux and spectral shape (3)

.

brehmsstralung radiation in the X-rays. High energy radiation from shells of SN remnants is observable for thousands of hundreds of years after the explosion. SN remnants are also visible in the gamma-ray band at extreme energies above a few TeV. The emission of very high energy gamma-rays is believed to be generated by high energy electrons interacting with the X-ray photons via inverse Compton scattering, and decay of neutral pions created the supernova shell. In addition, immediately after the SN explosion, it is possible to observe radioactivity produced in the explosive nucleosynthesys. The end product of the thermonuclear reactions occurring in the nucleus in of the Supernova progenitor is ^{56}Ni. ^{56}Ni emits gamma-rays via electron capture to ^{56}Co with a half-life of 6.1 days. ^{56}Co then undergoes β decay to ^{56}Fe: with a half life of 77 .1 days.

$$^{56}Ni + e^{+} \rightarrow ^{56}\ Co + \gamma \text{ and then } ^{56}Co + e^{+} \rightarrow ^{56}\ Fe + \gamma \tag{1.1}$$

Characteristic lines of ^{56}Co at 1238keV and 647keV are only visible for a few months after the SN explosion, after the envelope of the supernova became transparent to gamma-rays. Observations of SN and SN remnants in the X- and gamma-rays have

been crucial to refine our understanding final stages of the life cycle of a star, as well as the physical phenomena that occur during and after the explosion of a SN (2).

Gamma-ray Bursts

Gamma-ray bursts (GRBs) are brief bursts of high-energy radiation that appear apparently at random in the sky, emitting the majority of their energy above 0.1 MeV. GRBs have been one of the unsolved mysteries in astrophysics for a long time. These phenomena are divided into two broad categories according to their duration. The short gamma-ray bursts, only lasting a few seconds, have been associated to the supernova explosion of an extremely massive but metal poor stars. Long GRB, of the duration of tens to hundreds of seconds, have been connected to extremely violent events such as neutron star-neutron star, black hole-neutron star, or black hole-black hole mergers. This connection was confirmed after the observation of a GRB which occurred less than two seconds after a gravitational wave detection by the gravitational wave observatory LIGO. The GRB was detected independently and simultaneously by the gamma-ray telescopes INTEGRAL-SPI and FERMI-GBM, providing evidence of the association between the two phenomena. Follow-up observations at lower energies revealed that the event was originated by the merger of two neutron starts. Surveying the sky in the gamma-rays was crucial to validate the models behing GRB events (**?**)

1.1.2 Observing the sky in X-ray and gamma-ray bands

Observations of the sky in the high energy bands are essential to probe the regions where radiation emission took place and constrain the parameters of the models for the physical processes involved in some of the most extreme environments in our Universe. Figure 1.3 shows a plot representing the atmospheric transparency for photons of different energies. The blue line represents the altitude at which 50% of the incoming radiation is absorbed. Astronomical observation in the X-ray and gamma-ray bands is not possible on earth due to the high atmospheric absorption of photons at these energies. As a consequence, the detection of high energy photons has been performed with several generations of telescope-based instruments.

In the early days of X-ray astronomy (up to the 80s) sky surveys were extremely limited in scope and often accomplished by 'drift scans' where a collimated instrument was mounted on a satellite, which was moved slowly across the sky, and the presence of sources was inferred by determining the times when the count rate in the detectors increased. These scans were achieved by allowing the telescope aperture

slit to drift slowly across the sky, often using a spinning satellite and orbital precession to map the whole sky. Slew/drift surveys of this kind were very inefficient as the instrument had to be heavily collimated to provide good imaging and so only the brightest sources could be detected, and the point spread function (PSF) was often asymmetric as source location was only possible along the drift/spin axis of the spacecraft. As an example, the NASA mission HEAO 1 carried a gamma-ray instrument with this type of imaging techniques(4), as well as the ARIEL V satellite(5). Both missions were carried out in the 70s and 80s. Building a sky map could take several years and spacecraft re-orientations meant each source was 'visited' only once or twice, making variability studies virtually impossible.

True X-ray imaging capabilities, with angular resolution down to less than one arcsecond, was achieved for the first time by telescopes with grazing incidence optics like XMM-Newton(6) and Chandra(7). Grazing incidence systems are characterised by a field of view narrower than one degree and are ideal for detailed studies of known sources, but impractical for sky surveys. The best example of the type, the ROSAT All Sky Survey, covered the whole sky and was very successful, but actually provided very limited exposure of approximately 400s on average at each point on the sky(8). Moreover, grazing incidence imaging is only efficient at relatively low energies because of the absorption of X-rays in the reflecting material. The NuSTAR mission has extended the technique to $\sim$80 keV but even at that energy the reflectivity is only 10% of the nominal levels, seriously impacting the telescopes' throughput (9). In 2009 the Monitor of All-sky X-ray Image (MAXI) mission was installed on the International Space Station. Equipped with two different types of slit cameras, MAXI is able to provide an all-sky image of X-ray sources above 20 mCrab in approximately 90 minutes (one ISS orbit), with a source location accuracy down to 0.1°. The key objective of the mission is all-sky monitoring, for transient alert and creation of an unbiased X-ray source catalogue (10)

Between 100 keV up to approximately 100 MeV it is possible to produce images of the sky with telescopes equipped with appropriately designed coded aperture (or coded mask) cameras. These types of telescope use the opacity to gamma-rays of high Z material to produce shadows of a specific pattern on a detector plane. In many ways these appear to overcome all the limitations of the systems described above. They can offer a wide field of view which is ideal for sky surveys where the multiplex advantage allows many sources to be studied at once. Typically instruments of this type have fields of view with areas 100x larger than the grazing inicidence ones. Coded apertures also offer much higher throughput from the imaging system - typically 50% throughput which is much higher than can be achieved with a collimated system (although not as good as the best grazing incidence system might do at lower energies). The 'cost' of coded aperture systems is that they require

complex and expensive imaging detector planes as they rely on spatial modulation of the input flux, whereas scan/drift surveys used temporal modulation and really simple detectors. Coded mask gamma-ray imagers have had a great success in X-ray and gamma-ray astronomy and their use is established for observations in the 10 keV -10 MeV range. Two X/gamma-ray missions that mount coded-mask telescopes as their primary instrument were launched in the early 2000s and are still currently operational: Swift, with its Burst Alert Telescope BAT (11), and INTEGRAL (INTErnational Gamma-Ray Astrophysics Laboratory) (12) which has three coded mask instruments on board: IBIS, SPI and JEM-X. The advantages of coded-aperture imaging for surveys in the hard X-ray band have been clearly demonstrated by the INTEGRAL and Swift missions as a result of the high sensitivity provided by their imaging systems. These missions have increased the numbers of sources we know in the hard X-ray sky by orders of magnitude and also allow variability of sources to be studied in detail. In 2015 the Indian Space Research Organization Launched the Astrosat mission which include, in addition to several soft X-ray instrument, the coded mask camera CZTI (Cadmium–Zinc–Telluride Imager), sensitive in the 20 - 100 keV energy range (13).

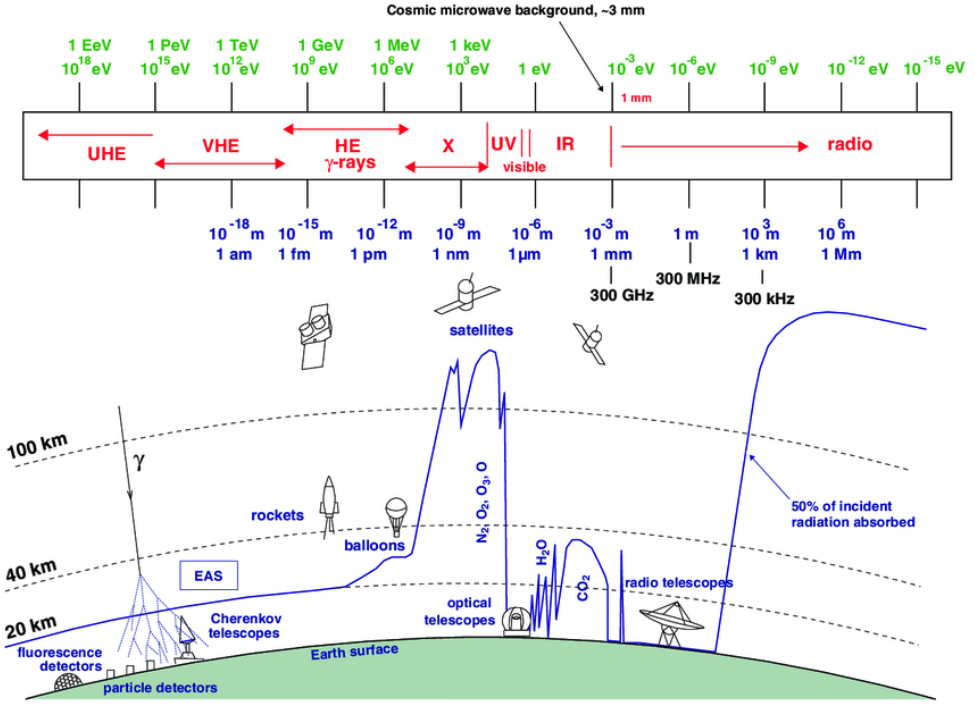

FIGURE 1.3: Atmospheric transparency for different wavelengths. The continuous line indicates the height at which a detector can receive 50% of the incoming radiation. Since X-rays and gamma-rays are absorbed by the atmosphere, satellite observations are needed to study objects emitting in these bands (2)

Above $\sim$ 10 MeV gamma-rays are too energetic to be absorbed by a few cm thickness of heavy material, and other physical processes need to be used to detect high energy photons from astronomical sources and reconstruct their origin. For example,

Fermi Gamma-ray Space Telescope (14) uses $\gamma \rightarrow e^+e^-$ conversion to observe the sky between 20 MeV and 300 GeV. At even higher energies ground based telescopes like H. E. S. S. or VERITAS (15) are used to observe the Cherenkov emission from the products of the interaction between the gamma photons and the atmosphere and indirectly reconstruct the characteristics of the incoming photon. Both telescopes have a large field of view and are designed to monitor the sky to detect and identify different types of gamma-ray sources and trigger observations in their counterparts in other wavelengths.

This thesis examines two new applications of coded aperture imaging which relate strongly to the ways in which X-ray astronomy has evolved. Traditionally, coded aperture telescopes have relied on a stabilised platform to allow the telescope to accumulate a statistically valid shadow of the aperture pattern, which means that they cannot work on moving platforms, or image targets that move. But a coded aperture is a form of collimator, so why should it not be used as a modulator for a drift/scan survey too? In principle, the requirement is actually not for stable pointing, just of a precise knowledge of the telescope orientation at the moment each photon arrives.

The first application demonstrates that a photon-by-photon reconstruction can be used to image with a coded aperture even when source and/or camera is moving. In this approach the methodologies of both temporal and spatial modulation are combined as described in chapter 3. This thesis applies this method to the dataset accumulated by INTEGRAL/IBIS during the telescope slews (where it is moving between pointings). This corresponds to a 'free' data set that has been collected over the course of INTEGRAL mission but not explored previously as it cannot be analysed using standard methods. We demonstrate how a sky survey could be constructed using just slew data, although in practice the science will be optimised when the slew and pointing surveys are combined, due to the way the mission is operated.

In the second application, we note that the majority of medical imaging methods still rely on heavily collimated imaging systems with extremely low throughput. If the collimator can be replaced by coded apertures, as it has been in astronomy, the potential benefits in terms of system sensitivity are enormous. This application is discussed in chapter 5. We raise the intriguing possibility that a single coded aperture imager is capable of reconstructing a source distribution in 3D when used for near-field imaging. While this is true, the PSFs generated are asymmetric (just as the astronomy drift-scan ones were) and we demonstrate that imaging is greatly improved by the use of a dual-view imaging system. The develop of this system and results from early trials in a clinical setting are detailed in chapters 6 and 7. In principle, these two advances may one day be combined, with the possibility

of a hand-held medical imager that provides real-time imaging for use in surgery without the need for a stabilised platform.

1.2 Principles of Coded Mask Imaging

Producing images of gamma-ray sources is particularly challenging because photons with energies above 100 keV can not be reflected (and then focused on a detector to produce an image) even with special optics like grazing incidence optics. As a consequence, alternative techniques, which do not require reflection, are required. Pinhole cameras, for examples, can produce gamma-ray images, but present a compromise between the signal to noise ratio (SNR) and the angular resolution of the system. The SNR improves with the size of the pinhole, while the angular resolution is made worse as the pinhole diameter increases. The idea of using random pinhole arrays for X-ray and gamma-ray imaging was first put forward by Dicke (16), who suggested that the use of multiple pinholes could improve the SNR with respect to a single pinhole camera, while maintaining its angular resolution. On the other hand, the image needs to be decoded to be intelligible, since it is made by the overlap of several single pinhole images. Fenimore and Cannon (17) theorized the use and image reconstruction techniques of what today is known as coded mask cameras. A coded mask (or coded aperture) is a modulating patterns of open and closed "pixels" placed in front of a detector, instead of multiple and randomly positioned pinholes. Figure 1.4 represents a diagram of an imaging system based on coded masks. An X-ray or gamma ray source emits radiation, which is modulated by a mask made of a heavy absorbing material like tungsten (Z=74) or lead (Z=82) before reaching a position sensitive detector which in figure 1.4 is represented on the left.

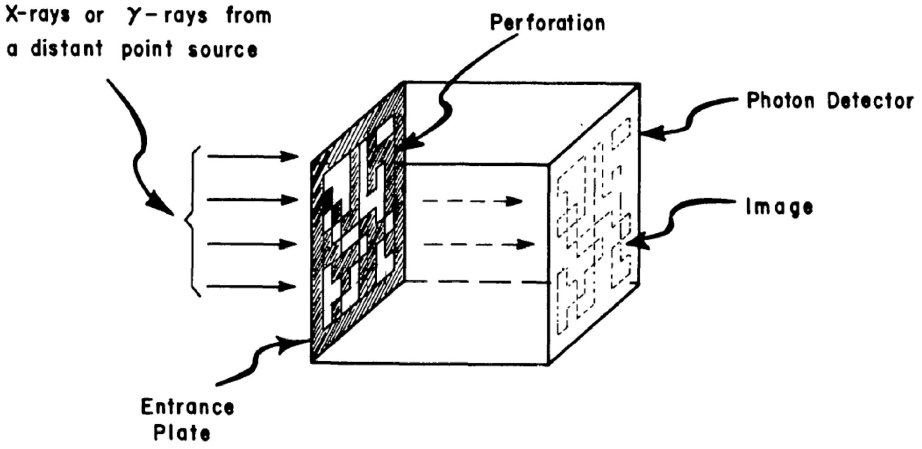

FIGURE 1.4: Schematic representation of a coded aperture imaging device(16). Radiation incoming from the left side of the image is modulated by a perforated plate of heavy material before being recorded by a position sensitive detector

The detector image recorded by a coded mask camera is called a shadowgram and it is the shadow that the mask casts onto the detector plane. The shadowgram needs to be reprocessed in order to locate gamma-ray sources and produce a recognizable image. The advantages of this imaging technique reside in the improved SNR with respect to a single pinhole camera, making it suitable for high energy applications in astronomy, while maintaining its angular resolution. Coded mask telescopes also have a large field of view, allowing the monitoring of large areas of the sky.

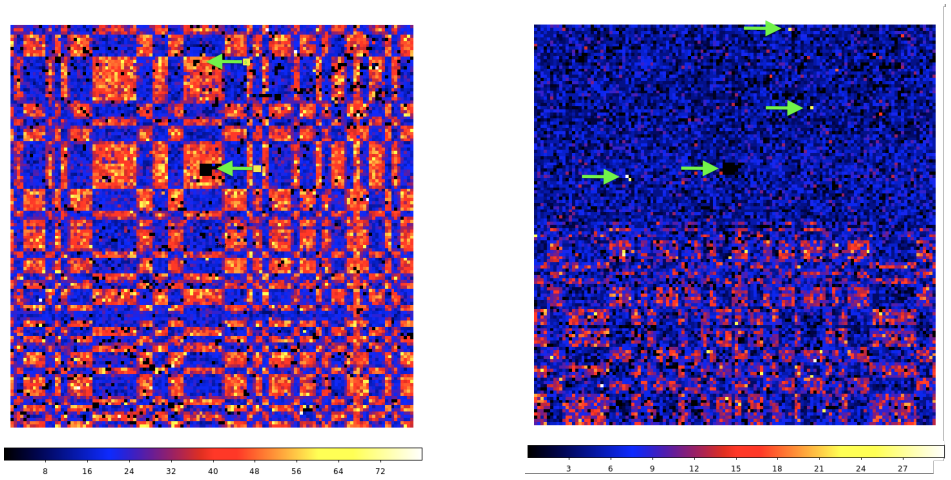

FIGURE 1.5: INTEGRAL/IBIS examples of shadowgrams collected during an observation of the Crab in the FCFOV (left, from science window 017000780010) and in the PCFOV (right, science window 017000970010). The partial illumination of the detector plane is visible in the second shadowgram. Both images show, highlighted with green arrows, pixels (or groups of pixels) that have an abnormally high or low number of counts compared to their neighbours. These pixels are either inactivated during the observation, or subject to electronic noise. Treatment of inactive and noisy pixels in the image processing is described in section 2.2

1.2.1 The Field of View

The field of view (FOV) of a coded aperture camera is defined as the range of angles through which radiation can be collected by the detector and used to produce an image. In other words, the FOV represents the extent of the region of space observable by a given imaging system. In the particular case of the imager being a coded mask camera, the level of information encoded by the mask depends on the position and varies considerably within the FOV. To account for these variations, the FOV of coded mask instruments is divided into two regions. Radiation sources in the fully coded field of view (FCFOV) illuminate the whole detector plane with encoded flux, while sources in the partially coded field of view (PCFOV) only project the mask pattern on a part of the detector. This effect is shown the shadowgrams in figure 1.5, which were recorded when the Crab was in different positions of the FOV. The image on the left shows the detector histogram of an observation with the

Crab in the FCFOV. The whole detector shows the mask pattern. The image on the right, on the contrary, was acquired during an observation when the Crab was in the PCFOV, in which the shadow of the mask only shows on approximately half of the detector plane.

Including the PCFOV in the final images of a telescopes forms a bigger field of view but as a result of the partial use of the detector plane and the consequent lower number of counts, the imaging performance in the PCFOV is lower compared to the FCFOV. Figure 1.6 shows the cross-section of a coded mask systems. The blue arc defines the angles delimiting the FCFOV. Sources within this angle project a shadow of the mask over the full detector plane. The red arc, on the other hand, shows the angular size of the PCFOV. Sources at outside the FCFOV but within the FCFOV cast a shadow of the amask on paret of the detector plane. The sizes of the FCFOV and PCFOV are defined by the angles:

$$FCFOV = 2 \arctan \frac{L_M - L_D}{2MD} \tag{1.2}$$

$$PCFOV = 2 \arctan \frac{L_M + L_D}{2MD} \tag{1.3}$$

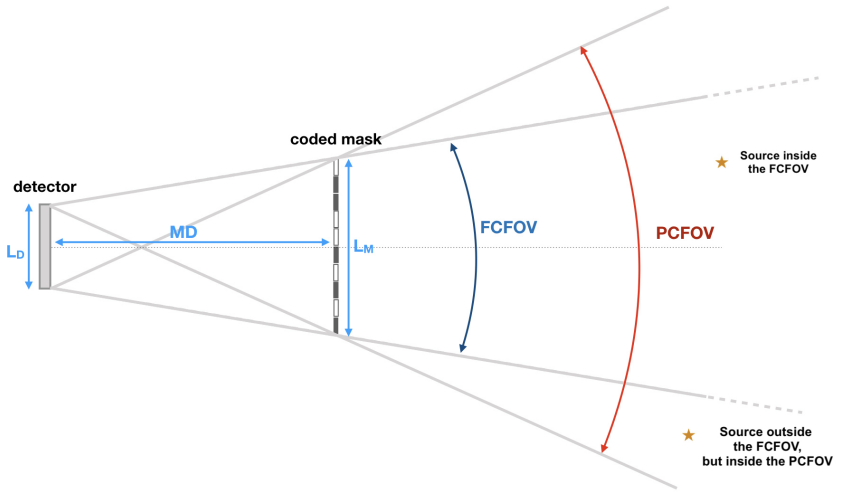

FIGURE 1.6: One dimensional diagram of a coded aperture imaging system. The partially coded field of view, shown in blue, is larger than the fully coded field of view, shown in red

1.2.2 The Angular Resolution

The angular resolution of a coded mask system depends on the distance between the mask and the detector and the size of the detector pixel. If p_m identifies the size of the mask pixel, the angular resolution ϕ can be calculated as

$$\phi = \arctan \frac{p_m}{MD} \tag{1.4}$$

with reference to figure 1.7. It is worth noting that the detector resolution also comes into play in the design of real coded mask systems. The detector pixelisation must be sufficiently fine enough to sample the expected features of the shadowgram. However, it has been demonstrated that pushing the sampling factor to very high values does not always represent an advantage, since the sensitivity with respect to the ideal case already saturates at values between two and three(18; 19).

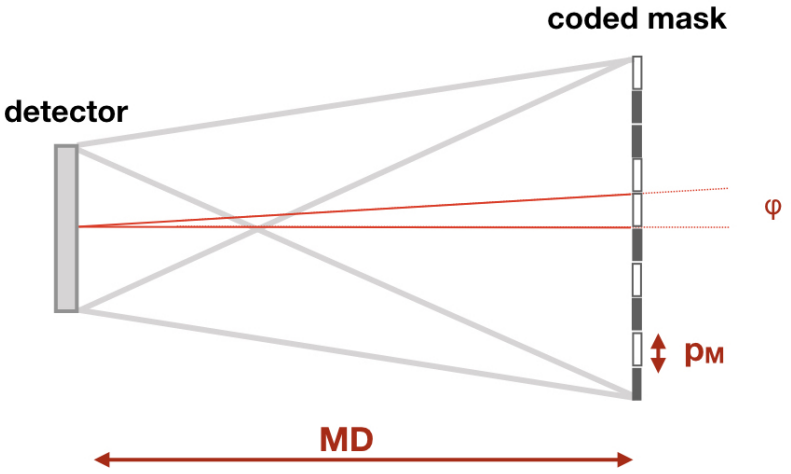

FIGURE 1.7: The angular resolution of a coded mask telescope is defined as the ratio between the size of a mask pixel and the mask to detector distance. MD is the mask to detector distance, p_m is the size of the mask pixel. The angular resolution of a telescope can be improved by either increasing MD or reducing p_m.

1.2.3 Image Reconstruction by Cross-Correlation

The coded aperture can be expressed as a matrix A

$$A_{i,j} = \begin{cases} 0 & \text{if the mask pixel is closed} \\ 1 & \text{if the mask pixel is open} \end{cases} \tag{1.5}$$

If the emitting object is expressed by the matrix O in the source plane,

$$O_{i,j} = \begin{cases} 0 & \text{if pixel } i,j \text{ does not emit photons} \\ 1 & \text{if pixel } i,j \text{ emits photons} \end{cases} \tag{1.6}$$

the image P on the detector plane is given by

$$P = (O * A) + N, \tag{1.7}$$

where $*$ is the correlation between the matrices O and A, defined as

$$(O * A)_{i,j} = \sum_{k,l} O_{k,l} A_{i+k,j+l} \tag{1.8}$$

N is a noise term that represents the contributions to the background that are not modulated by the mask, such as detector noise or, in case the camera is mounted on a telescope, cosmic penetrating through the shielding material. Correlation methods for the image reconstruction consists of seeking a decoding array G, such that

$$O' = P * G = O * A * G + N * G, \tag{1.9}$$

G is chosen so that $A * G$ has optimal properties for the image reconstruction. Ideally, the image would be perfectly reconstructed if $A * G$ is a δ function and $N * G$ is 0.

1.3 Coded Mask Designs

In general, $A * G$ will not be a delta function for any modulating pattern. An effective way to measure the efficiency of a coded mask in producing images that are really close to the real source distribution is given by its periodic spatial autocorrelation function (SACF). The SACF is computed as the cross-correlation between a basic mask pattern onto a mosaic of itself. The SACF of a perfect mask should assume its maximum value in a position of perfect registration, and be equal to 0 in all other positions (the side lobes). The only 'coded mask' that would meet this requirements is essentially a single pinhole. Very good compromises, however, can be reached with coded masks that present a SACF with constant side lobes. In this case, in fact, the image background level is constant and can be artificially removed with appropriate techniques known as 'balancing', which will be described in section 1.4.

1.3.1 Random Mask Patterns

A random mask pattern is a coded mask where holes are placed at random. The deconvolution array of random patterns is the mask pattern itself, so that $G = A$.

Figure 1.8 represents a random mask pattern and its computed SACF. The SACF of a random pattern presents sidelobes are on average flat, with fluctuations that reflect the random nature of the mask. This means that, for a random array, the SACF presents sidelobes that are on average flat. Figure 1.9 shows a picture of the SWIFT/BAT random coded aperture, which has a semi-circular shape.

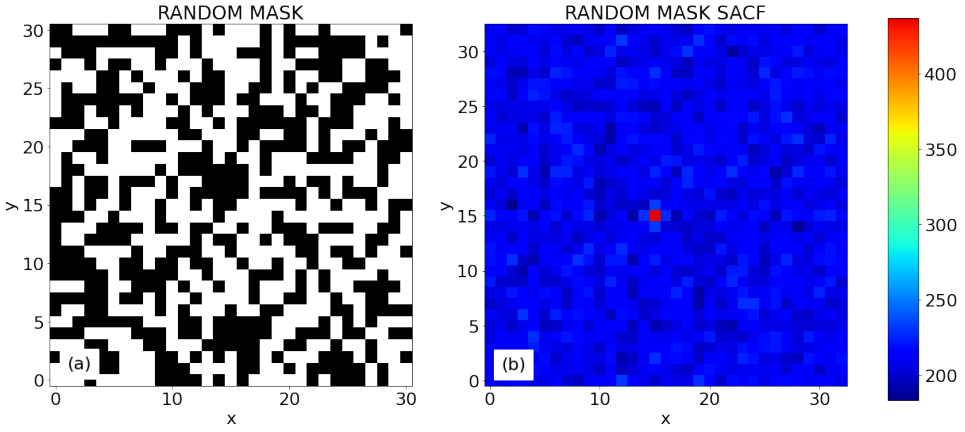

FIGURE 1.8: Random coded mask pattern (left) and its SACF (right). The position of perfect registration is evident at the centre of the SACF. The background of the cross-correlation image have features that derive from the randomness of the mask pattern

FIGURE 1.9: A picture of the semi-circular coded mask of SWFT/BAT inspected by a technician taken from the mission website (20). One of the advantages of using a random pattern is the possibility to use differently shaped masks, which permit more flexibility in the design of the instrument and how it is mounted onto the satellite

1.3.2 Non-Redundant Arrays

Non-Redundant Arrays (NRAs) form a set of coded mask pattern with interesting imaging properties. Their name is due to the fact that, in non redundant patterns, the separation between each pair of holes in the pattern is non redundant, i.e. does not repeat. Figure 1.10 shows an example of a non-redundant array constructed by L.E. Kopilovich (21). In the original paper, the coded mask is represented by a 19x19 matrix, and the open pixels are represented by black dots. By observing the pattern,

it is possible to notice that there is only one pair of openings that are adjacent, one pair of openings that is separated by two closed pixels, etc. It is important to specify that, in this context, the word 'distance' is used improperly. What is actually non-redundant are the spacing vectors between pairs of holes. This property of NRA leads to optimal features in the SACF. In fact, the SACF would show a central peak, with a height equal to the number of open pixels in the mask. All the other positions in the SACF assume value not greater than 1 (21). The main drawback of this family of patterns is the small number of holes, that results in a low transmission, usually around 15%.

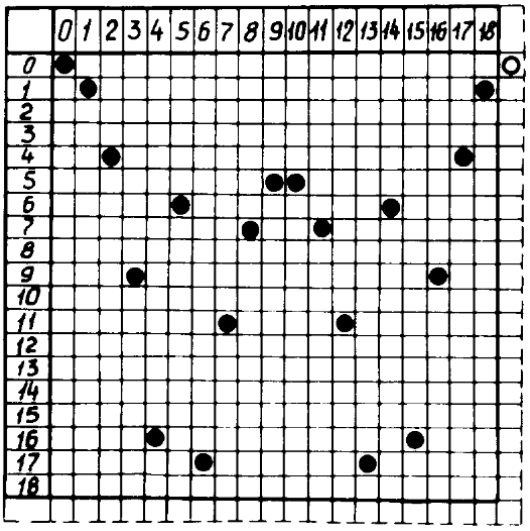

FIGURE 1.10: A non-redundant array constructed by L.E. Kopilovich(21). The spacing vectors between the pairs of open elements are all different, resulting in optimal properties for the SACF

1.3.3 Uniformly Redundant Arrays

The Uniformly Redundant Arrays (URAs) are a particular subset of the NRA that has a SACF with constant side lobes. The design is based on cyclic difference set theory (22). Cyclic difference sets are sequence of numbers built so that the separation between each pair of numbers of the sequence occurs a constant number of times. Once these sequence are folded into 2D arrays, they offer mask patterns where all separations between pairs of holes occur a constant number of times. The full construction of these patterns from cycling difference set theory can be found in the 1978 paper by Fenimore(17). For the purpose of this thesis it will be only highlighted that, due to the nature of cyclic difference sets, URA patterns generate mask arrays of $p \times q$ shape, where p and q are prime numbers such as $p - q = 2$. The deconvolution array G is a mosaic of a basic URA pattern of chosen size $p \times q$. This

type of pattern has been mounted on the hard X-ray telescope on board the Indian mission AstroSat(13).

1.3.4 Modified Uniformly Redundant Arrays

A modified version of the URA designs, always based on cyclic difference set theory, allows applications to square masks where $p - q = 0$. These are called Modified Uniformly Redundant Arrays or MURAs. These patterns are constructed as follows.

$$A_{i,j} = \begin{cases} 0 & \text{if } i = 0 \\ 1 & \text{if } j = 0, i \neq 0 \\ 1 & \text{if } C_i C_j = +1 \\ 0 & \text{otherwise} \end{cases} \tag{1.10}$$

where

$$C_i = \begin{cases} +1 & \text{if } i \text{ is a quadratic residue modulo p} \\ -1 & \text{otherwise} \end{cases} \tag{1.11}$$

In equation 1.10 and 1.11 i is a quadratic residue (modulo p) if there exists an x such that $x^2 = q(\text{mod } p)$. A is generally defined as basic pattern or unit pattern, while p is defined as the rank of the basic pattern, where p is in the form $4m + 1$ with $m = 1, 2, 3....$

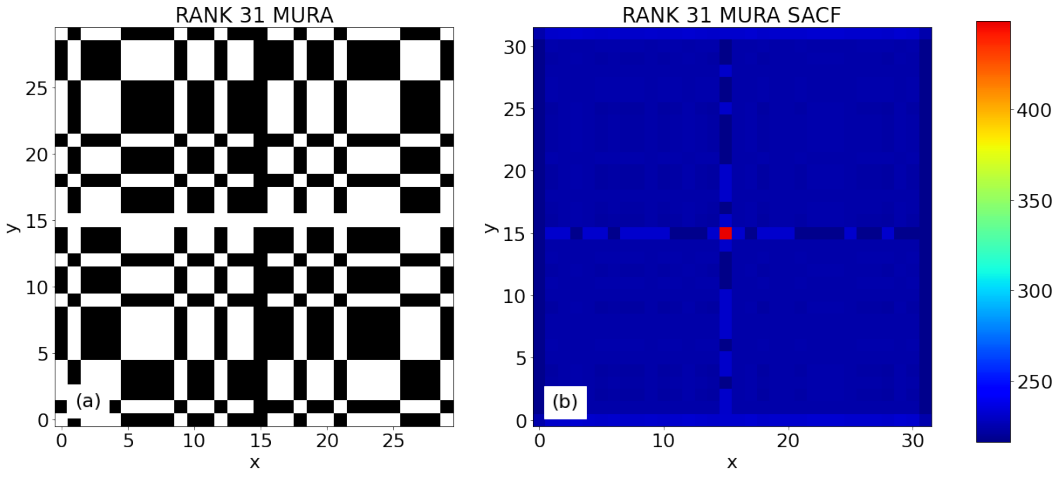

FIGURE 1.11: (a) A rank 31 MURA pattern. (b) SACF of a rank 31 MURA pattern. The maximum correlation occurs at the centre. The sidelobes present a mostly flat background with a characteristic 'cross' pattern centered on the peak

Figure 1.11 shows that the SACF of a MURA pattern presents an intrinsically flat background. This feature is due to the fact that the pattern is uniformly redundant. This background can be easily removed by an appropriate choice of deconvolution array. The construction of the deconvolution arrays for MURA patterns was first presented by Gottesman and Fenimore in 1989 (23), and is very similar to that used for URA patterns, with a modification for the first cell:

$$G_{i,j} = \begin{cases} +1 & \text{if } i = 0 \\ +1 & \text{if } A_{i,j} = 1, i \neq 0 \\ -1 & \text{if } A_{i,j} = 0, i \neq 0 \end{cases} \tag{1.12}$$

The presence of negative values in 1.12 and in general in deconvolution arrays will be further explained in section 1.4 Random patterns and MURAs are the two most commonly used arrays for coded mask imaging and have been for a really long time. The optimal imaging properties of MURAs have been exploited in astronomy by the IBIS telescope on board the INTEGRAL mission and, in their hexagonal form, by the SPI (SPectrometer on INTEGRAL) telescope (24). However, random mask patterns should not be disregarded because they can be produced of any shape and open to close pixel ratio.

1.4 Balancing Cross-Correlation Images

The background level in cross-correlation images is due to non-zero correlation between the mask pattern and the shadowgram in every position of the field of view. This level of background is intrinsic to the cross-correlation process and can be eliminated by appropriate construction of the deconvolution array. As a first approximation the mask pattern itself can be used as a deconvolution array. For example, considering a random mask like the pattern in figure 1.8, the deconvolution array can be expressed as:

$$G_{i,j} = \begin{cases} 0 & \text{if } A_{i,j}=0 \\ 1 & \text{if } A_{i,j}=1 \end{cases} \tag{1.13}$$

Figure 1.12(a) shows a very ideal version of a shadowgram produced by an on-axis source, with one count in the illuminated pixels and no counts in the obscured pixels. Cross-correlation with the array described in 1.13 produces an unbalanced image, similar to the image shown in the centre of figure 1.12. The unbalanced image shows a clear peak in the middle but also a background level with average ~ 209. Due to the randomness of the mask, the image also presents fluctuations around the

average background level, which depend on the specific pattern. Figure 1.12(c) is the cross-correlation between the shadowgram and a balanced deconvolution array, constructed as:

$$G_{i,j} = \begin{cases} -1 & \text{if } A_{i,j}=0 \\ 1 & \text{if } A_{i,j}=1 \end{cases} \tag{1.14}$$

While the random structures in the background are still present, the average value of the image has been brought to zero, increasing contrast and thus SNR.

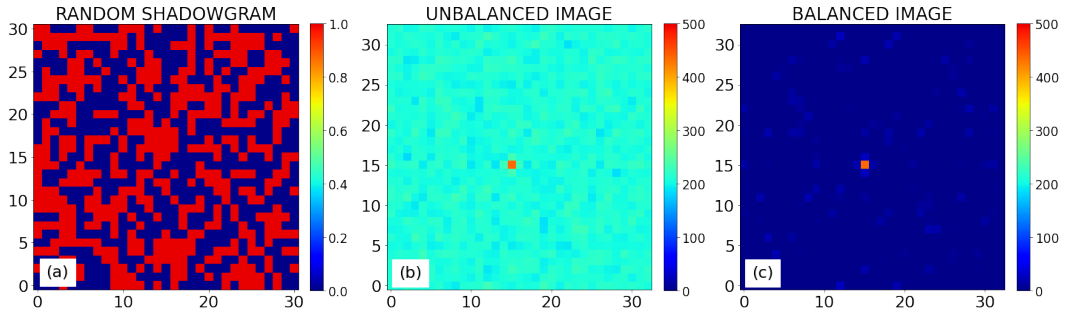

FIGURE 1.12: (a) Ideal shadowgram for an on-axis source and a random mask. (b) Unbalanced cross-correlation. (c) Balanced cross-correlation. While the random features in the background are the same, the balanced image does not have a constant background component

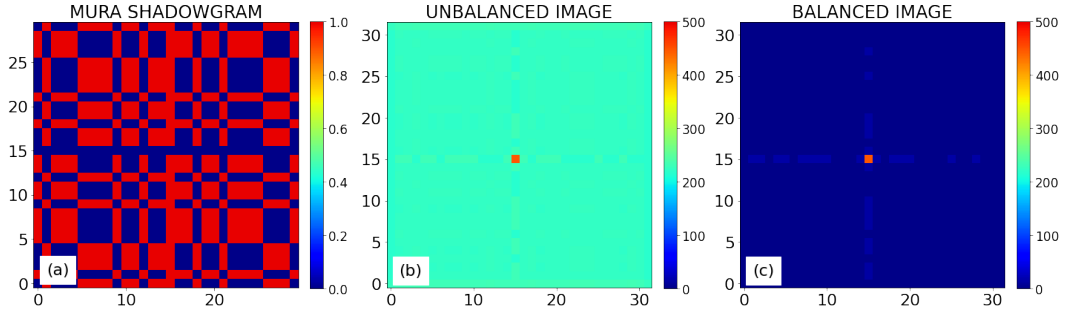

FIGURE 1.13: (a) Ideal shadowgram for an on-axis source and a MURA mask. (b) Unbalanced cross-correlation. (c) Balanced cross-correlation. Since MURA images already present an almost constant sidelobes in the SACF, balancing brings the background level to zero

The possibility to remove the constant level of background in cross-correlation images is particularly useful when operating with MURAs, since the coding background is already flat in the SACF. The optimal decoding array G for MURA patterns is defined in equation 1.12. The contribution of the negative values of the array G bring the constant background level down to zero in the deconvolved image(17). The sidelobes of the correlation $A * G$ and thus the level of the inherent noise are

constant and zero, as shown in the balanced image in figure 1.13. Generally speaking, choosing G to optimize the background characteristics of coded mask images is a technique known as balancing and it will be further elaborated in section 6.1.3.

1.5 Mask-Detector Configurations

The optimal properties of MURAS are only achieved if the whole unit pattern is sampled by the detector plane. In order to maximise the area of the FOV where sources can be fully coded, different camera designs can be adopted.

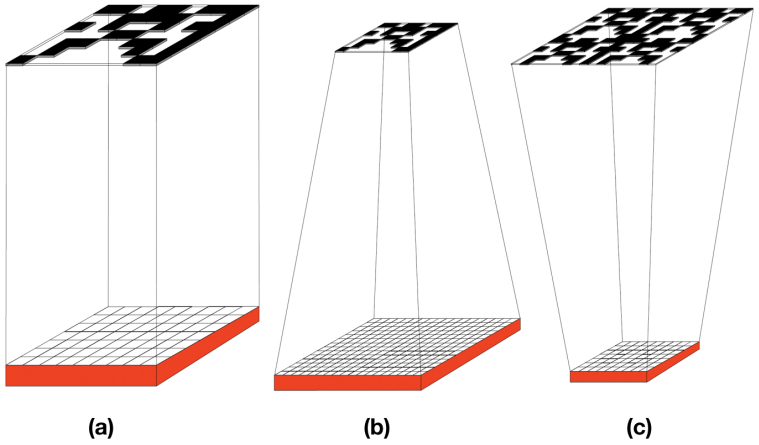

FIGURE 1.14: Possible configurations for coded mask cameras designs. (a)The detector and the coded mask have the same size. (b)The detector is bigger than the coded mask. (c)The mask is bigger than the detector plane and is a 2x2 repeat of a basic MURA pattern

Figure 1.14 shows three possible configurations for a MURA coded aperture camera. On the left, figure 1.14(a) displays a system where the detector and the coded mask have the same size. This system would obtain close to perfect image characteristics for on-axis sources, but any source even slightly off-axis would fall into the PCFOV. Option (b) has a larger FCFOV, but also makes inefficient use of the detector plane: the shadow of the mask is smaller than the detector plane, always leaving a portion of the active detector in the dark. The design in figure 1.14(c) is the most commonly used for MURA based telescopes. The detector is the same size as a single MURA pattern, while the coded mask consists of a 2x2 repetition of the unit MURA pattern. Generally, in order to avoid ambiguities, the mask is a 2x2 repeat of the unit pattern with one row and one column removed. With this configuration sources in a bigger FCFOV than design (a) cast a shadow of a cyclically shifted version of a basic MURA

pattern over the whole detector area. Since a cyclically shifted basic MURA pattern also has a SACF with flat sidelobes, optimal imaging capabilities are obtained in the whole FCFOV. Figure 1.14(c) represents a MURA mask design based on a repeat of four copies of a 17×17 basic pattern and its SACF. It is mostly flat, with the presence of secondary peaks called ghosts. These are due to the cyclic nature of the mask. It is not trivial to eliminate these spurious peaks in the image. The technique used in INTEGRAL data analysis to deal with ghosts will be illustrated in section 2.2.3.

1.6 INTEGRAL/IBIS Space Telescope

The algorithms that have been developed in this research project are general and in principle can be implemented to a variety of coded mask imagers. However, the basis for this work focuses on the analysis of low-level data from one of the instruments on board the INTEGRAL satellite: the IBIS telescope (Imager on Board the INTEGRAL Satellite).

IBIS is a coded mask hard X-ray/soft γ-ray telescope, launched onboard the ESA space mission INTEGRAL in October 2002. A depiction of the INTEGRAL telescope is represented in figure 1.15, where it is possible to identify the MURA square coded mask that is mounted on IBIS. IBIS achieves a wide spectral coverage ranging from approximately 20 keV to 20 MeV thanks to the two detector planes it is equipped with, which are layered below the tungsten-based coded mask.

FIGURE 1.15: A drawing of INTEGRAL Space Telescope. The IBIS square coded mask and the SPI round mask are visible in the front part of the image.

1.6.1 The Coded Mask

The IBIS coded mask is made of a 16mm thick layer of a 90%W-5%Cu alloy, that lays 3200mm above the detectors module. The high density of the alloy ensures a minimum opacity of 70% for 2 MeV photons.

(A) A picture of IBIS coded mask in its supporting frame (25).

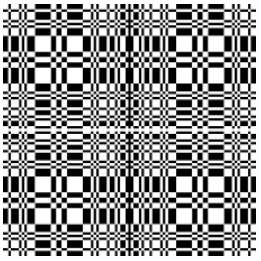

(B) The IBIS coded mask pattern. (white: transparent elements, black: opaque elements (25))

The mask pattern, shown in figure 1.16b, is made of 95×95 square cells, forming a repeat of a 53×53 MURA basic pattern minus a column and a row. The solid elements of the mask are connected together by 2mm ribs, making the mask self-supporting. Nonetheless the mask is mounted on with a support panel, which provides the necessary stiffness and strength to withstand the launch and in-orbit conditions. The mask provides a FCFOV of $\sim 9°$ and a PCFOV of $\sim 30°$.

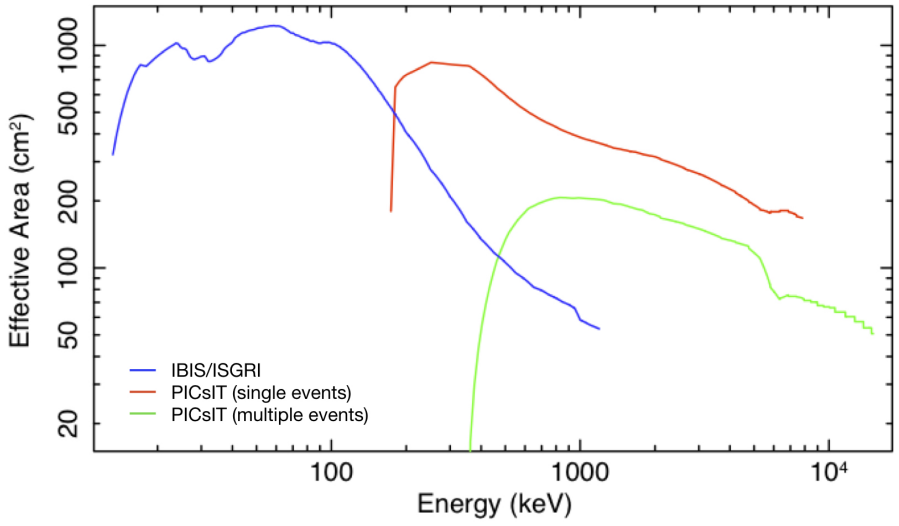

FIGURE 1.17: Effective area of IBIS/ISGRI, PICsIT single events and PICsIT multiple events (25)

1.6.2 The IBIS Detectors: ISGRI and PICsIT

IBIS is equipped with two detector modules, with different sensitivity in different energy ranges. ISGRI, the INTEGRAL Soft Gamma Ray Imager is the low energy camera. The active detector layer of the camera is made of 8 independent modules of 64 $\times$ 32 CdTe crystals. Each crystal is a 4mm$\times$4mm, 2mm thick detector, read out by a dedicated integrated electronic channel. Gamma-ray photons penetrate the CdTe and ionizes the material, generating an electric signal. The electric signal recorded, after proper calibration and corrections, gives information on the energy of the photon and position of the interaction. The high energy detector PICsIT (Pixellated Imaging Caesium Iodide Telescope) is composed of 64 $\times$ 64 CsI bars of 8.4mm $\times$ 8.4mm $\times$ 30mm, each coupled to a silicon PIN photodiode. Each detected gamma ray generates a scintillation flash in the CsI, which is then detected by the photodiode and converted in a current signal. The efficiency of IBIS/ISGRI in different energy bands, measured by its effective area, is shown as a function of photon energy in figure 1.17. ISGRI thin CdTe Crystals achieve a good energy resolution, but become transparent to high energy photons, with 50% efficiency reached at 150 keV. Conversely, the CsI crystals that compose PICsIT are more sensitive to higher energy photons but present a lower energy resolution. In particular ISGRI is optimised for energy between 18 keV and 1 MeV keV and PICsIT for energy between 175 keV and 10 MeV. The angular resolution for both instruments is 12', with the point source location accuracy (PSLA) depending on the detector. For SNR=10, ISGRI has a 3' PSLA and PICsIT has a PSLA between 5' and 10'. It is also worth mentioning that if an event triggers both ISGRI and PICsIT detectors can be reconstructed using Compton kinematics (Compton mode).

1.6.3 IBIS Shielding

A passive collimating system made of tungsten and lead structures protects the detector plane from the cosmic gamma-ray background up to a few hundred keV. An anticoincidence veto system shields the detector from gamma-rays coming from the bottom of the telescope. It is composed of 16 independent modules, each one made out with two BGO crystals, read out by two 3 inches photomultipliers.

1.7 Thesis Outline

The overarching goal of this research project is the development of a method to analyse coded aperture data collected when the imaging system is not static. This occurs when the camera is moving between observations of different targets or the target of

the observation is moving. This scenario can happen in different fields, but two in particular were investigated: high-energy aastrophysics and nuclear medical imaging. Starting with the astrophysics application of the research, chapter 2 describes the analysis software currently used to analyse INTEGRAL/IBIS data. This software, which is based on cross-correlation, does not work if the observation is not static. An alternative to cross-correlation is back-projection which is applicable to both static and non-static observations. This method is based on the fact that each photon detected must have come from a source in the sky through an open mask pixel. Each detected photon is traced back to all the directions in the sky that it could have come from through all the open mask pixels. A description of the back-projection approach and its implementation to IBIS data can be found in chapter 3. Following, the results obtained for a reduced trial data set are presented in chapter 4, along with the potential applications of the method.

The success that coded mask imaging has had in high energy astrophysics, together with the intrinsic 3D capabilities of this technique, suggest that it could be suitable for applications in the near-field imaging. One particular application was explored in this research, which is a medical imaging technique known as Single Photon Emission Computed Tomography (SPECT). SPECT uses gamma rays to produce images of a patient's organs. SPECT is currently being performed using collimators, which produce an image by selecting a fraction of the gamma-rays emitted by the source under investigation and absorbing the rest. While photons are emitted isotropically, only the photons traveling in very specific directions are selected by the collimators and are detected to produce an image. The working principles of collimators and their main applications in SPECT are described in chapter 5. Coded masks work in a similar way to collimators, in the sense that they select only a part of the incoming radiation to be captured by the detector and block the rest. Compared to standard collimators used for SPECT however, which only select less than 1% of the incoming photons, coded masks have a transparency of around 50%. The application of coded masks to SPECT could enable a more efficient use of radiation for medical imaging. The radiation dose administered to the patient could potentially be reduced, resulting in different benefits for the healthcare system. The duration of each SPECT scan, which is normally around 30 minutes, could be decreased. Shorter SPECT scans would enable the healthcare system to provide more scans per day, but would also be safer and more comfortable for the patient, which has to stay still for the entire duration of exam. A lower radiation dose, associated with a lower risk, could be used for more frequent monitoring or for paediatric patients, who are more susceptible to radiation damage. More sensitive cameras also could open the way for the development of lower emission new radiopharmaceutical. -Finally, in coded mask systems the size of the field of view is not directly limited by the detector size, and a large FOV can be obtained with a relatively small detector area. With all these

potential benefits in mind, a version of the back-projection algorithm that produces near-field 3D images from a coded mask system was developed in this research and is presented in chapter 6. This algorithm, in fact, implements a photon-by-photon approach, which is applicable to many situations where the target or the camera is moving, such as dynamic studies or for surgical probes. The algorithm was applied to experimental data obtained with a prototype imaging system which is described in chapter 7. Images of samples of various nature recorded in a series of experiments with the prototype camera are presented. Finally, chapter 8 summarises the key findings of the project and the contribution made by this work to the state of the art in gamma ray imaging techniques. Suggestions for further developments and applications in both subject areas are also included in this chapter.

Chapter 2

Analysis of IBIS/ISGRI Pointing Data

This chapter describes the image computation techniques that are currently used to process INTEGRAL pointing data. These techniques are implemented in the 'Off-line Scientific Analysis' (OSA) software that performs all necessary corrections and calibrations, forms a shadowgram and creates a sky map from the raw data transmitted by the telescope(26). The method used in OSA is mostly based on cross-correlation and is thus only applicable to stable pointing data. Before describing in depth a more general approach, which was developed and implemented in this research project, it is worthwhile providing a review of how INTEGRAL performs observations, how data are organised and the procedure for the standard analysis of INTEGRAL data.

2.1 Observing with INTEGRAL

Since the four instruments on-board INTEGRAL are operated simultaneously, every observation includes data from all of the instruments. Typical observations can last from one day to a few weeks and during each observation the telescope can operate in different modes.

2.1.1 INTEGRAL Observing Strategies

Three types of observing strategies are used according to the purpose of the observation:

- In order to suppress systematic noise on the SPI detector plane, the telescope (with the four instruments on board) usually observes in a dithering pattern. Several pointings are made in a raster scan of the region around the target (27). The shape of different dithering patterns is shown in figure 2.1.
- Scanning mode is used to cover large areas of the sky for monitoring purposes. This has mainly been used for galactic plane observations
- Staring observations are mainly used for calibration purposes

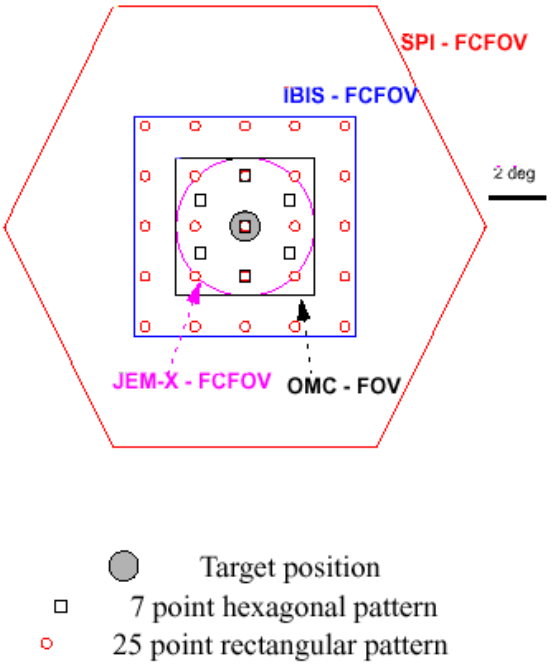

FIGURE 2.1: Shape of different dithering patterns mapped onto the FOV of the different instruments on board of the satellite. The rectangular 5x5 pattern with a 2° step is the default mode and is used for imaging multiple point sources in the field of view, for sources with unknown locations, and for extended diffuse emissions(28). An hexagonal dithering pattern can also be used, but it compromises the imaging capabilities of IBIS and SPI and therefore is only used if the scientific goal require continuous monitoring of the main target by JEM-X

Almost all INTEGRAL pointing observations for scientific purposes are made in dithering mode with a rectangular pattern, which offers the best imaging performance.

2.1.2 INTEGRAL Operation Modes

Independently of the observing strategy used, all data acquisition periods of INTEGRAL fall into one of two operation modes:

- The **pointings** are periods during which the telescope axis remains stable while observing a target. A shadowgram is accumulated in the field of view and an image can be deconvolved using methods based on standard cross-correlation. More specifically, ISGRI data is normally collected in photon-by-photon mode and then histogrammed on ground. PICsIT data is transmitted as a histogram to the ground due to telemetry restraints

- When the telescope is maneuvered from one pointing to the following one, the telescope is operated in **slew** mode. During slews, the pointing axis of the telescope changes continuously. Slew mode science windows are present in ISGRI data archive, but there is no standard software available to obtain sky images from them

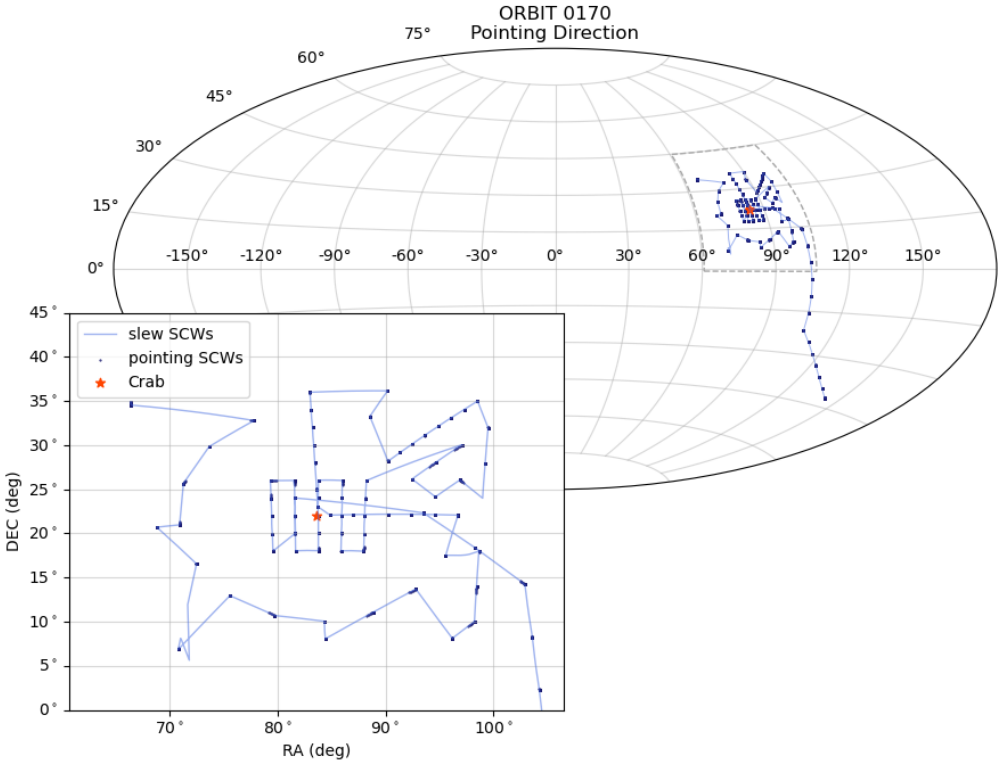

FIGURE 2.2: Orientation of IBIS pointing direction during orbit 170. This orbit includes a series of calibration pointings around the Crab, performed in a square dithering pattern and a wider arc intended to explore the off-axis response. The orbit ends with a long slew

In particular, the data acquisition time is divided into time periods named science windows (usually abbreviated to scw) characterised by one of the two telescope operation mode. The data collected during observations of a single target is usually

composed of a series of pointing and slew science windows performed in a dithering pattern. Slew science windows are also performed between observations, to move the telescope from one target to the next. An example of the motion of the telescope axis during an observation is shown in the plot in figure 2.2, which represents the pointing direction of the telescope during orbit 0170. This orbit included a calibration observation of the Crab, performed in a 5x5 dithering pattern, followed by a series of pointings around the Crab region.

2.2 INTEGRAL 'Off-line Scientific Analysis' Software

The OSA software is a set of tools distributed by the INTEGRAL Science Data Centre (ISDC) that process pointing data collected from all the instruments of the telescope. The software is composed of a series of scripts that reduce the raw data and extract scientific products such as images, light curves and spectra. 'IBIS Science Analysis' is the section of OSA that performs the analysis of IBIS data. Since the back-projection software presented in chapter 3 makes use of some of the results from intermediate steps of OSA's pipeline, this section includes a description of the key stages of OSA and the end products of the imaging stage of the software.

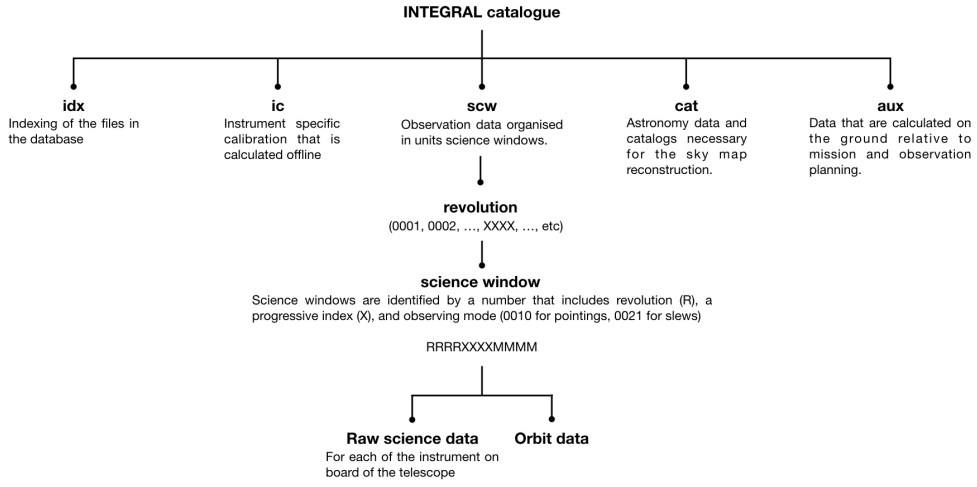

FIGURE 2.3: Organisation of all the data used for IBIS analysis data into an INTEGRAL database. These data include not only science data resulting from interaction in the detectors, but also housekeeping data regarding the status of the instrument and auxiliary data produced during mission and observation planning (28)

2.2.1 IBIS/ISGRI Raw Data Repositories

INTEGRAL database adopts FITS (Flexible Image Transport Standard), which uses image and table files to store astronomical data(29). The INTEGRAL data that are pre-processed and available to the community are stored in FITS tables and images and organised in a number of repositories, represented in the diagram in figure 2.3. Telescope data are divided into five types, according to their origin and their purpose.

- The **auxiliary data (aux data)** derive from mission planning rather than telescope telemetry and are necessary for the analysis of INTEGRAL data
- The **catalogue data (cat data)** repository includes reference observational catalogues used to match detections in the images with known sources
- The **instrument characteristics data (ic data)** are related to the instrument specific calibration and parameters
- The **science window data (scw data)** repository includes pre-processed data transmitted by INTEGRAL instruments. This repository includes the scientific data from the telescope, in the form of an event list and histograms, and data regarding the operation of the telescope
- **Index file data (idx data)** are files which store the indexing system used through the whole repository system

2.2.2 IBIS/ISGRI Data Reduction

The reduction of IBIS/ISGRI data takes the raw list of photon detections as an input and produces calibrated and corrected shadowgrams ready to be deconvolved. These shadowgrams are energy calibrated and take into account the instrument efficiency and characteristics. PICsIT data, on the contrary, is normally histogrammed on board and transmitted as a histogram.

Correction

The first step of IBIS data analysis is the construction of corrected data structures. Pixels that had a switch off during the observation and pixels with an abnormal time distribution of events are considered noisy and events occurred in those pixels are ignored in the subsequent analysis. At this stage an energy value in keV is also assigned to each event.

Good Time Intervals

Good Time Intervals (GTIs) are the time intervals in which events are considered valid and usable for the analysis. OSA computes tables of GTIs using the instrument data containing information about the satellite stability, instrument status and gaps in the data.

Dead Time

The dead time of a detector system is the time interval after a detection in which a second event can't be recorded. ISGRI dead time for each detector module is calculated as the combined effect of the detector dead time, and the additional dead time introduce by the veto shielding, calibration and Compton counts (if Compton mode is on). The observed count rate C_o depends on the real count rate C and the dead time D according to:

$$C_o = C(1 - D) \tag{2.1}$$

The effects of different sources of dead time were evaluated in flight during the commissioning stage of the mission. Considering that the trigger rate per ISGRI module is around 800 s^{-1} and that the ISGRI processing time for each event is 114 μs, the dead time associated to event processing is around 9% However, the coincidence windows applied with the veto system, the calibration source and PICsIT increase the effective dead time to about 24% on average (30).

Binning

Event data are split into time and energy bins according to whether the goal is imaging, light curve or spectra production. A shadowgram is produced for each time and energy bin selected by the user. Efficiency shadowgrams are also produced, taking into account the dead time D and the energy dependent detector efficiency. These two factors are combined as:

$$Eff(T, E, y, z) = (1 - D(T, module))LT(E, y, z) \tag{2.2}$$

where T is the time, y and z are the coordinates of the detector pixels in the detector plane yz. The energy dependent term LT is derives from the low threshold operation limit of the telescope. This limit represents the degradation of the detector at lower energies as a result of the passage of charged particles such as cosmic-ray protons. To account for it, all events below a characteristic low threshold value (which depends on the orbit number) are removed. At this stage one further correction is applied:

the eight detector modules comprising ISGRI are separated by a gap of the width of two pixels. These gaps are filled with the average number of detector counts, to reduce the formation of artifacts in the final image. The value of the low energy threshold was set to 17 keV at the beginning of the mission and has been increased since then up to 30 keV(31).

2.2.3 IBIS/ISGRI Image Reconstruction

Cross-Correlation

Sky images are deconvolved using a discrete cross-correlation of the binned and corrected shadowgrams.

$$S_{i,j} = \sum_{k,l} G_{i+k,j+l} D_{k,l} \tag{2.3}$$

Assuming Poisson statistics, the variance of each sky pixel is constant in the FCFOV and equal to

$$V_{i,j} = \sum_{k,l} G^2_{i+k,j+l} D_{k,l} = \sum_{k,l} D_{k,l} \tag{2.4}$$

and equal to the sum of detector counts. This deconvolution is extended to the PCFOV, by applying a non cyclic cross-correlation with an expanded version of the deconvolution array G padded with 0 elements. This extension obtains a larger FOV, but requires a proper normalisation in order to obtain a flat background. In order to properly balance the cross-correlation image in the PCFOV and obtain a flat background in absence of sources, the negative part of the deconvolution array is multiplied by a factor before being subtracted. The normalisation or balancing factor is

$$B_{i,j} = \sum_{i,j} \frac{n^+_{i,j}}{n^-_{i,j}}, \tag{2.5}$$

where n^+ is the number of detector pixels that can see the position of the sky pixel i, j through an opening in the mask, while n^- the number of detector pixel that do not have the sky pixel i, j on a line of sight because the closed elements of the mask are blocking its view. The interpretation of this factor will be discussed further in chapter 6, where a similar balancing will be applied to near-field images. Taking into account the proper balancing and the efficiency of each pixel, the corrected sky

maps are obtained with

$$S_{i,j} = \sum_{k,l} G^{+}_{i+k,j+l} W_{k,l} D_{k,l} - B_{i,j} \sum_{k,l} G^{-}_{i+k,j+l} W_{k,l} D_{k,l} \tag{2.6}$$

In equation 2.6 B is the balancing array and W is a weighting factor that takes into account losses in detection efficiency in pixels or areas of the detector. G^{+} and G^{-} are defined as:

$$G^{+} = \begin{cases} G & if G > 0 \\ 0 & if G < 0 \end{cases} \tag{2.7}$$

$$G^{-} = \begin{cases} -G & if G < 0 \\ 0 & if G > 0 \end{cases} \tag{2.8}$$

The G arrays are also expanded and padded with zeros for a non-cyclic cross-correlation. Variance maps , which are not constant outside the FCFOV, are calculated accordingly:

$$V_{i,j} = \sum_{k,l} (G^{+}_{i+k,j+l} W_{k,l})^2 D_{k,l} + B^2_{i,j} \sum_{k,l} (G^{-}_{i+k,j+l} W_{k,l})^2 D_{k,l} \tag{2.9}$$

Ghost images

In order to optimise the use of the active detector area, IBIS coded mask uses a configuration with a 2x2 repeat of a basic MURA pattern. In section 1.5 it is specified that the removal of one row and one column from the pattern would avoid ambiguities. This is only true to a certain extent. Figure 2.4 represents a deconvolved image of an on-axis source, captured with a 2x2 repeat of a rank 53 MURA (the mask system used by INTEGRAL). The source peak, indicated with an arrow, is visible at the centre of the image. However, lower 'ghost' peaks in the PCFOV are also visible at symmetrical positions around the source peak. Ghosts are due to the repeated nature of the pattern. Especially if multiple sources are present in the FOV, the presence of ghosts would seriously compromise the quality of the image, and therefore they need to be identified and removed. The removal of one row and one column from the pattern will cause ghosts to have a lower value than the main peak, making them recognisable and removable.

Cleaning and Computation of Sky Maps

The sky map is computed from the cross-correlation image by means of an iterative algorithm that searches for significant peaks. This process is enhanced by the use of a reference source catalog of likely positions. To do so, OSA has a 'ghostbuster'

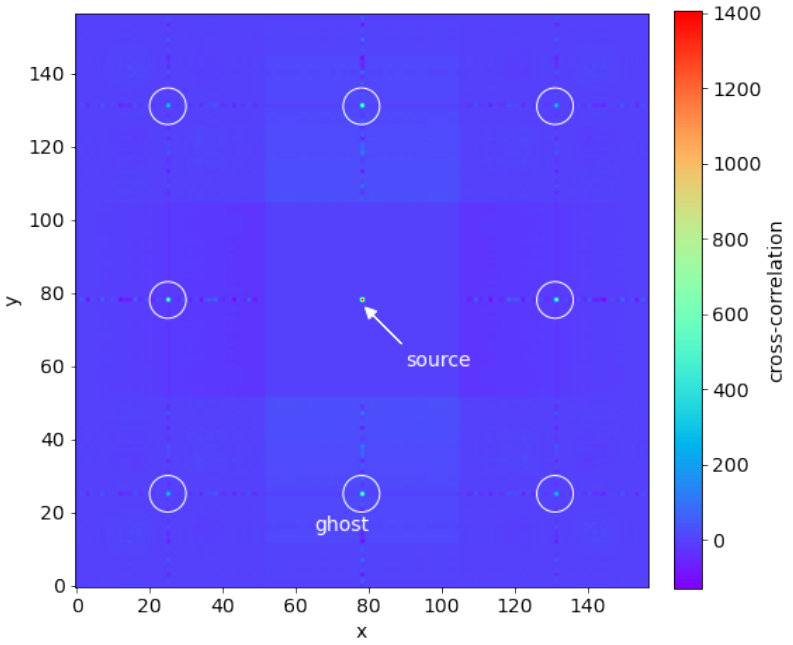

FIGURE 2.4: Image obtained by deconvolution from a 2x2 repeat of a rank 53 MURA basic pattern. The resulting image shows a source peak in the centre, accompanied by 'ghost' peaks, indicated with white cirles, in the PCFOV

tool that cleans the image and produces the final sky map. This tool identifies the contribution of every bright source in the raw image, including the ghosts, operating as follows:

- The brightest source in the FOV is found in the reference catalogue and the corresponding peak is found in the map
- The peak corresponding to the brightest source in the catalogue isx fitted it with an analytical approximation of the PSF
- A Shadowgram for a source that corresponds to the fitted PSF is modeled. This shadowgram represents the contribution of the brightest source to the measured shadowgram.
- The contribution of the brightest source is subtracted from the shadowgram. At the same time, the model of the brightest peak is added to a 'cleaned' image.
- A second image is deconvolved from the shadowgram after the source contribution has been removed. This will generate an image without the brighest peak and its associated ghosts.

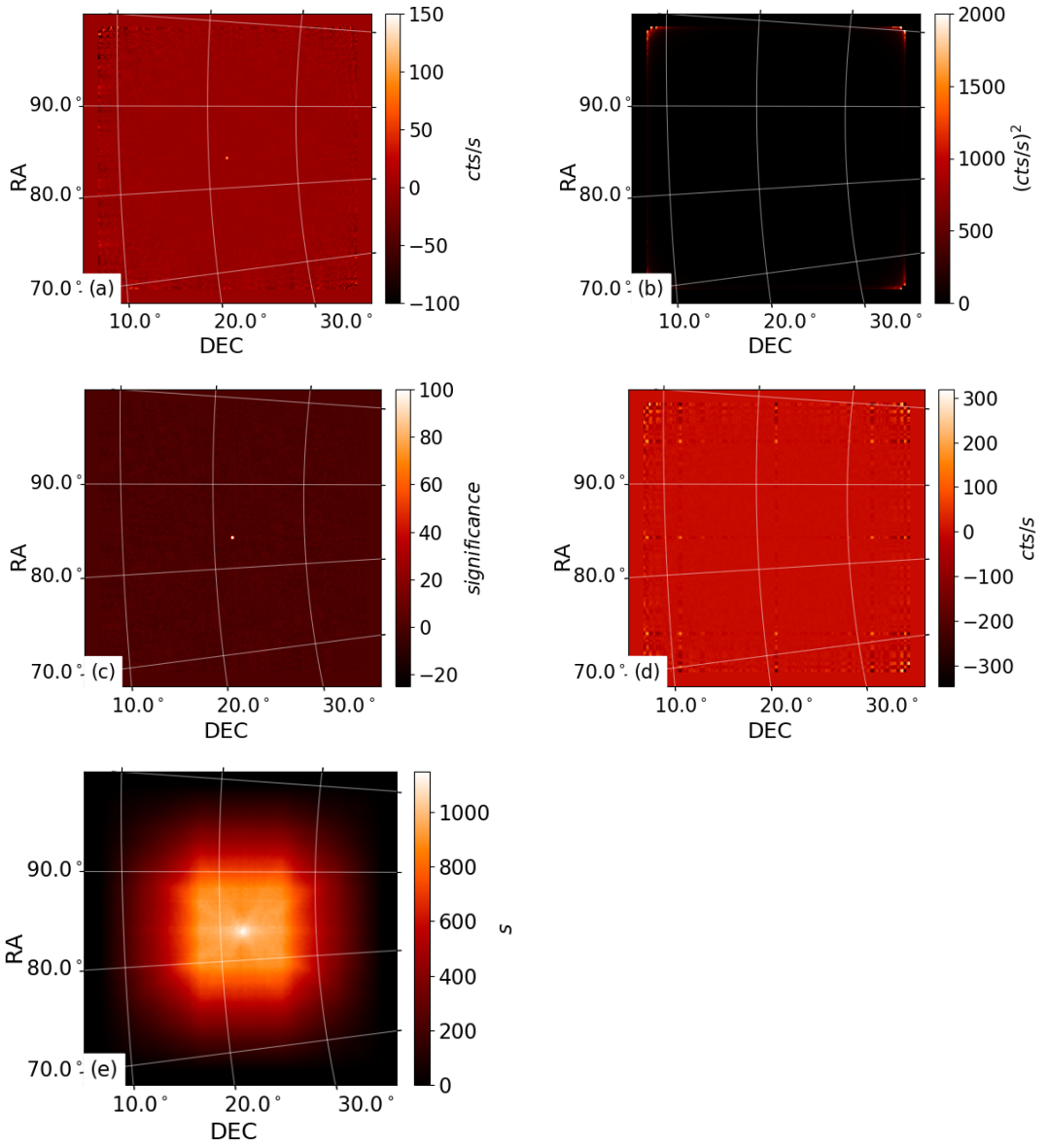

FIGURE 2.5: Sky map produced by OSA with data from the pointing science window 146100410030. This is another calibration observation of the Crab, which is a really good example of images of a sigle bright source at the centre of the FOV. (a) Intensity map after ghost correction, (b) Variance map, (c) Significance map, (d) Map of residuals, (e) Effective exposure

The process is repeated until all sources or excesses are identified. The final sky image is composed of the primary peak of each source. When modeling the shadowgrams for each source contributions, the number of counts per second for each contribution is estimated. The units of the final sky maps are reconstructed counts per second in the FCFOV. Exposure maps are also computed at this stage. These maps represent the effective exposure time in each pixel in the FOV and are used to normalise the sky maps to count rate.

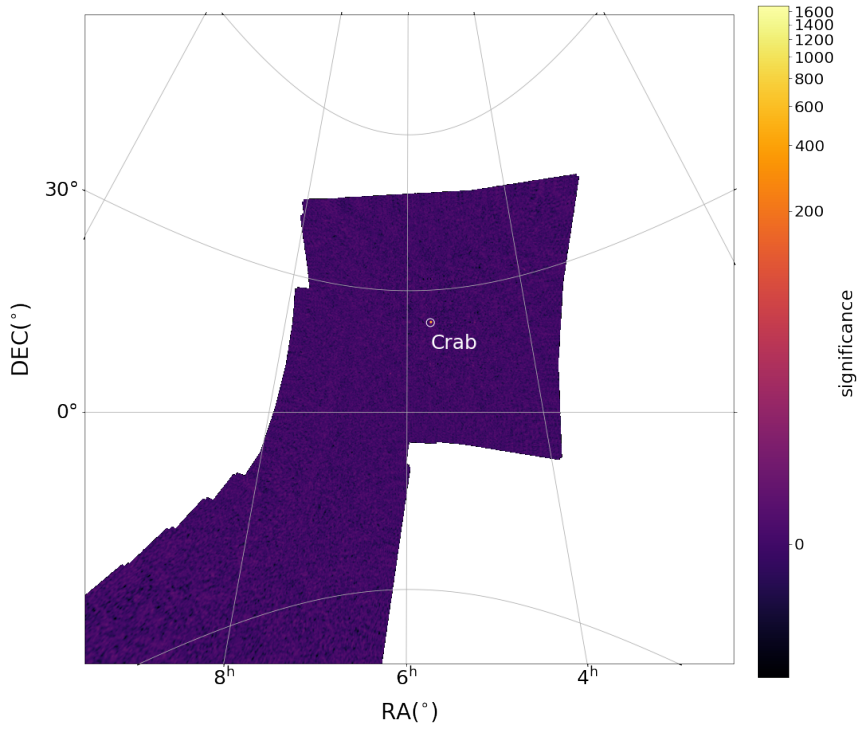

FIGURE 2.6: Mosaic map of the Crab with pointing data from orbit 170. The overlap of several science windows as the telescope is approaching the target is visible in the bottom left corner of the map

2.2.4 Outputs of the Image Reconstruction

Depending on the parameters entered by the user, the OSA analysis of pointing observations returns a series of images, or maps, which are stored as multiple subsections (called extensions) of a *.fits* file. The standard output structures include intensity and variance maps, from which significance maps are produced, as well as exposure and residual maps. Since version 10 of OSA, exposure maps represent the 'true exposure' of the observation, which also includes self-collimation effects of the mask supporting structure. The residual maps include the residuals of the source peak subtraction from the intensity images operated during the cleaning stage and can be used for diagnostic purposes. The software also produces lists of sources found in the individual science windows. The standard output of the image reconstruction stage is shown in figure 2.5. These images are first produced at a science window level and then (if requested) rotated and projected over a reference image to produce maps of observations composed of multiple science windows(26). As an example, figure 2.6 shows the mosaic image obtained with the data from the pointing science windows forming the square observing pattern drawn in figure 2.2. With the mosaic, a list of sources found in the single science window maps and in the final map are also provided.

Chapter 3

Imaging with IBIS/ISGRI Slew Data

3.1 Motivation

As described in section 2.1.2, ISGRI observing time is spent into one of two operational modes: pointing mode or slew mode. Table 3.1 shows how the total amount of ISGRI observation time was divided between different operating modes from the time of launch in October 2001 to October 2022. Pointing observations constitute 88% of IBIS data and sum up to more than 500 Ms of observation. Slew observations constitute 11% of the total observing time. Finally, less than 1% of the exposure time is dedicated to engineering observation which do not have scientific purposes and are classified as neither a pointing nor a slew. The total time spent observing in slew mode by INTEGRAL is 65Ms ($\sim$2 years, which was originally INTEGRAL's nominal operational life). In spite of the considerable amount of slew data, a software to reduce this type of data has never been developed nor released. At the time of launch, in fact, the INTEGRAL mission was originally planned to last for only a few years. Processing of slew data is not trivial and computationally challenging and only justified, at this point, by the large amount of data that was gathered during the over 20 years of operation. Table 3.1 also shows the approximate duration of each science window. It is important to keep in mind that the duration of each science window can vary considerably depending on the target and the observation schedule from 200s up to over 1000s in some cases.

Due to the mode of collection, processing these data is particularly challenging on a computational level, and an analysis tool is not yet available for them. The goal of this work is the development of an analysis tool for IBIS/ISGRI slew observations

scw type	Total Exposure (Ms)	Number of scw	Approximate scw duration (s)
OTHER	5	7627	600
SLEW	65	192724	300
POINTING	507	195894	2500

TABLE 3.1: Total IBIS exposure for orbits 1 to 2500. The majority of time is dedicated to pointing observations for scientific or calibration purposes. Slew observations, carried out between pointings constitute a non negligible fraction of a total exposure time. the rest of the science windows, classified as 'OTHER', are performed for engineering purposes

and the production of a survey of these data. The contribution of this additional observation set to the INTEGRAL dataset will be:

- Long term monitoring of transient activity of known sources. Slew observations can provide additional data points for INTEGRAL light-curves with a non regular time spacing. This will help timing analysis, for example evaluation of orbital periods and duty cycles of X-ray binaries.
- Search for new X-ray transient sources in areas of the sky that aren't normally observed in pointing observations.

3.2 Introduction to Back-Projection Analysis

Figure 3.1 shows the shadowgram recorded by ISGRI in a single pointing science window during orbit 0170. This scw is part of a calibration observation of the Crab pulsar and is a good example of a shadowgram of a single bright source in the sky. The shadow of the coded mask pattern is clearly visible on the detector plane, and a simple deconvolution will show an obvious primary peak in the position of the Crab.

Generally speaking, during slew observations, the mask pattern is not obviously noticeable in the detector image. In fact the detector image is the shadow of a mask that is constantly moving relatively to the sources, and therefore a cross-correlation with the correlation inverse array G does not present peaks at the source positions. What makes reconstruction of slew images possible is the fact that each detected photon must have passed through one of the apertures in the mask. The knowledge of the instrument geometry can in principle be used to trace back each detection (event) to all the regions of the sky that the corresponding photon could have come from. The position of astronomical sources is then reconstructed by tracing a great number of photons from different positions in the detector. This process of image

reconstruction is called back-projection. Back-projection presents some similarities with the method developed by Fenimore called URA tagging which can be used when time resolution is needed,operates in the image plane and does not require deconvolution (32).

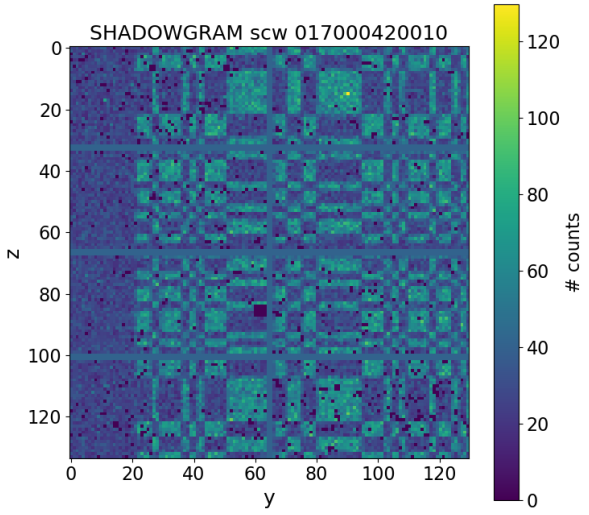

FIGURE 3.1: Shadowgram of a single IBIS/ISGRI science window from orbit 0170. The target of the observation (the Crab) is in the PCFOV and is so bright that the shadow of the mask pattern is recognisable in the detector image. A few dead pixels and bright (noisy) pixels can be identified

3.2.1 Single Pixel Projections

In principle, knowing the position of the detection and ISGRI pointing direction at the time of each photon detection, it is possible to trace each photon back to its origin in the sky through all the open mask pixels. In practice this is a really computationally intense task. To make the computation more manageable, the back-projection algorithm makes use of pre-calculated single pixel projections (SPPs). Each single pixel projection represents the portion of the ISGRI field of view that can be observed by a specific detector pixel through all the openings in the mask. Examples of a single pixel projection for IBIS/ISGRI are shown in figures 3.2 (a) and (b). The two plots represent the PCFOV of IBIS telescope, which is $\sim 30^\circ \times 30^\circ$ with the exposed detector area dropping from 100% to 0 at the borders of the PCFOV. The area of the PCFOV was divided into $4.5' \times 4.5'$ pixels, to match the resolution of pointing OSA images. Figure 3.2(a) shows the SPP for a pixel at the centre of the detector plane, Figure 3.2(b) shows the SPP for a pixel at one corner of the detector plane.

The interpretation of these projections is that a source placed anywhere in a sky pixel with value 1 fully illuminates the detector pixel under consideration through one of the mask openings. On the contrary, a source placed anywhere in a pixel with value between 0 and 1 only partially illuminates the detector pixel. Further details on the construction of the SPPs and the meaning of negative values in them are provided in section 3.2.1. The addition of a great number of SPPs corresponding to the detector pixels where gamma-rays were detected will produce a back-projection image. Addition of the SPPs is performed after appropriate rotation to account for the pointing direction of the telescope. Back-projection can be compared to other photon tracing techniques such as the use of Compton scatter or pair production. These techniques, used in telescopes like CGRO (The Compton Gamma Ray Observatory)(33) or Fermi-LAT use parameters calculated from different types of interaction in a detector to trace a great number of photons back to their regions of origin. By accumulating a great number of photons, the position of the gamma-ray sources is constrained.

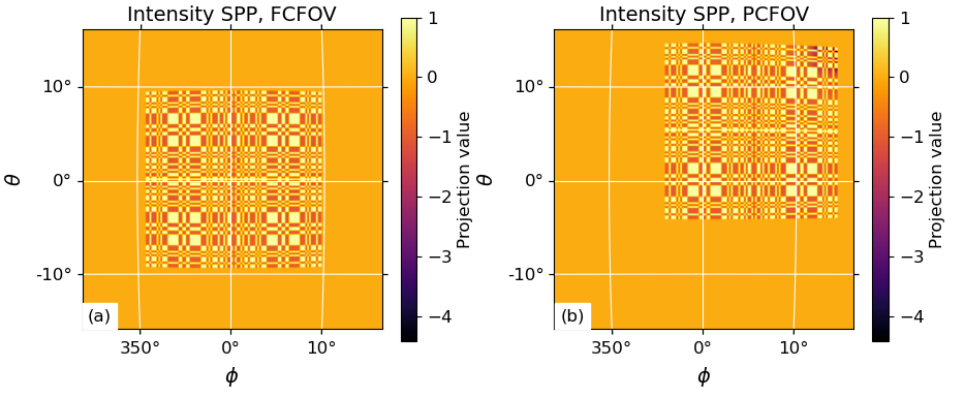

FIGURE 3.2: Single Pixel Projections. (a) and (b) Represent the visibility of ISGRI FOV from the position of a pixel in two different positions of the detector. If a photon is detected by a a certain detector pixel, it must have been emitted in the regions of the FOV with SPP >0

For each detector pixel, the SPP is calculated by assigning a numerical value to each sky pixel in the field of view. This value represents whether the sky pixel can be seen by the detector pixel through one of the openings in the coded mask. In the first instance, for detector pixel l, m and sky pixel i, j the assigned values can be set to:

$$SPP^{l,m}(i,j) = \begin{cases} 1, & \text{if sky pixel i, j is seen by detector pixel l,m} \\ 0, & \text{if sky pixel i, j is not seen by detector pixel l,m} \end{cases} \tag{3.1}$$

In order to obtain $SPP^{l,m}$ it is necessary to add the contribution from each open mask pixel p_m to the visibility of the field of view by the detector pixel l, m

$$SPP^{l,m}(i,j) = \sum_{p_m} SPP^{l,m}_{p_m}(i,j) \tag{3.2}$$

$SPP^{l,m}_{p_m}$ is the part of the FOV visible by detector pixel l, m through the single mask opening p_m. Assigning a value of 0 or 1 to the sky pixels in the SPP corresponds to projecting the area of each detector pixel back to the sky map plane through all the openings in the mask. Although this choice of array is sufficient to obtain a peak in the source position, a few corrections need to be applied to 3.1 in order to obtain good quality images. The refinements applied to $SPP^{l,m}$ are described in the following sections.

Partial Illumination of Detector Pixels

One of the effects that should be taken into account is the capacity of a source in a certain position to illuminate partially or completely a certain detector pixel. This characteristic of each position in the FOV is called pixel illumination fraction (PIF) and depends on the position of the detector pixel and the telescope and mask geometry. In order to simply visualise this effect it is useful to consider a single mask pixel - detector pixel pair. Figures 3.3 a, b, and c are diagrams of a very simple system composed of a detector, a single mask pixel and a source placed in a plane at a certain distance from the mask. The images show, on the right, a detector formed by 4x4 pixels. The single detector pixel under consideration is highlighted with a darker gray. The mask pixel is shown in the centre of the drawings. On the right, the source is represented with a sun symbol. The portion of the plane containing the source that is visible to the detector pixel is divided into different regions, shaded in different colors, which meaning is hereby explained:

At the top, figure 3.3a shows that a source positioned in the central square area highlighted in blue (region A) will illuminate the full area of the pixel. Region A will then have a PIF value of 1. Similarly, a source positioned towards the edges of the shaded area, in the regions highlighted in green (region B), or in the regions highlighted in orange (region C), will only illuminate a 'slice' or a 'corner' of the detector pixel. The PIF value of regions B and C is less than 1, because a source placed in these regions will only illuminate the detector pixel only partially When calculating the SPP, this partial illumination of the pixels needs to be taken into account. A sky pixel in region C does not have the same visibility of a sky pixel in region A, because it only illuminates part of the detector pixel.

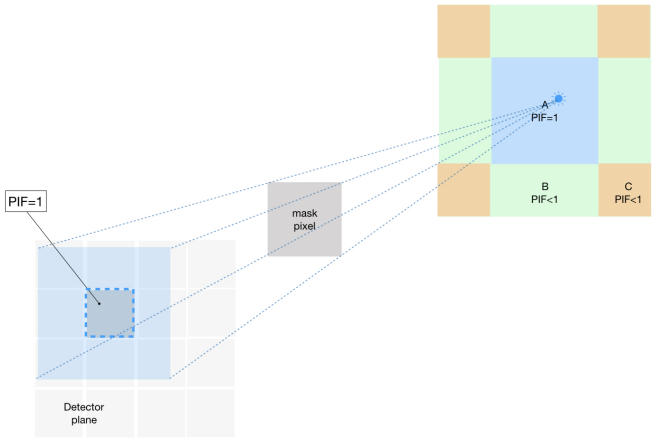

(A) A source in Region A illuminates the entirety of the detector pixel highlighted in the figure. All sources in region A have PIF =1 relative to that specific detector pixel

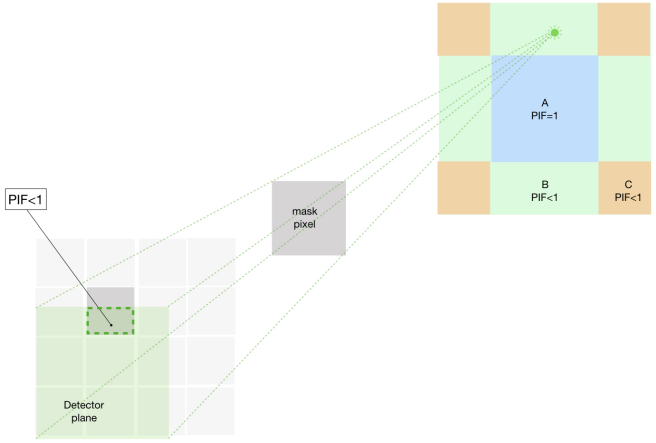

(B) A source in Region B illuminates part of the detector pixel highlighted in the figure. All sources in region B have PIF < 1 relative to that specific detector pixel

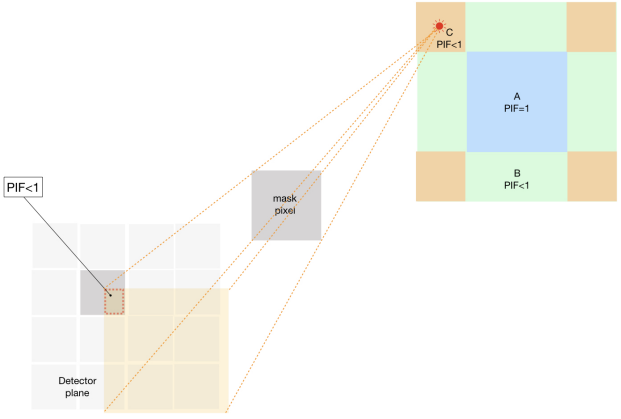

(C) A source in Region C illuminates part of the detector pixel highlighted in the figure. All sources in region C have PIF < 1 relative to that specific detector pixel

FIGURE 3.3: The portion of the FOV visible by a single detector pixel through a single mask pixel. Highlighted in blue, green and orange, the regions of different PIF of the detector pixel highlighted with a darker gray in though the mask pixel represented in each figure

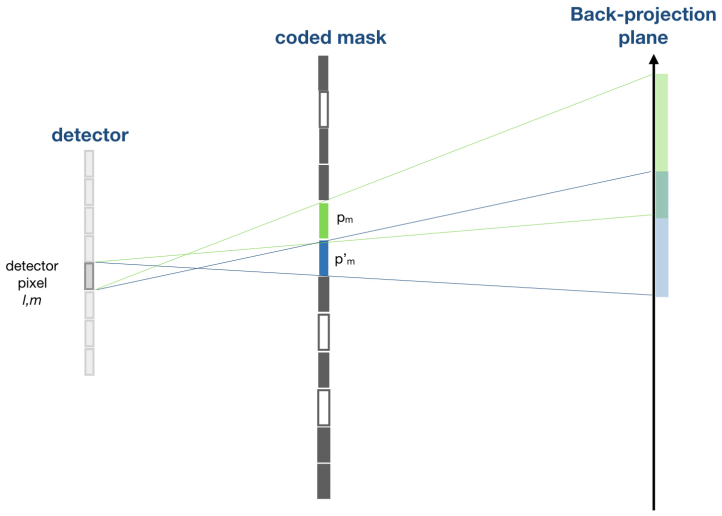

FIGURE 3.4: Cross section of the FOV of a coded mask camera. The regions of the FOV visible by a detector pixel through two adjacent mask pixels p_m and p'_m, highlighted respectively in green and blue, partially overlap

Detector Pixel Illumination through Adjacent Mask Pixels

Figure 3.4 shows the cross-section of the field of view of a generic coded mask imager. Detector pixel l, m is taken into consideration. The portion of the FOV that is visible by detector pixel l, m through p_m (highlighted in green) overlaps with the part of the FOV visible by detector pixel l, m through the adjacent mask pixel p'_m (highlighted in blue). As a consequence, if $SPP^{l,m}$ was constructed by simply assigning 1 to the regions of the FOV that are visible by detector pixel l, m through each mask pixel and then summing the contributions from all the mask pixels, equation 3.2 would account more than once for the overlapping regions.

Figures 3.5a and 3.5b show the diagram of the same system as figure 3.3, but considering the mask pixels adjacent to the first. The illuminated portion of the detector through each of the two mask pixels is shaded in green in figure 3.5a and orange in figure 3.5b. When a detector pixel is only partially illuminated through an open mask pixel, depending on the source position, the remaining portion of the detector can be illuminated through one or more of the adjacent mask pixels if they are open. In order to correctly account for detector pixels that are illuminated through more than one mask pixel, the positive values of $SPP^{l,m}_{p_m}$ were obtained by the following approximation:

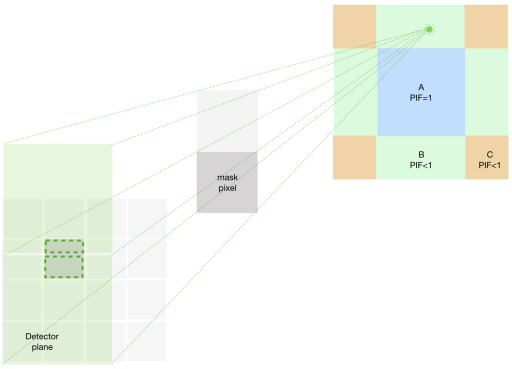

(A) The illumination of a pixel lying in region B through two adjacent open mask pixels

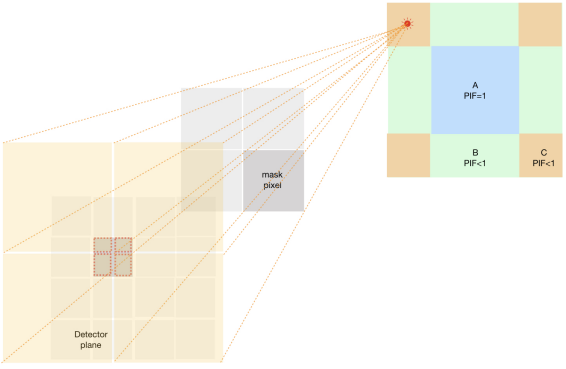

(B) The illumination of a pixel lying in region C through four adjacent open mask pixels

FIGURE 3.5: Highlighted in blue, green and orange, the regions of different PIF of a specific detector pixel through the mask pixel. The mask and detector pixel under consideration are drawn in a darker gray. The pictures illustrate how the detector pixel under consideration is fully illuminated through more than one mask pixel.

$$SPP^{l,m}_{p_m}(i,j) = \begin{cases} 1, & \text{if pixel i, j is in A} \\ 0.5, & \text{if pixel i, j is in B} \\ 0.25, & \text{if voxel i, j is C} \\ 0, & \text{if } p_m \text{ is closed} \end{cases} . \tag{3.3}$$

This means that if sky pixel i, j fully illuminates detector pixel l, m, $SPP^{l,m}(i,j)$ is given by either:

- A single contribution = 1
- The sum of 2 factors = 0.5
- The sum of 4 factors = 0.25

and can not be greater than 1. Conversely, a partially illuminated detector pixel will give $SPP^{l,m}(i,j)$ a value <1. It is worth acknowledging that equation 3.3 is an approximation and does not take into account the exact degree of illumination of each detector pixel, but correctly accounts for the contribution of each mask pixel to the visibility of the FOV.

3.2.2 Equivalence between Back-Projection and Cross-Correlation

In order to prove the validity of the back-projection method and its equivalence to cross-correlation, it is a useful exercise to consider a pointing observation to simplify the scenario and take the movement of the telescope axis out of the equation. The results can then be generalised to slew observations. When a detector image is formed, the back-projection sky map is obtained through the addition of the SPPs weighted by the number of counts in each detector pixel, according to:

$$S(i,j) = \sum_{l,m} SPP^{l,m}(i,j) C_{l,m} \tag{3.4}$$

where i, j represent the pixels of the final sky image S and C is the number of counts in the detector pixel identified by l, m. There are similarities between equation 3.4 and the 2D deconvolution formula

$$S(i,j) = \sum_{l,m} G_{i+l,j+m} C_{l,m} \tag{3.5}$$

which will be further discussed in this section.

It is useful to consider a single term in the sum in equation 3.5, corresponding to a certain detector pixel l, m. The shift between $G_{i,j}$ and $G_{i+l,j+m}$ is equal to the distance of the detector pixel l, m from the pixel $0, 0$. Figure 3.6 shows, in a 1D cross section, that shifting G by a certain number of detector pixel size lengths lP_D is equivalent to considering a projected mask pattern on the sky where the centre of the mask pattern is translated by an angle θ. This means that performing a traditional cross-correlation in the detector plane and rebinning the final image to fit the PCFOV of the telescope is equivalent to back projection, which acts directly in the sky plane. It is also possible to visualise the equivalence by expanding the sum in 3.5, separating the contributions from each detector pixel

$$S(i,j) = \sum_{l,m} S^{l,m}(i,j) \tag{3.6}$$

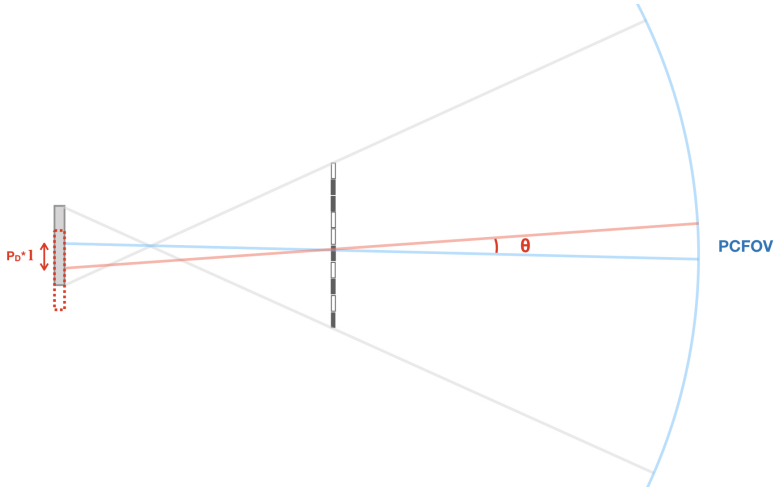

FIGURE 3.6: Equivalence between cross-correlation and back-projection. Shifting the deconvolution array G by a certain number of detector pixel size lengths lP_D is equivalent to considering a projected mask pattern on the sky where the centre of the mask pattern is translated by an angle θ.

where

$$S^{l,m}(i,j) = G_{i+l,j+m}C_{l,m} = \underbrace{G_{i+l,j+m} + G_{i+l,j+m} + \cdots + G_{i+l,j+m}}_{C_{l,m} \text{ times}} \tag{3.7}$$

The single term of this sum is nothing but the SPP calculated in section 3.2.1 and the two sums are equivalent. The difference between the two methods comes into play when a photon-by-photon reconstruction is needed. This occurs when the CA camera (telescope) is in a continuous motion. The knowledge of the pointing direction of the camera and the location of the photon detection allow the accumulation of an image by back projection of each detected photon to all the regions of space that could have hosted its emission. This is equivalent to accumulating shadowgrams for a time t$\rightarrow$ 0, or until each 'shadowgram' has a single photon detection, calculating a cross-correlation images for each shadowgram, and then producing a mosaic of all the images obtained this way. Since the standard INTEGRAL software does not implement a similar reconstruction, the analysis of slew data presented in chapter 5 have been processed photon by photon with a software designed over the course of the project from very low level data. OSA was used only to obtain calibration data from the intermediate stages of IBIS analysis up to the binning stage, such as photon energy, detector efficiency or dead time.

3.2.3 Balancing Back-Projection Images

The equivalence between cross-correlation and back-projection also means that the images obtained by BP can be and need to be balanced in the same way as cross-correlation images are. This can be done by using the following construction for $SPP^{l,m}_{p_m}$, where B is defined in 2.5

The back-projection equivalents of G^+ and G^- are calculated similarly to SPP_{p_m}, with reference to figures 3.3a, 3.3b, 3.3c for regions A, B and C of partial illumination of a detector pixel:

$$SPP^{(+)l,m}_{p_m}(i,j) = \begin{cases} 0, & \text{if } p_m \text{ is closed} \\ 1, & \text{if sky pixel i, j is in A (if } p_m \text{ is open)} \\ 0.5, & \text{if sky pixel i, j is in B (if } p_m \text{ is open)} \\ 0.25, & \text{if voxel i, j is in C (if } p_m \text{ is open)} \end{cases} \tag{3.8}$$

$$SPP^{(-)l,m}_{p_m}(i,j) = \begin{cases} 0, & \text{if } p_m \text{ is open} \\ 1, & \text{if sky pixel i, j is in A (if } p_m \text{ is closed)} \\ 0.5, & \text{if sky pixel i, j is in B (if } p_m \text{ is closed)} \\ 0.25, & \text{if voxel i, j is in C (if } p_m \text{ is closed)} \end{cases} \tag{3.9}$$

$SPP^{l,m}$ in its balanced version is then constructed as

$$SPP^{l,m}(i,j) = \sum_{p_m} SPP^{(+)l,m}_{p_m}(i,j) - B_{i,j} \sum_{p_m} SPP^{(-)l,m}_{p_m}(i,j) \tag{3.10}$$

The way to interpret equation 3.8 and 3.9 is that, while one needs to project back through the open pixels of the mask in order to calculate the positive part of the SPP, the negative part part of it is calculated by projecting back 'negative visibility' to the sky through the closed pixels. It is important to clarify that there is no such thing as 'negative visibility', just as much as there is no such thing as 'negative probability' that a photon could have been emitted in a region of the sky blocked by the mask. Balancing is a technique that is applied to cross-correlation images to artificially suppress background due to non-zero correlation in non-source positions of the FOV(18).

The Balancing Array

The back-projection equivalent of the balancing array defined in equation 2.5 can also be calculated from $SPP^{(+)}$ and $SPP^{(-)}$. By definition $B(i,j)$ is the ratio between $n^+(i,j)$ and $n^-(i,j)$. Since $n^+(i,j)$ is the number of detector pixels that can observe sky pixel i,j through the mask, it can be calculated as

$$n^+(i,j) = \sum_{l,m} SPP^{(+)l,m} \tag{3.11}$$

from the definition of $SPP^{(+)}$. In the same way

$$n^-(i,j) = \sum_{l,m} SPP^{(-)l,m} \tag{3.12}$$

$B(i,j)$ is simply calculated by dividing element by element the two arrays $n^+(i,j)$ and $n^-(i,j)$.

3.2.4 Variance Single Pixel Projections

Analogous arguments can be made to define the 'single pixel variance' (SPV) similarly to $SPP^{l,m}(i,j)$ in equation 3.10:

$$SPV^{l,m}(i,j) = \left(SPP^{(+)l,m}(i,j)\right)^2 + B(i,j)^2 \left(SPP^{(-)l,m}(i,j)\right)^2 \tag{3.13}$$

The Variance map can then be obtained by accumulating a number of contributions from each detector pixel which registered a gamma detection during an observation.

3.3 Implementation of The Back Projection Algorithm to IBIS/ISGRI data

The image reconstruction consists of two main steps: the creation of a list of events in an appropriate format and the projection of each event from the event list through the openings in the coded mask.

3.3.1 Event List Creation

Events Selection

Although back-projection processes the detector data photon by photon, it was convenient to implement the algorithm so that it could use the intermediate outputs of the first stages of OSA data reduction for the application of instrument calibration and correction. In the first place, the detected photons are selected according to quality criteria. These are the standard selection criteria applied by OSA to pointing data.

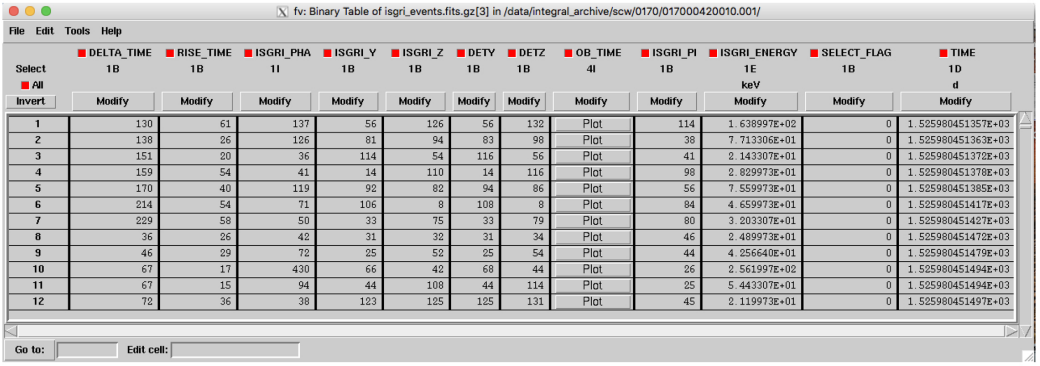

	DELTA_TIME	RISE_TIME	ISGRI_PHA	ISGRI_Y	ISGRI_Z	DETY	DETZ	OB_TIME	ISGRI_PI	ISGRI_ENERGY	SELECT_FLAG	TIME
	1B	1B	1I	1B	1B	1B	1B	4I	1B	1E keV	1B	1D d
1	130	61	137	56	126	56	132	Plot	114	1.638997E+02	0	1.525980451357E+03
2	138	26	126	81	94	83	98	Plot	38	7.713306E+01	0	1.525980451363E+03
3	151	20	36	114	54	116	56	Plot	41	2.143307E+01	0	1.525980451372E+03
4	159	54	41	14	110	14	116	Plot	98	2.829973E+01	0	1.525980451378E+03
5	170	40	119	92	82	94	86	Plot	56	7.559973E+01	0	1.525980451385E+03
6	214	54	71	106	8	108	8	Plot	84	4.659973E+01	0	1.525980451417E+03
7	229	58	50	33	75	33	79	Plot	80	3.203307E+01	0	1.525980451427E+03
8	36	26	42	31	32	31	34	Plot	46	2.489973E+01	0	1.525980451472E+03
9	46	29	72	25	52	25	54	Plot	44	4.256640E+01	0	1.525980451479E+03
10	67	17	430	66	42	68	44	Plot	26	2.561997E+02	0	1.525980451494E+03
11	67	15	94	44	108	44	114	Plot	25	5.443307E+01	0	1.525980451494E+03
12	72	36	38	123	125	125	131	Plot	45	2.119973E+01	0	1.525980451497E+03

FIGURE 3.7: Example of an event list from IBIS/ISGRI science window 17000420010 as shown with the software 'FITSviewer'. Each row of the table represents a photon detection. For each photon, several pieces of information are recorded, such as position on the detector, detection time and energy

The list of all detected photons is stored in the 'scw' data repository, in the form of a fits table extension called 'ISGR-EVTS-ALL'. The event list is a table including the details of all the events in each observation. Figure 3.7 displays a section of such a table. The columns store data recorded for each detected event, among which:

- **ISGRI Y, DETY** - y coordinate of the detector pixel
- **ISGRI Z, DETZ** - z coordinate of the detector pixel
- **SELECT FLAG** - Selection flag (1 if the pixel is flagged as noisy)
- **TIME** - detection time in Integral Julian Date (IJD). IJD is defined as MJD−51544.0, where MJD is the Modified Julian Date(34).

The event list table also includes additional event data such as pulse rise time and amplitude in the detector. The energy of each event in keV is also calculated and stored in the event list. In order to create an event list containing the appropriate information to perform back projection reconstruction, a copy of this list is created and three selection criteria are applied by the addition of a selection flag column which assumes value 0 if the event is accepted and 1 if the event is rejected. The selection criteria are:

- All the events with energy falling below the low threshold limit for the orbit are rejected
- All the events falling outside of the good time intervals are rejected
- All the events rejected by the correction stage of OSA are also rejected. To identify these events, ibis science analysis is run on the raw data. The output of the correction stage is a corrected event list called 'ISGR-EVTS-COR' which has a selection flag column labeling all the events rejected by the correction stage of OSA.

The result of this stage is a pre-processed event list, where all the events that do not pass the selection criteria are labelled and will be ignored in the subsequent stages.

Correction for Inactive Detector Areas

The inactive areas between detector modules need to be filled with simulated events to avoid the formation of artifacts in the final image, due to the presence of areas with zero counts in the middle of the shadowgram. The gaps between detector modules are visible in the shadowgram in figure 3.1. Similarly to the way OSA implements this correction, the back-projection algorithm divides the gaps between modules into equivalent pixels and assigns to each of them a number of simulated events. A number of simulated events equal to

$$N_{sim} = \overline{D} * N_{gaps} \tag{3.14}$$

is produced, where $\overline{D}$ is the average detector counts and N_{gaps} is the number of fictitious pixels in the gaps. The value of N_{sim} is rounded down to the nearest integer. A random detection time within the GTIs and position within the gaps is assigned to each simulated event. This additional simulated event list is processed in the same way as the event list of physical detections. This is an approximation which will lead to some artefacts in the final images. These artefacts are also present in the

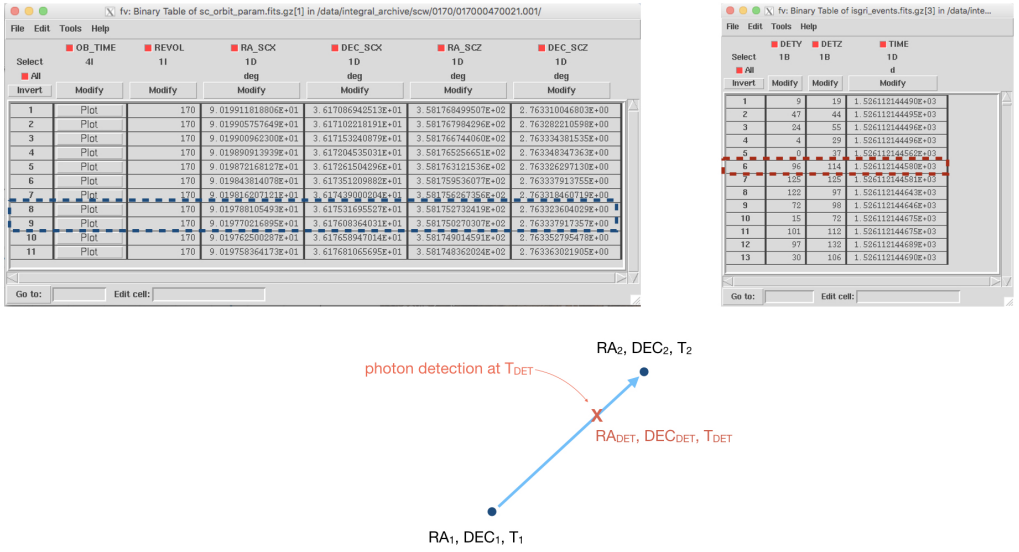

FIGURE 3.8: Calculation by interpolation of the instantanoeus ISGRI pointing direction at the time of each detection

OSA cross-correlation images before the correction stage is applied. A better choice to correct the detector image would be the use of the local mean of the detector plane. Using the local mean would be more accurate when sources illuminate only part of the detector (sources in the PCFOV) or to reproduce the largest features of the mask pattern on the inactive pixel areas.

Calculation of ISGRI Instantaneous Pointing Direction

In order to trace the possible origin of a detected photon through the mask openings two pieces of information are needed: the position of the interaction on the detector plane and the pointing direction of the telescope at the time of detection. The first piece of information is stored in the pre-processed event list. In order to calculate the instantaneous pointing direction of the telescope at the time of detection a second data file is needed, which is also part of the *scw* data repository and is the orbit parameter file. An extract from the orbit parameter table is shown in figure 3.8 and includes data regarding the operation of the telescope. The direction of the x and z axes of INTEGRAL is reported every eight seconds throughout the duration of the science window and stored in a file called 'INTL-ORBI-SCP'. Assuming that the pointing direction is changing with constant speed in each eight seconds interval, the instantaneous pointing direction is calculated by interpolation within these time intervals. It should be pointed out that the values of the pointing direction stored in the INTL-ORBI-SCP table is referred to the star tracker system, and due to the presence of a 10 arcmin misalignment between the star tracker and each of the

telescope instruments, a small correction needs to be applied before interpolation in order to correctly reconstruct the position of sources. Figure 3.9 represent the three reference frames that are at play: the world, the star tracker and ISGRI. In ISGRI reference frame, z identifies the pointing axis, while the y-x plane is the detector plane. The correction for the misalignment consists of applying a rotation in the calculated pointing direction, which is encoded in a rotation matrix between ISGRI and the equatorial frame of reference. This matrix is stored in the *aux* database. The result of this step is an updated event list, where four columns have been added, displaying ra and dec of the x and z axes of ISGRI at the time of each detection.

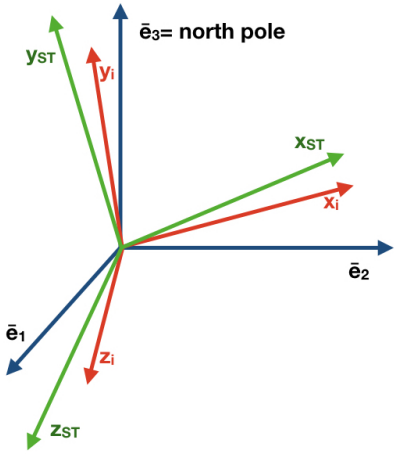

FIGURE 3.9: Misalignment between the star tracker system (in green) and ISGRI axis (in red). The relative orientation between the two systems is stored as a 3x3 rotation matrix in the aux data repository of the archive

3.3.2 Photon-by-Photon Back-Projection

Once a set of SPP and SPV and the effective exposure have been computed and stored in memory and after the construction of an event list, a series of steps are followed for each valid event in order to obtain a set of sky maps. First the event parameters useful for the analysis are read from the *.fits* event table. These parameters include pixel coordinates l, m and information on the ISGRI pointing direction at the time of detection ra_x , dec_x, ra_z, dec_z. The efficiency of pixel l, m in the science window analysed is read from the corrected shadowgram produced by OSA. The efficiency is calculated with equation 2.2 during the *binning* stage of the OSA analysis. Finally, $SPP^{l,m}$, $SPV^{l,m}$ and the effective exposure are loaded from memory.

$SPP^{l,m}$ and $SPV^{l,m}$ as they have been loaded from memory are expressed in polar coordinates in the ISGRI frame of reference, where $(\theta, \phi)=(0,0)$ is the telescope axis.

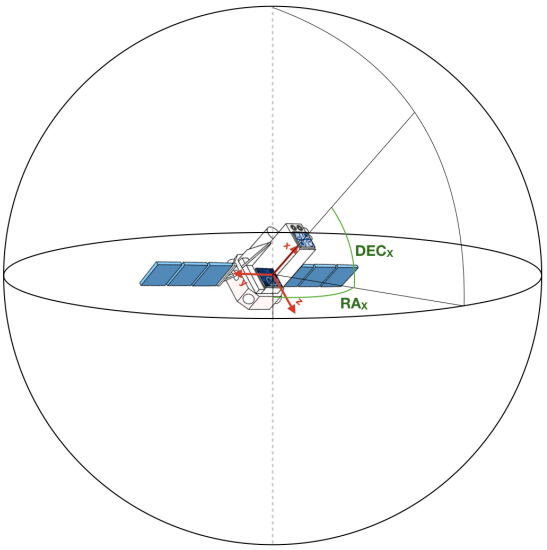

FIGURE 3.10: Representation of INTEGRAL frame of reference (in red) and the equatorial frame of reference (in green). The pointing axis is the x-axis in the telescope reference frame, while the detector surface lies in the y-z plane. RA_x and DEC_x are the equatorial coordinates of the telescope pointing direction

In order to build sky maps it is necessary to project the coordinates of the SPPs and SPVs onto a sky map in equatorial coordinates RA and DEC, considering the instantaneous pointing direction of the telescope. This change in frame of reference is applied with the following steps, which are repeated for every pixel in $SPP^{l,m}(i,j)$:

1. Calculate the components of the unity vectors corresponding to the coordinates of the four corners of each pixel i,j in $SPP^{l,m}(i,j)$ and $SPV^{l,m}(i,j)$.
2. Apply a change in reference frame, expressed by the rotation matrix:

$$\begin{pmatrix} x_{eq} \\ y_{eq} \\ z_{eq} \end{pmatrix} = M \begin{pmatrix} x_{ISGRI} \\ y_{ISGRI} \\ z_{ISGRI} \end{pmatrix} \tag{3.15}$$

where

$$M = \begin{pmatrix} \cos ra_x \cos dec_x & \begin{array}{l} -\sin ra_x \cos dec_x \sin dec_z \\ +\sin dec_z \sin ra_z \cos dec_z \end{array} & \cos ra_z \cos dec_z \\ \sin ra_x \cos dec_x & \begin{array}{l} -\sin dec_x \cos ra_z \cos dec_z \\ +\cos ra_x \cos dec_x \sin dec_z \end{array} & \sin ra_z \cos dec_z \\ \sin dec_x & \begin{array}{l} -\cos ra_x \cos dec_x \sin ra_z \cos dec_z \\ +\sin ra_x \cos dec_x \cos ra_z \cos dec_z \end{array} & \sin dec_z \end{pmatrix} \tag{3.16}$$

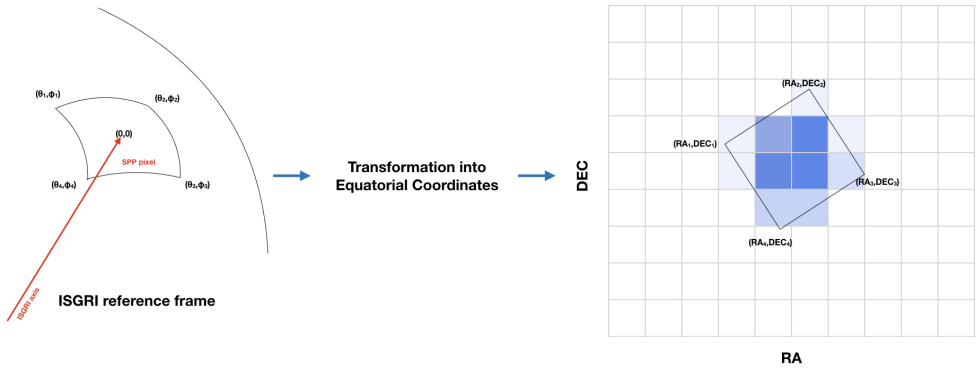

FIGURE 3.11: Reprojection of a single pixel of $SPP^{l,m}$ onto the empty sky map. The coordinates of the pixel coordinates are transformed into equatorial coordinates, and the sky map is filled with the value $SPP^{l,m}(i,j)$

In equation 3.16 (x_{eq}, y_{eq}, z_{eq}) is the unit vector describing directions in the equatorial reference frame and $(x_{ISGRI}, y_{ISGRI}, z_{ISGRI})$ the unit vector describing directions in the ISGRI reference frame. ra_x, dec_x and ra_z, dec_z are the coordinates of the IBIS pointing axis (x axis) and z axis. Figure 3.10 represents the correspondence between ISGRI frame of reference, with the pointing axis aligned with the x-axis, and the equatorial frame of reference. The equatorial coordinates of the pointing axis are indicated as RA_x and DEC_x.

3. Calculate *ra* and *dec* corresponding to the direction of (x_{eq}, y_{eq}, z_{eq}). These are the four corners of the pixel in the equatorial reference frame

4. Fill the pixels of the intensity all-sky map the value of $SPP^{l,m}(i,j)$ and the pixels of the variance all-sky map with the value of $SPV^{l,m}(i,j)$. This is done with a recursive algorithm that calculates the degree of overlap between the all-sky map pixel and the pixel from $SPP^{l,m}(i,j)$ that is being projected onto it

The process of reprojecting each pixel of $SPP^{l,m}$ onto the empty sky map is outlined in the diagram in figure 3.11. The result of these steps is an all-sky intensity map and an all-sky variance map with the projection of a single event to the regions in the sky that it could have come from, with balancing factors applied. These steps are repeated for all the valid events in the event list.

3.3.3 Exposure Maps

In order to compute sky maps that can be converted to count *rate* units it is necessary to produce exposure maps of the sky for the observation under analysis. While exposure maps are normally built by OSA for static observations, slew exposure maps need to consider the motion of the telescope axis as the instruments are collecting data. Figure 3.12 shows the exposure that results: if IBIS is pointing in a certain direction (*theta*,*phi*)=(0,0) for one second the FCFOV is characterised by 1 second exposure. The exposure of areas in the PCFOV will be < 1, according to the ratio of the detector area that is used. This concept is called effective exposure. The total exposure map of an observation is the sum of all such exposure projections onto an empty sky image as the telescope slews from one pointing to the next. The exposure projection is computed as

$$E(i,j) = \sum_{l,m} SPP^{(+)l,m} \tag{3.17}$$

$E(i,j)$ has the same value (and interpretation) as n^+. It represents the total number of detector pixels that can observe sky position (i,j). E(i,j) is then normalised to 1

$$\overline{E(i,j)} = \frac{E(i,j)}{n^+(FCFOV)} = \frac{E(i,j)}{0.5 \cdot N_m} \tag{3.18}$$

From an algorithm point of view, the exposure is projected back in exactly the same way as the intensity is. For each event the exposure projection is loaded from memory and multiplied by an appropriate time interval which is determined as follows:

- If the event occurs within a GTI the exposure projection is multiplied by the time interval between the current event and the following valid one
- If the event is the first or last event of a GTI the exposure projection is multiplied by the time interval between the event and the boundary of the GTI

The exposure projection is then rotated to match the instantaneous pointing direction of the telescope and its contribution is added to an empty sky image following the same method as the $SPPs$ and SPVs. The result is an all-sky map of the effective exposure of the telescope during a slew science window.

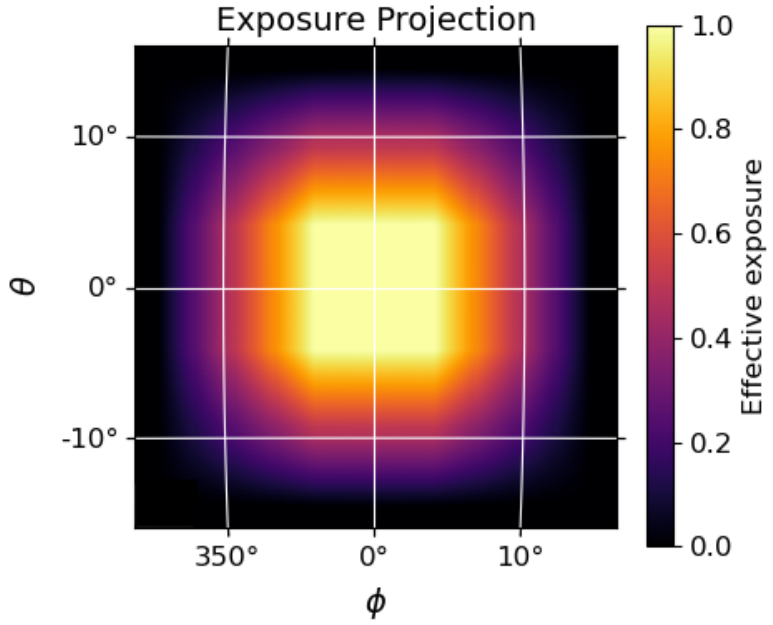

FIGURE 3.12: Effective exposure projection

3.3.4 Products of the Slew Data Analysis

The back-projection code for IBIS/ISGRI data outputs a set of four images stored as extensions of a *.fits* file for each science window. These images are: intensity, variance, significance and exposure. The significance map is simply calculated as the pixel by pixel division between the intensity and the square root variance map. Slew science window maps can be mosaicked in the same way as pointing observations are, with proper weighting with variance and exposure time. The first astronomical image that was produced to test the algorithm is an image of the Crab Nebula, a Supernova Remnant which is one of the strongest X-ray sources observable in the sky. Since its intensity is considered to be constant, a great number of X- and gamma-ray telescopes (including INTEGRAL) have used and continue to use observations of this source to perform their calibration. The data sets that were used to test the success of the back projection method are indeed part of calibration observations of the Crab. The first observation is from one of the early orbits, orbit 0170, which was performed in June 2004 and included 27ks of observation of the Crab(35). The second observation was performed in October 2014 and covers two orbit, 1461 and 1462, with a total exposure of around 39ks. The Crab was chosen as a test source also because, contrary to other persistent sources bright in the X-rays, the Crab is the only X-ray source in its region, offering an almost ideal test scenario with one single source in the FOV.

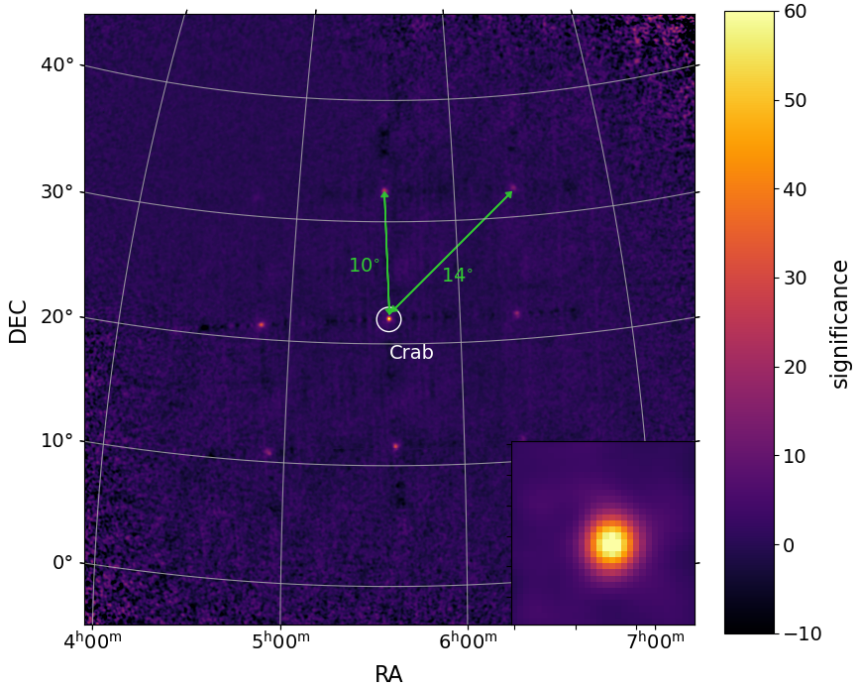

FIGURE 3.13: Significance maps of the regions around the Crab Nebula using science windows from orbit 1461-62. The image shows a peak in significance in the position corresponding to the Crab, as well as 8 ghost images around the main peak

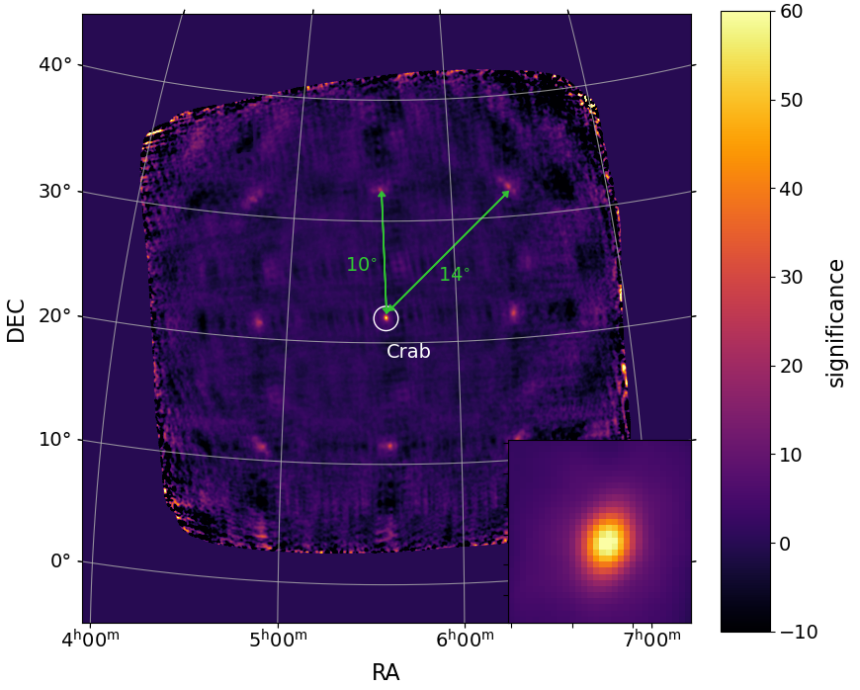

FIGURE 3.14: Significance maps of the regions around the Crab Nebula using science windows from orbit 0170. The image show a peak in significance in the position corresponding to the Crab, as well as 8 ghost images around the main peak(35)

Figures 3.13 and 3.14 show the final significance images made with the two Crab observations. Both images show a clear peak in the Crab position with a significance of — for orbit 0170 and — for orbits 1461/62. In addition, eight ghost images are placed at symmetrical positions around the main source. It is important to emphasize that these spurious sources are not generated by back-projection itself. On the contrary, they are due to the repeated nature of the mask pattern and appear in cross-correlation images as well, before the correction stages of OSA. OSA is able to suppress ghost images by operating a cross-check between a catalogue of positions of known sources and possible sources found in the images. In fact, when a previously unknown source is found in ISGRI images, it does presents ghosts, since OSA fails to suppress them. Results from the analysis of science observations made of a stack of science windows from several orbits will be presented in chapter 4.

3.3.5 CUDA Implementation of Back-Projection

The code which runs the analysis has been first implemented in C++. The total computing time associated with back projection can be divided into two tasks. First, the construction of the SPPs, SPVs and exposures, then mapping of these projections onto the sky. A code written in Python computes the projections in the telescope's reference frame by using purely geometrical considerations. Once projections have been computed, they need to be mapped on an empty all-sky map. This operation, described in section 3.3.2, took about 2 seconds per photon. On average, a slew science window includes around 30000 events. This means that on average the computing time to produce an image of a single science window would be 16.7 hours. After the first prototype, which worked with reduced data sets of a few hundred photons, it has been decided to use GPUs to reduce the computing time. The code that implements the back projection algorithm, processing each photon in the event list, was written in C++. The function that adds the contribution of each photon to the sky map runs on a GPU by means of the computing platform CUDA distributed by NVIDIA, which allows the definition of C++ functions, called kernels, that can be executed on the GPU. Kernels define a number of threads, which take a 1D or 2D array as an input and perform a series of operations on a single element of the input array, executing them in parallel on a GPU. The computation was split between four servers each equipped with a NVIDIA GeForce RTX 2080 GPUs. A single science window at a time was processed by each server. For each science window, an event list is first produced on the CPU. Then, space for the output image is allocated in the GPU memory. The all-sky map that will host the output image is an 8000x8000 pixel array. Then, for each event the appropriate SPP, SVP and EP are loaded from the HDD and copied to the GPU memory space. Only at this stage the kernel is

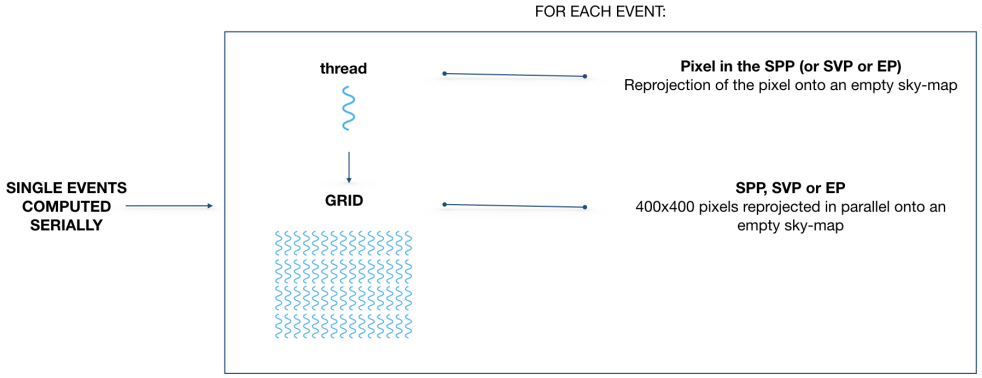

FIGURE 3.15: Structure of the kernel used for reprojection onto the sky. Each thread reprojects one of the 400x400 pixels in SPP, SVP and EP. By processing all of the pixels in parallel, the computing time decreased 400 times

then launched. The diagram in figure 3.15 displays how the algorithm was implemented for a parallel execution and the structure of the kernel: each thread of the kernel performs the reprojection onto the sky map of one of the 400x400 pixels in each of the three arrays (SPP, SVP and EP). With the parallel implementation, the performance has improved (from $\sim$2 seconds/photon to $\sim$50 ms/photon). This is absolutely fundamental for the production of a big survey. In fact, the total number of slew events recorded by INTEGRAL is estimated to be of the order of magnitude of 10^{10}. Further details on the performance of this implementation can be found in chapter 4.

Chapter 4

An IBIS/ISGRI Slew Survey Prototype

4.1 The Potential of a Slew Survey

The previous chapters of this thesis illustrated the method that has been used to extract images from IBIS/ISGRI slew data and the motivation for pursuing this challenging task. This chapter focuses on the possibility to obtain scientific products from slew data and is articulated in three sections. The first section describes the potential of a slew data survey, by comparing the slew exposure of the sky to the pointing exposure. The second section presents a demo of the slew survey with a reduced data set of ten orbits. The chapter is closed with a section that describes the work that still needs to be carried out to fully implement slew data analysis of large data sets.

4.2 Sky Distribution of the Slew Exposure

One of the key motivations for performing a slew survey is that it can provide exposure of sky regions that are not well covered by pointings. Figures 4.1 and 4.2 represent the pointing and slew exposure maps of the first 2000 orbits of the INTEGRAL satellite. The first was obtained from the INTEGRAL Announcement of Opportunity (AO-15), which covers data up to the end of 2017(36). The second was evaluated from the orbit parameters file for each slew science window, accessed from the INTEGRAL data archive. Both maps present highest value in the region of the galactic plane, with slew exposure being approximately one order of magnitude lower than its pointing counterpart. The apparent gap in the data in figure 4.2

is resulting from the reprojection of the slew exposure maps, originally computed in the equatorial frame of reference, into a galactic frame of reference. Figure 4.3 represents the ratio between slew exposure and pointing exposure of the first 2000 orbits. It is possible to notice that around the galactic plane the value of the ratio is approximately 0.1, which is in line with slews representing around 11% of the total observing time. However, moving away from the galactic plane, areas where slew observations constitute a significant portion of the total observing time appear, and even small regions where the ratio is greater than 1, indicating that the slew exposure is higher than its pointing counterpart.

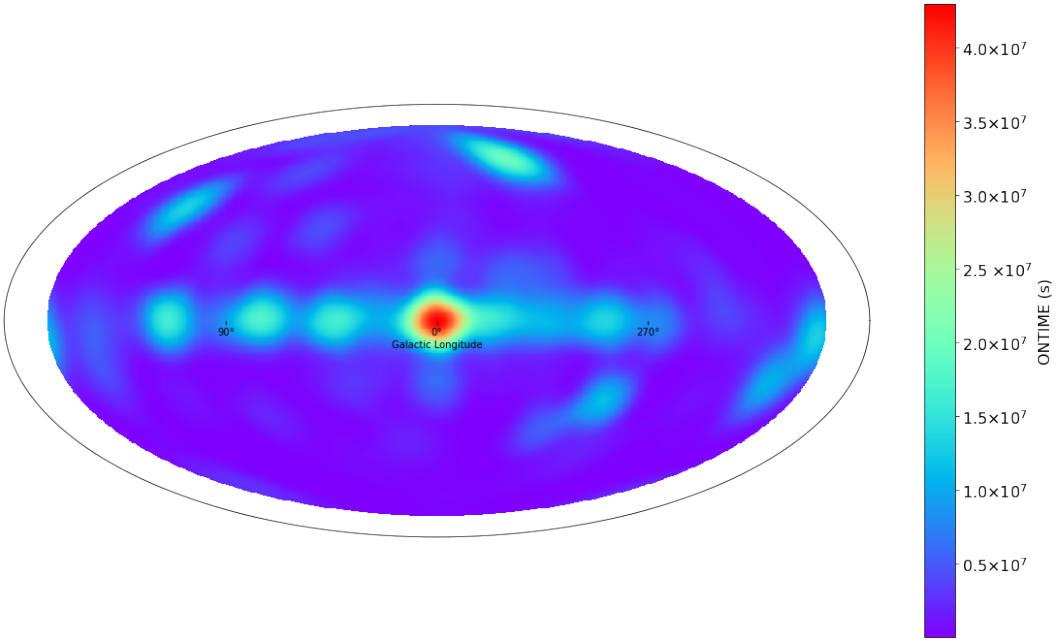

FIGURE 4.1: Exposure map of the pointing INTEGRAL/IBIS data for orbits 0 to 2000. This map was obtained from the INTEGRAL Announcement of Opportunity 15 (AO-15) (36)

Figure 4.4 represents the ratio of the sky covered with pointing and slew observations above a certain exposure time. This plots highlights again how, in areas of the sky that are not visited often (lower exposure values), slew observation constitute a significant fraction of the total amount of INTEGRAL data. Some small areas even present an exposure ratio between pointings and slews close to 1, which means that approximately half of the data available for those regions is composed of slew observations. Figure 4.4 provides a second way of looking at the exposure data. The plot represents the percentage of the sky observed at different levels of exposure. The plot confirms that observing time spent in slew mode is approximately 10% of the time spent in pointing mode.

It is worth emphasizing that, although these maps provide a good idea of the quantity of data that could become available if a slew analysis tool is developed, they are

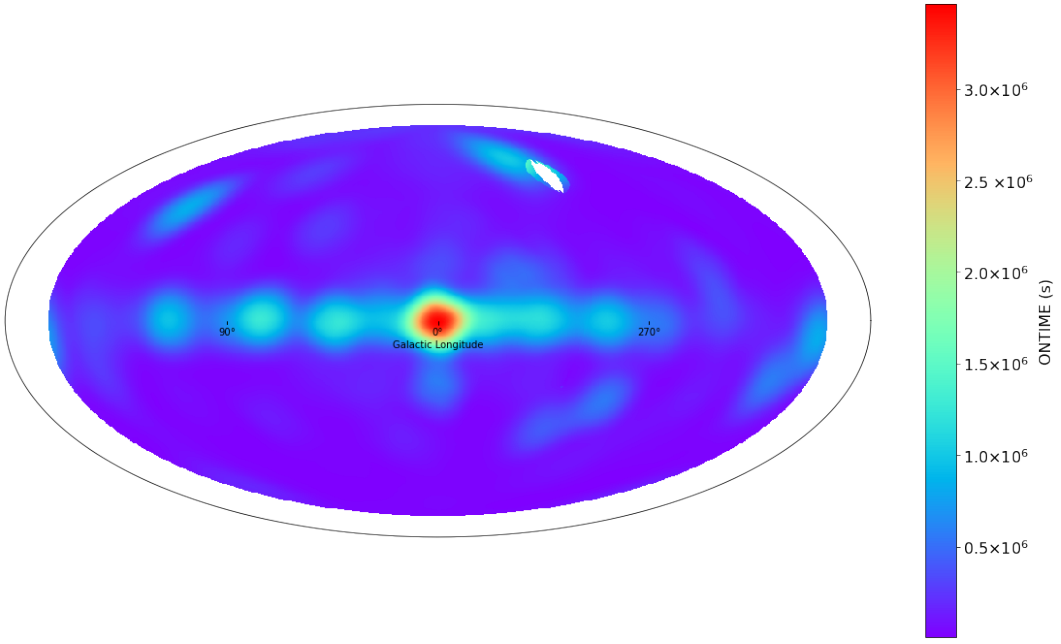

FIGURE 4.2: Exposure map of the slew INTEGRAL/IBIS data for orbits 0 to 2000. This map was calculated from the orbit parameters available in archival data. A local averaging algorithm has been used to address the discontinuity around ra=0 when converting from equatorial to galactic reference frame. This transformation was performed to display the map in the same coordinates as the pointings exposure map, directly downloaded from the INTEGRAL Announcement of Opportunity 15 (AO-15) (36)

not comparable to the exposure maps computed with OSA. Figures 4.1 and 4.2 are 'ONTIME' maps, which represent the amount of time the telescope spent observing every sky pixel. Since version 10, OSA produces 'true' exposure maps, which have much lower values because they account account for detector dead time, the transparency of the mask and various vignetting effects from the mask supporting structures (25).

4.3 A Prototype for a Slew Data All-Sky Survey

A reduced set of observations was selected to be processed with the back-projection algorithm and be a prototype to test its imaging capabilities. The data sample consists of 11 INTEGRAL orbits, from 973 to 983, and covers a time period of one month (October 2010). This 11 orbits data set was chosen for multiple reasons. First of all the data sample is extremely varied in terms of types of slew science windows: it includes long slews where the orientation of the telescope axis varied at high speed as well as really short and almost static slews between pointings forming a dithering pattern. The second reason for this choice of data for a first multi-orbit test relies in the targets of the observations. The observation of several bright sources during

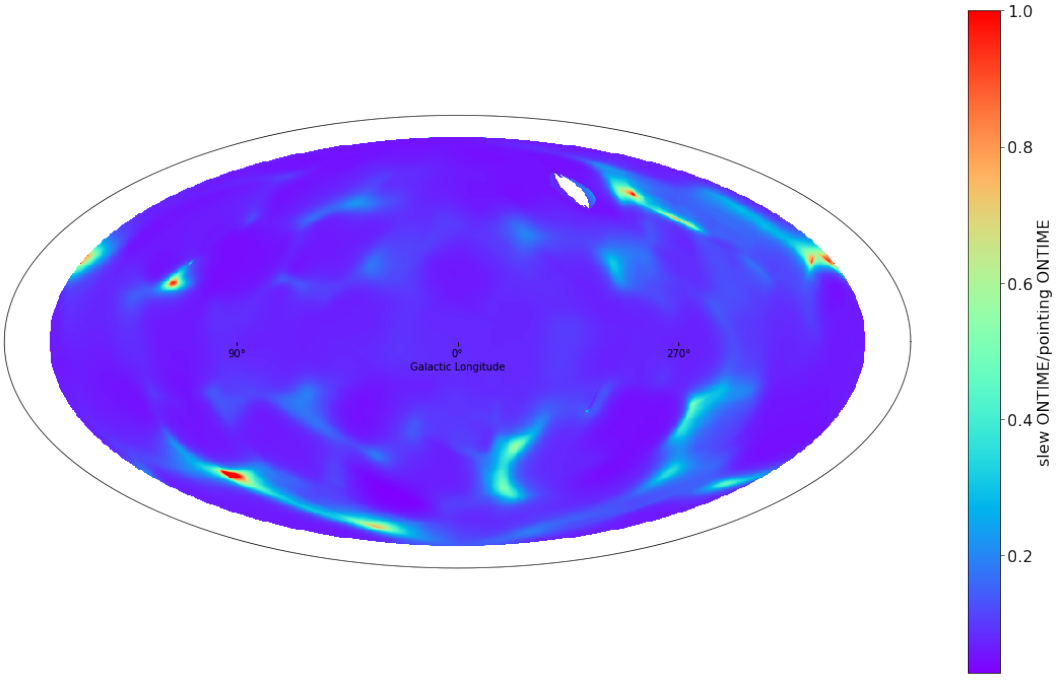

FIGURE 4.3: Ratio between pointing and slew exposure maps for orbits 0 to 2000. When moving away from the galactic plane, slew observations constitute a significant portion of INTEGRAL observing time

these orbits makes this sample a good test bench for the capabilities of the back-projection reconstruction. This time window also presents a high level of overlap with Swift/BAT observations. This overlap makes this data set ideal to test an integrated gamma-ray survey including ISGRI pointings, slews and Swift/BAT observations, although this particular application is out of the scope of this thesis. Figure 4.5 shows the motion of the pointing direction of the telescope during one of the orbits of the data set. Pointing observations are represented by a dark dots, while the trajectory of the pointing direction during slews is traced with a pale blue line. Orbit 975, which is fairly typical in terms of observation schedule, starts with observation of the outer galactic region composed of a series of pointings performed in a line at $l = -150^{\circ}$, followed by an observation of the galactic bulge in an hexagonal pattern. Figure 4.6 shows the exposure map of the orbit: the outer galactic region has an exposure of approximately 3 ks, while the galactic bulge was observed for 960 s during orbit 975.

4.3.1 Exposure Map of the Prototype Data Set

Figure 4.7 shows the total exposure for the slew science windows of the test data set. The total exposure time (calculated as the sum of the GTIs and thus equal to the ONTIME) is 150ks and 2.2Ms respectively for slews and pointings. The most observed

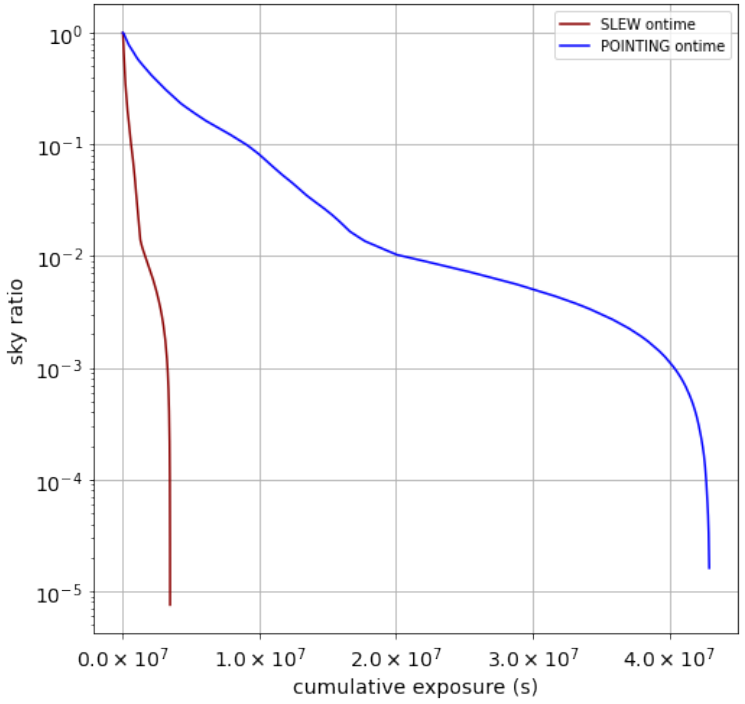

FIGURE 4.4: Fraction of the sky observed by ISGRI as a function of cumulative exposure. The fact that two curves have the same shape, but extend differently along the x-axis indicates that the time spent in slew modes sums up to approximately 10% of the time spent in pointing mode in the majority of the sky.

areas of the sky have an exposure of around 10ks, mostly composed by slow and short slews between pointings forming a dithering pattern around the same source. Some long fast slew are also present, with a coverage in the hundreds of seconds. A total of 945 science windows was processed, corresponding to approximately 6×10^7 back-projected events. For the preliminary analysis presented in this thesis, images were processed only in the 18-60 keV energy band, around the peak of the ISGRI detector sensitivity. The 18-60keV energy band is optimal for survey studies of X-ray binaries and AGN spectra, and for this reason is one of the key bands used in existing surveys with ISGRI(37; 38).

4.4 Producing a Mosaic Slew Sky Map

The back-projection reconstruction was applied to each science window of the data set. In OSA analysis for pointing observations, single science window images are produced and then averaged to obtain a high statistics mosaic. OSA creates images of the telescope's field of view for each static observation and creates a 'mosaic' by reprojecting each single science window image onto an empty sky map. The same process was followed for back-projection images of slew data. The only difference

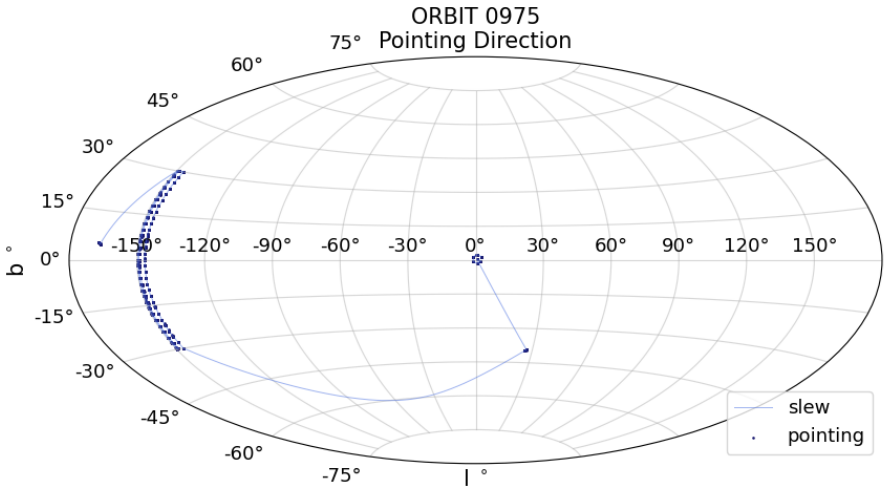

FIGURE 4.5: ISGRI pointing direction during orbit 975. The orbit starts with a series of observation of the outer galactic disk, followed by an hexagonal pattern observation of the galactic bulge

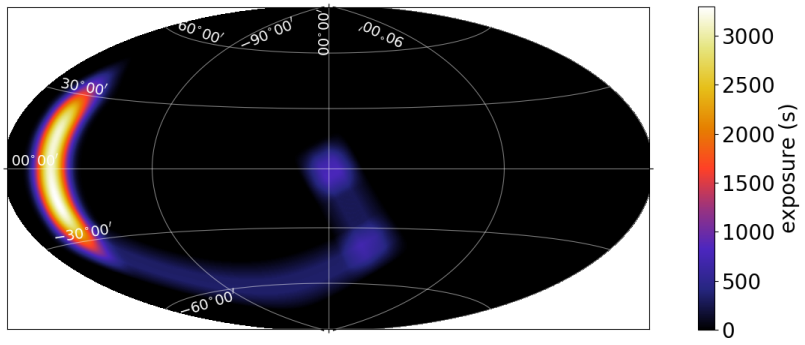

FIGURE 4.6: Exposure map of slew observations in orbit 975. The orbit includes a 3ks coverage the outer galactic region at l=215°, followed by 700s in the galactic centre

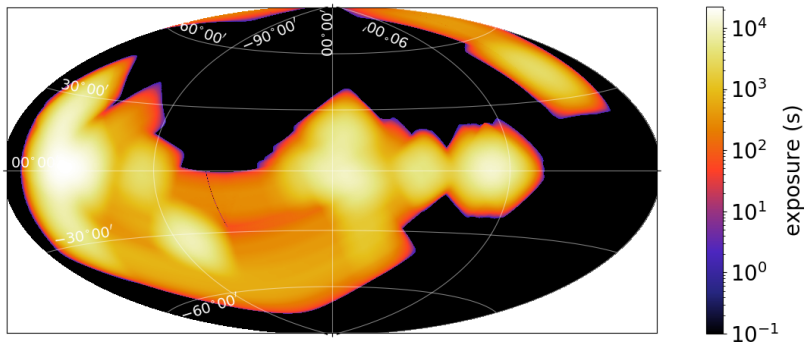

FIGURE 4.7: Total exposure (ONTIME) of orbits 973 to 983. The color bar is displayed in logarithmic scale to highlight the areas with lower exposure

is that, since the back-projection algorithm always projects detected events onto an empty map of the whole sky, it is sufficient to sum the single science window images after proper weighting with their variance and exposure since all the images are already in the same reference frame. However the term 'mosaic' will be used also for slew maps, in analogy with OSA analysis.

4.4.1 Intensity Maps

A total intensity map I was produced by simple pixel-by-pixel sum of the single science windows intensity maps.

$$I_{\mathrm{mosa}}(\mathrm{x},\mathrm{y}) = \sum_{\mathrm{scw}} I_{\mathrm{scw}}(\mathrm{x},\mathrm{y}) \tag{4.1}$$

In equation 4.1 x and y refer to the pixel of the sky map. It is possible to perform these operations simply pixel-by-pixel because the output of all the slew images is an all sky map in the same reference frame.

4.4.2 Exposure Maps

In a similar way, the exposure maps are calculated by adding together exposure maps from single science windows.

$$T_{\mathrm{mosa}}(\mathrm{x,y}) = \sum_{\mathrm{scw}} T_{\mathrm{scw}}(\mathrm{x,y}) \tag{4.2}$$

It is important to reiterate that exposures calculated in 4.2 are comparable to exposure maps processed with OSA, since they do not account for detector efficiency and various vignetting effects. They only indicate the time that the telescope spent observing each sky pixel if the observation fell inside a GTI.

4.4.3 Flux and Variance Maps

Flux maps for each science window are derived by dividing the intensity map by the exposure

$$F_{\mathrm{scw}}(\mathrm{x,y}) = \frac{I_{\mathrm{scw(x,y)}}}{T_{\mathrm{scw(x,y)}}} \tag{4.3}$$

In principle, since the peak in the deconvolution map is proportional to the number of detector counts from a source and the deconvolution is equivalent to back-projection, F_{scw} will be proportional, after proper calibration, to the detector count rate from a position in the sky. This is why in this thesis, the quantity in 4.3 is indicated and treated as an uncalibrated 'flux'.

The flux variance maps at a science window level were computed by simple error propagation dividing the variance maps obtained with 3.13 by the square of the exposure

$$\sigma^{2\,\mathrm{flux}}_{\mathrm{scw}}(\mathrm{x,y}) = \frac{V_{\mathrm{scw(x,y)}}}{T^2_{\mathrm{scw(x,y)}}} \tag{4.4}$$

The flux map of the whole observation period was then produced by simply averaging the single science windows map after properly weighting them with the variance maps $\sigma^2_{\mathrm{scw}} = V_{\mathrm{scw}}$:

$$F_{\mathrm{mosa}}(\mathrm{x,y}) = \frac{\sum_{\mathrm{scw}} F_{\mathrm{scw}}(\mathrm{x,y}) \frac{1}{\sigma^2_{\mathrm{scw}}(\mathrm{x,y})}}{\sum_{\mathrm{scw}} \frac{1}{\sigma^2_{\mathrm{scw}}(\mathrm{x,y})}} \tag{4.5}$$

and the mosaic variance map is calculated accordingly.

$$\sigma^2_{\mathrm{mosa}}(\mathrm{x,y}) = \frac{1}{\sum_{\mathrm{scw}} \frac{1}{\sigma^2_{\mathrm{scw}}(\mathrm{x,y})}} \tag{4.6}$$

In equations 4.5 and 4.6 σ_{scw} refers to the error on uncalibrated flux at a science window level, calculated with 4.4. In the same way σ_{mosa} refers to the error on the mosaic flux images.

4.4.4 Significance maps

The significance map for the mosaic image, expressing the flux in units of its standard deviations, is then calculated by dividing the mosaic flux map by its error, which is the square root of the mosaic variance map.

$$S_{\mathrm{mosa}}(\mathrm{x,y}) = \frac{F_{\mathrm{mosa}}(\mathrm{x,y})}{\sigma_{\mathrm{mosa}}(\mathrm{x,y})} \tag{4.7}$$

4.5 Results

It is interesting to compare the back-projection maps obtained from the slew science windows and the cross-correlation maps from the pointings performed in the same orbits. For comparison, a deconvolution sky map was computed by means of OSA from the same orbits.

4.5.1 Search for Excesses in the Significance Map

Pointing and slew significance maps were inspected with a tool that searches for peaks in the image (37). This tool is called 'peakfinder' and operates a search for peaks in three stages: it first selects the pixels in the image above a certain threshold and recursively searches for peak structures around them. The recursive search stops if the selected pixel falls below a certain threshold value or if the value increase, indicating that is is situated in a valley in the image. Selection criteria are applied to the identified peaks, to determine the likely sources. First, the centroids of the identified peaks are then calculated and compared to the local rms of the image, to reject peaks that are comparable to the noise level. The radius of the peak is evaluated and compared to a minimum threshold which depends on the maximum value.

In this work, peakfinder was tuned to identify peaks above 5σ detection and a total of 59 sources were identified in the pointings map. This threshold is similar to the 4.7σ threshold used to search maps in previouis works with larger data sets. Table 4.1 shows the ten brightest sources that were found, along with the significance of their detection and the local exposure of the observations around their position. The

Source	RA (deg)	DEC (deg)	pointing exposure(s)	slew exposure(s)	pointing significance (σ)	slew significance (σ)	pointing position offset (deg)	slew position offset (deg)
GRS 1915+105	288.802	10.942	37856	4762	520.434	52.985	0.006	0.035
Vela X-1	135.528	-40.555	37486	2846	427.660	31.217	0.001	0.048
Sco X-1	244.979	-15.646	14106	3155	419.467	44.959	0.005	0.128
Cyg X-1	299.585	35.201	30837	7705	338.566	40.446	0.004	0.083
Cyg X-3	308.112	40.954	48234	1184	243.8222	27.668	0.005	0.062
4U 1700-377	255.989	-37.842	24085	4271	172.503	-	0.003	-
MAXI J1659-152	254.757	-15.252	27044	6658	130.765	20.788	0.006	0.098
GX 1+4	263.006	-24.749	33522	8502	107.117	-	0.004	-
Ginga 1826-24	277.367	-23.789	55369	9669	102.817	-	0.008	-
1E 1740.7-294	265.977	-29.730	36511	8579	75.601	-	0.015	-

TABLE 4.1: List of the ten brightest sources identified in the mosaic pointing map of orbits 973 to 983

peakfinder was also applied to the slew images, and the six sources identified are summarised in table 4.1. Most of the sources are concentrated around the galactic centre, which was a target of many of the observations under examination. All the X-ray sources observed in this data set are well known X-ray binary systems. The low-mass X-ray binary GRS 1915 +105, isone of the most studied galactic galactic black holes. Sco X-1, one of the brightest X-ray sources known, is a low-mass X-ray binary system hosting a neutron star as a compact object. Both systems have been extensively monitored by ISGRI. Cyg X-1, Cyg X-3 and Vela X-1 are also well known low-mass X-ray binaries. Cyg X-1 and Cyg X-3 host a black hole candidate, while Vela X-1 hosts a neutron star as a compact object. These sources, although showing different levels of variability in their light curves, present persistent X-ray emission coming from the accretion disk, and thus are always visible in the X-ray band.

The differences between the two data sets are essentially two: the total exposure time of each sky pixel and whether the telescope axis is in motion or not. Due to the lower exposure, it is expected that not as many sources will be visible in the map computed with slew data. The local exposure in the slew sky map is also indicated in table 4.1. It is important to note that, even though slews and pointings are alternating in the observations, the time spent observing each source in slew mode is not simply a constant fraction of the pointing exposure, but depends on the scheduled observation and the telescope manoeuvers.

4.5.2 Point Source Location Accuracy

The last two columns of table 4.1 show the distance between the centroid of the peak and the nominal position of the source in the INTEGRAL reference catalogue. Generally speaking, the angular size of the peak is approximately equal to the projected angular size of the mask element, which for IBIS telescope is $\sim 12'$(FWHM). The point source location accuracy of ISGRI, which depends on the detector, the mask,

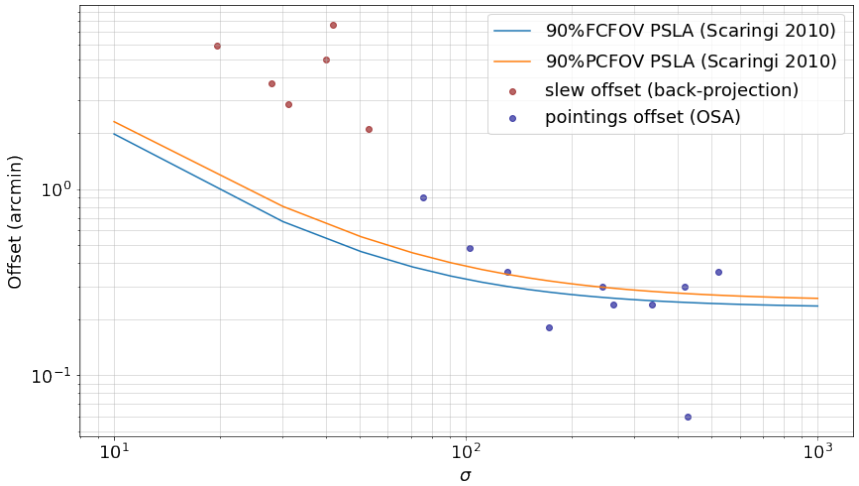

FIGURE 4.8: Offset between the the source position reconstructed by back-projection and the source position in the INTEGRAL reference catalogue. For comparison, the plot also shows the 90% confidence level PSLA from Scaringi et al (40) for the PCFOV and FCFOV

the reconstruction method and significance of detection, has been characterised during the initial phases of the mission (39). Figure 4.8 shows the offset between the reconstructed and catalogue position of the sources as a function of significance.

After both slew and pointing maps were searched for sources, the position of each source estimated from the map was compared to the known source position from the INTEGRAL catalogue. Each data point represents the offset between the known position of one source and the position estimated from the sky map. The red data points are the six sources found in the slew map, while the blue data points are the 10 sources found in the pointing map. The images of sources obtained from pointing observations have higher significance, but also show a smaller offset from the catalogue position.

For comparison, the plot also includes the 90% ISGRI source location accuracy (PSLA) from by Scaringi et al(40). While the pointing data distribute around the curve,the average offset for slew images is 0.076 degrees (4.56 arcmin), which is much greater than the offset predicted by the model used for pointing observations of the same significance. In spite of the small size of the sample, it is evident that the point source location error radius is degraded in slew observations by a few arcminutes. This effect can be associated to two contributions: the unsteadiness of the telescope during slews, and the uncertainty introduced during the linear interpolation of the pointing direction in the back-projection analysis.

It is important to point out that the peak finding tool was used on this map only for indication. In fact, the code is designed to work with OSA images, which have been cleaned from cross-correlation artefacts (ghosts). It is expected that the peak finder

will struggle identifying peaks in the slew sky map, not only because of the lower exposure (which implies a lower significance), but also because the slew map is in a raw version at this stage of development and presents a significant amount of noise. Moreover, the PSF might be larger in slew maps, due to the motion of the axis. At this stage, visual inspection of the maps is essential and further optimisation of the peak finder tool for slew maps is needed.

4.5.3 The Coding Noise

The term coding noise refers to the spurious structures in coded mask images that result solely from the decoding process. An example of coding noise are ghosts images: they are features that degrade the quality of the final image, and are not caused by statistical noise in the detector, but arise from the design of the mask and the cross-correlation process. Another example of coding noise is clearly visible in the slew sky map and is shown in detail in figures 4.9 and 4.10. Figures 4.9 and 4.10 display portions of the mosaic maps, which show of prominent line features. These lines result from decoding the gaps between detector modules as if they were active pixels. Section 3.3.1 explained how the detector average was used as a fill value for these gaps. This value initially gave good results for the test science window from the observations of the Crab, but seems insufficient to eliminate these streaks for other slew observations. This difference is probably due to the motion of the telescope axis, which contributes to either blur out or intensify these streaks: observations in a dithering pattern have the effect to blur out these line features, while slews in a single direction observations tend to show them. If, during an open slew, the telescope axis moves along one of the axis of the detector plane (y or z axis), long streaks will show along the direction of motion (figure 4.10). Since the lines in the image match the gaps between detector modules, there should also be a line orthogonal to ones visible in figure 4.10. That is not visible because it has been blurred out by the telescope motion. With the current version of the software, the presence of these structures strongly depends on the motion of the telescope axis.

4.5.4 The Sources

Some interesting remarks can be made on the sources that can be identified in the back-projection images. Figures 4.11 show the regions on the sky map around the identified sources. All of the sources present 'ghost images' at symmetrical positions around the main peak. It is important to remember that these are inevitable artefacts which are part of the instrument PSF and are due to the repeated nature of the IBIS

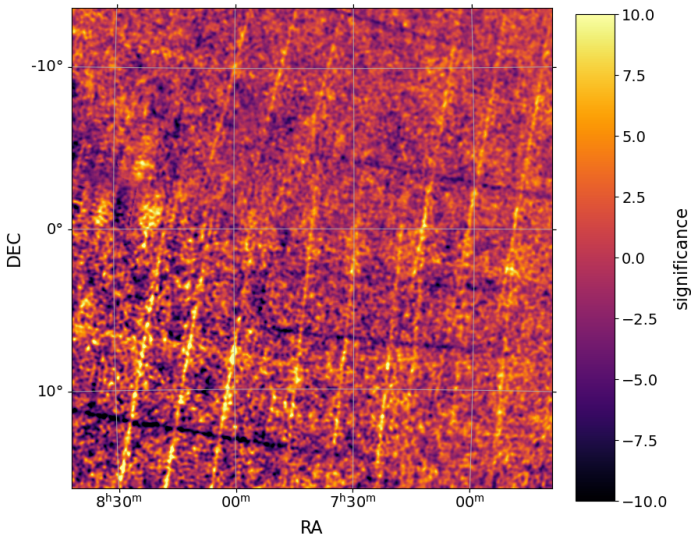

FIGURE 4.9: Coding noise due to insufficient or inaccurate correction for the dead areas of the detector plane. For a static view, the lines in the field of view match the separation of the modules in the detector plane

mask pattern. in OSA, these artefacts are removed at a later stage by means of a cleaning algorithm.

It is interesting to compare these results with the data from the pointing observations. The slew science windows sum up to a total exposure of 150 ks, which allows detection of six sources above 10 σ. If the lower number of source detections was only due to the lower exposure, the seven sources detected in the slew map would correspond to the brightest sources in the pointing map. This is true with the exception of the high mass X-ray binary 4U 1700-377, which is clearly visible in the pointing map but not detected in the slews. In order to understand why 4U 1700-377 was not detected in the slew data, it is useful to observe the back-projection image of that region of the sky.

Figure 4.12 shows the area where 4U 1700-377 was expected to be found. In spite of the presence of several bright sources, which position is indicated with white circles, the sky map does not show any peak that can be linked to 4U 1700-377. However, even though no source is visible, the background is not flat, but present structures with prominent patches and 'holes'. This effect is not completely unexpected. Generally speaking, coded masks struggle to produce good quality images when the field of view is particularly crowded, because detector is almost 'flooded' with photons from different directions. A crowded field of view, in fact, typically produces an image with a very noisy background, with prominent structures that hide the sources. In addition, each source is accompanied by eight ghosts, which overlap

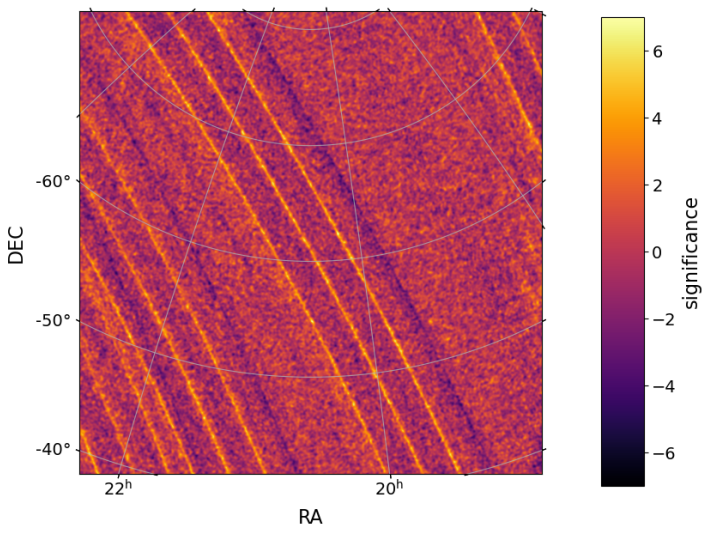

FIGURE 4.10: During long open slews, if the pointing axis is moving along the y or z direction in the telescope's frame of reference, the separation between detector modules will appear in the image as long lines along the motion direction. When the telescope operates in a dithering pattern, on the contrary, these features are less pronounced since they are blurred by the observation pattern.

and make the image even more crowded. The image cleaning and post-processing techniques implemented in OSA partially recover the quality of the image, but it is expected, at this stage, that back projection alone will not be able to reconstruct high quality images if such a crowded field of view. Even if the map showed bright irregular excesses in the same position as known sources, it is impossible to assert with confidence that they constitute a source detection, due to the low quality of the images when the field of view is really crowded. It is important to emphasize that, even with its correction method, regions in the galactic centre are affected by higher level of noise also in pointing images obtained with OSA.

4.6 Flux Calibration

The tests that were carried out on this reduced prototype data set show that it is possible to obtain back-projection images that present peaks in the position of identified sources. In order to enable the method to produce usable scientific data, it is necessary to correlate the peak in the back-projection images to the flux reconstructed by IBIS/ISGRI camera during pointings. In other words, it is necessary to calibrate the method. Figure 4.13 shows the uncalibrated flux of the six sources identified in the slew science windows of the 10 revolution data sample and the flux from the slew observations of the Crab from orbit 1461, both reconstructed using back-projection.

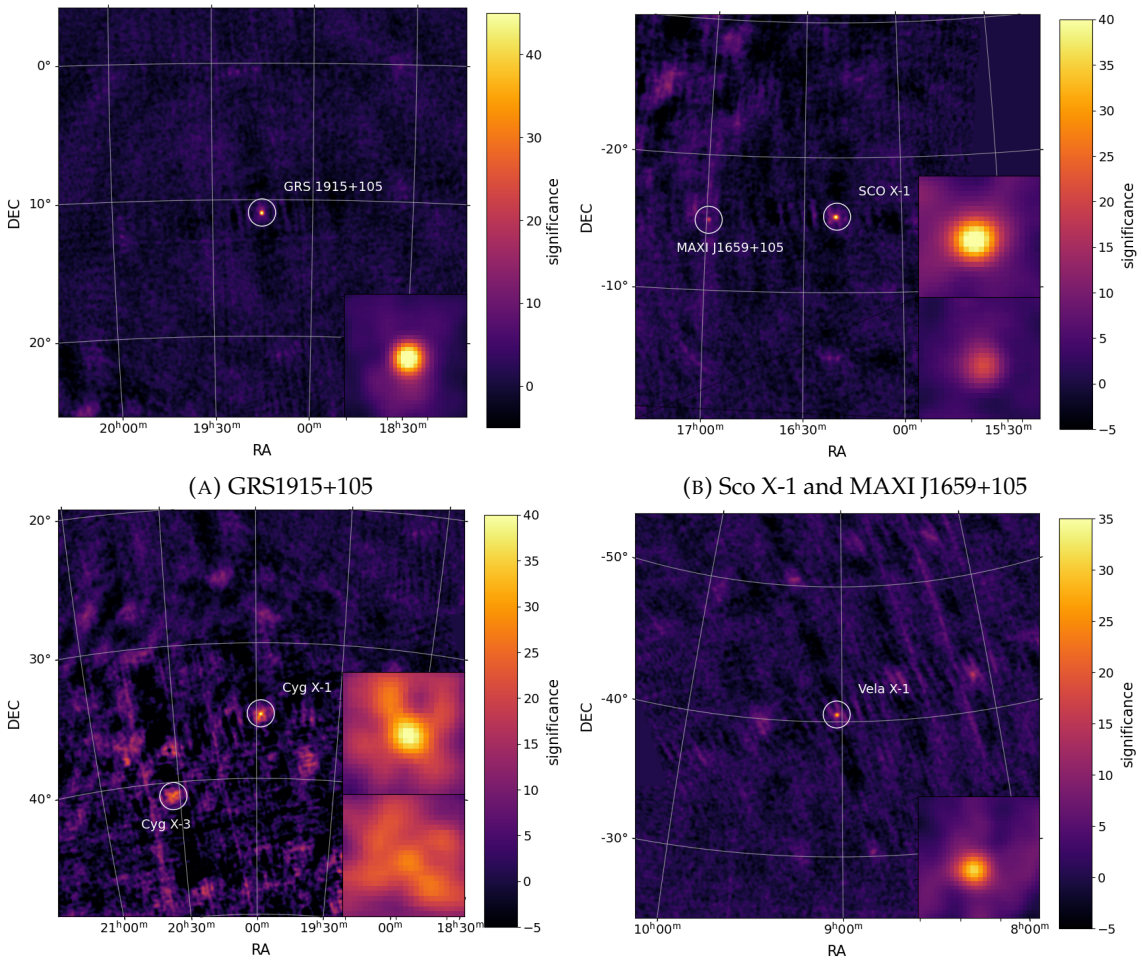

(A) GRS1915+105

(B) Sco X-1 and MAXI J1659+105

(C) Cyg X-1 and Cyg X-3

(D) Vela X-1

FIGURE 4.11: Significance maps of the regions around the seven sources identified in the slew mosaic maps of orbits 973 to 983

These fluxes are plotted against the flux calculated with OSA for the pointings of the same periods. The slew fluxes were obtained with a 2D gaussian fit of the flux maps, and the error was obtained from the variance maps. The plot also shows the values of the flux in the position of sources that were detected in the pointings but not in the slews. With the exception of 4U 1700-377, which has already been discussed in section 4.5.4, the pointing flux seems to suggest that these sources fall below the sensitivity of the method. On the other hand, the good correlation shown in the graph is an indication that the method is be able to reconstruct fluxes. However, this calibration plot has to be interpreted with one caveat: the two methods are processing data collected in different time intervals. However, since pointing and slew science windows alternate in the telescope operation, it was assumed that the potential variation of the flux was slow enough to spread across several science window and that the flux of the identified sources, averaged over the observation period, was the same in both pointings and slews.

A linear fit to the data in figure 4.13 suggests that the back-projection flux is around a factor of four lower than the pointing flux. The fit included only the sources that were detected in both operating modes. A few reasons have been identified as possible causes for the discrepancy. First, the calculation of the exposure maps in the current version of the code does not take into account vignetting effects from the mask support structure or the detector module dead time(25). On average ISGRI has a dead time around 25%, due to the combined effect of ISGRI events and the VETO strobe length. This alone will result in an underestimation of the flux in equation 4.3. Combined with the vignetting effects this contributes to lower the true exposure significantly with respect to the ONTIME. All these effects, however, are systematic or included in the telemetry, so in principle they can be modeled and corrected for. Another factor that might influence the peak heights is that the motion of the telescope axis has a blurring effect on the peaks in the image. The assumption made in section 3.3.1 that the telescope axis moves linearly with constant velocity every 8 seconds interval is not entirely accurate. In fact, the pointing axis is unstable during the slews. This effect impacts the PSF depending on how fast the axis is moving and how stable it is. An investigation of these effects on the peak values and the lateral resolution in slew images is necessary for a full calibration of the method.

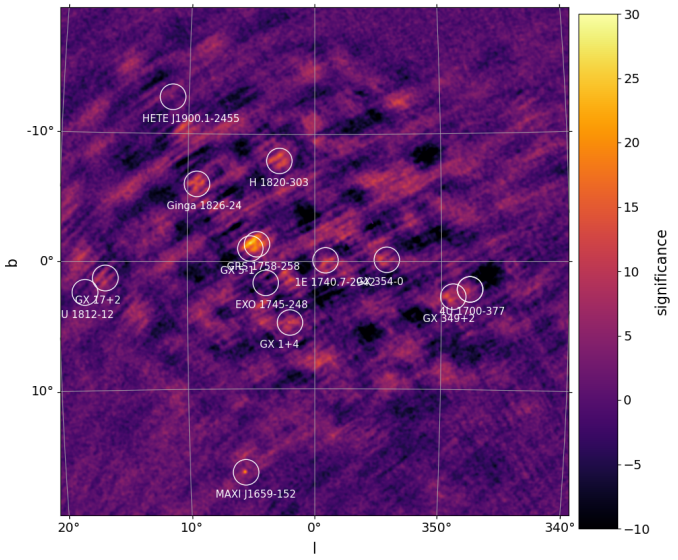

FIGURE 4.12: Slew sky map of the Galactic Centre region. When the field of view is really crowded, the image does not present a flat background, but a series of structures and 'holes'. In spite of the presence of many sources, it is impossible to recognise any obvious peak in the map and associate them to known sources

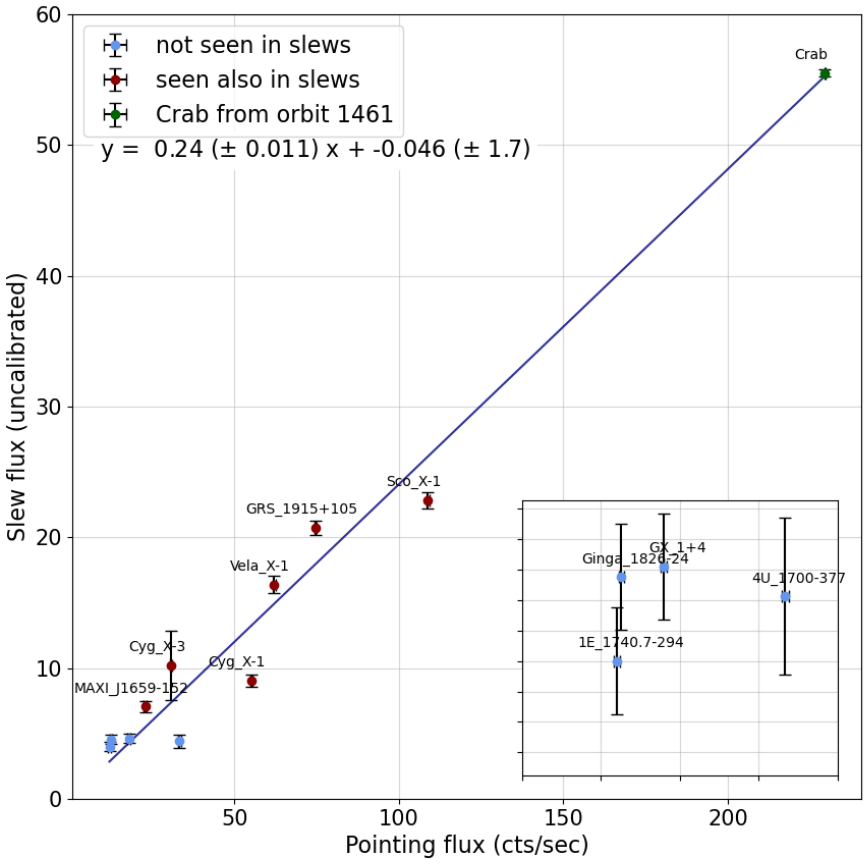

FIGURE 4.13: Back-projection uncalibrated average flux of the slews in orbits 973 to 983 plotted against the OSA reconstructed flux of the pointings in the same time period

4.7 Potential Applications

The results obtained using a prototype data set demonstrate that the IBSI/ISGRI slew data can be deconvolved using a back-projection approach, with good source reconstruction and straightforward flux calibration.

4.7.1 Search for New Sources

While using slew data for scientific purposes, it is important to note that slew observations do not have an observation target, but are simply manoeuvres performed to get from one scheduled observation to the next or from one step of a dithering pattern to the next. As a result, slew science windows can be broadly divided into

two categories. The first consists of 'quasi-static' observations, performed to move from one pointing to the next in the scope of a dithering pattern. These are called 'closed loop slews' and are generally slow and short (less than 2°). It can be assumed that the sources in the FOV of a closed loop slew are the target of the pointing observations performed immediately before or after. The second category consists of long and fast slews, called 'open loop slews' which are performed during galactic plane scans or between observations. From flight data, it can be calculated that the slew rate of closed loop slews is always at least $0.011^\circ/s$ (2° every 3 minutes). The length of slews performed during galactic plane scans are generally 7° and are performed at a higher rate, around $0.023\ ^\circ/s$. Large open loop slews can reach rates of $0.055\ ^\circ/s$(27). This would produce unacceppable blurring of the shadowgram if a standard analysis was attempted.

Consider for example a long open loop slew, with the pointing axis moving at a rate of $0.055^\circ/s$. Since the size of the PCFOV is approximately $30^\circ \times 30^\circ$, it can be estimated that a source crossing the centre of the FOV during a slew would stay in sight for 545s. Figure 4.14 shows ISGRI continuum sensitivity as reported in the latest ISGRI Observer's Manual(30). From the sensitivity characteristics of the instrument, it can be calculated that the $10^5 s$ 5σ continuum sensitivity at 40 keV is around 3.8 mCrab. This means that, assuming a continuum spectrum, the minimum source flux that can be measured with a confidence of 5σ in $10^5 s$ is 3.8 mCrab. Scaling the sensitivity down for a 545s observation, it can be estimated that the flux for a 5σ detection for a source crossing the centre of the FOV during a typical slew is around 160 mCrab.

4.7.2 Long-term Monitoring of Known Sources

The search for new sources is not the only reason for the development of an analysis method for slew data. A great portion of the sources observed by INTEGRAL are persistent X-ray sources with transient behaviours like AGNs and X-ray binaries (41). These sources are visited periodically according to the observation schedule. Slew data could provide a better time coverage of these variable sources, improving the temporal coverage of long term light-curves and increasing the amount of data to study their variability behavior in the hard X-rays. Figure 4.15 shows the slew ISGRI light curve of the high mass X-ray binary (HMXRB) Vela X-1 with data from orbit 976. The plots show the light curves from both pointing data (in red) and slew data (in blue and green). The blue data points are the light curve extracted from slew data in units of uncalibrated flux. Each data point corresponds to a single science window. Each science window image was produced in the 18-60 keV energy band, and the flux at the source position was extracted from the image. In order

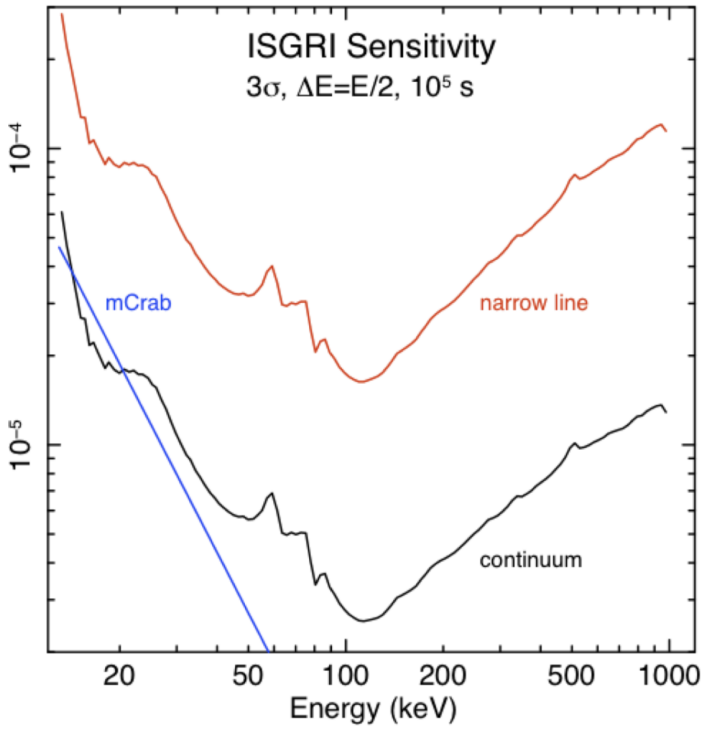

FIGURE 4.14: ISGRI continuum (black: ph $cm^{-2}s^{-1}$ keV^{-1}) and narrow line sensitivity (red: ph cm^{-2} s^{-1}) from the latest issue of IBIS Observer's manual, dated February 2021 (30)

to take into account the higher levels of systematic noise in current back-projection images, a systematic error was added to the statistical error extracted from the variance maps. The systematic error was estimated by inspecting the time variation of the measured flux at four background positions 1 degree away from the source. The level of systematic error was chosen so that the measurements in the off-source positions were always compatible with zero throughout the observation. The pointing light curve shows a significant variation in count rate, which peaks at IJD 3936.53 with a value of 202 cts s^{-1} and then falls to an average of around 60 cts s^{-1}. Due to the lower exposure time and the high level of noise of the current version of the reconstruction method, it is hard to obtain a significant flux measurement from a single slew science window when the source is in a low state. Most of the measurements between the peaks in the light-curve are compatible with zero. Where there is a peak in the pointings light-curve there is a corresponding increase in the uncalibrated flux. The slew flux has been quantitatively reconstructed with the calibration factor calculated in section 4.6 and is shown in green in figure 4.15. Despite the high level of systematic noise in back-projected images there is qualitative agreement with the pointing data around the emission peak. An image correction stage in the analysis, similar to that performed by OSA, would suppress the systematic error. Analysis of a larger data set would be needed to fully calibrate the method

and obtain more reliable flux measurements.

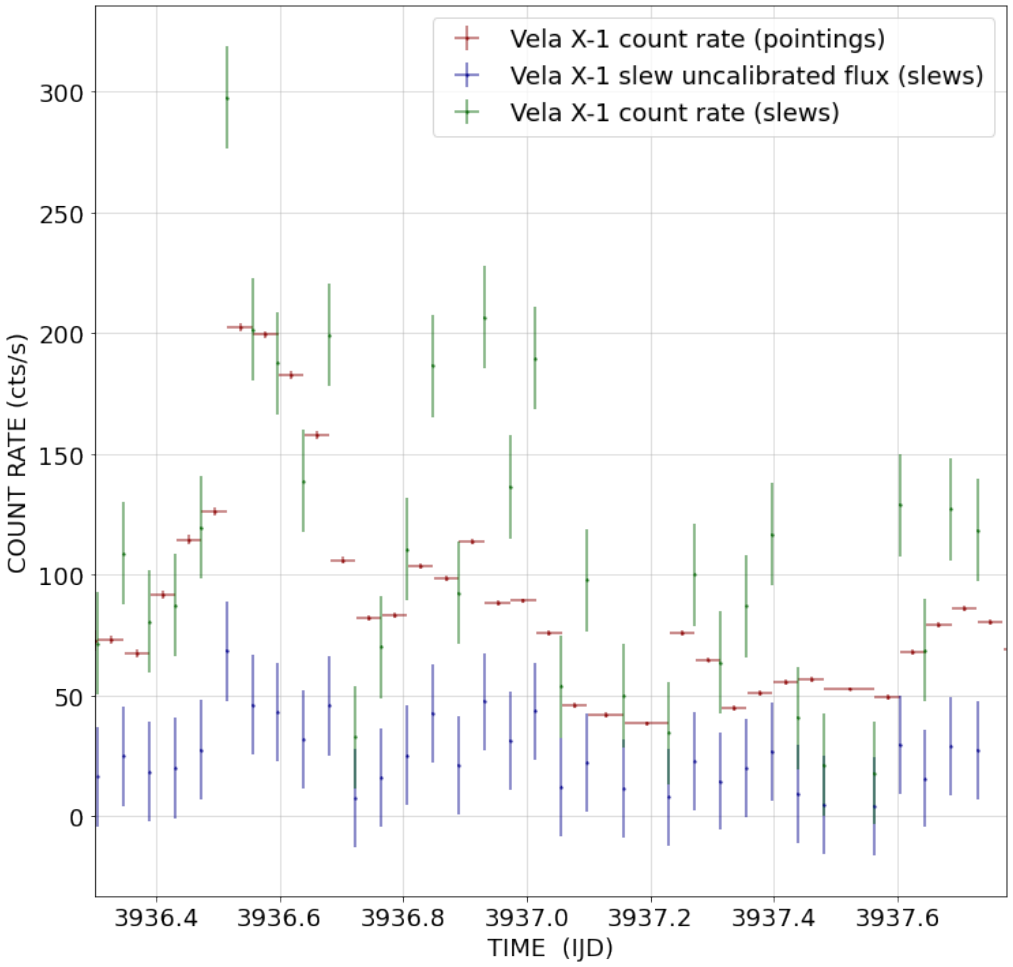

FIGURE 4.15: Light-curve of the HMXRB Vela X-1 from pointing data (red), from back-projection images (blue), and after the application of the calibration factors evaluated in 4.6

Figure 4.16 shows the light-curves of the binary system Sco X-1 obtained with the same technique. The pointings light-curve does not show prominent peaks. The count rate is stable around 150 cts s^{-1}in the first half of the observation, and falls to 80 cts s^{-1} in the second half. The data points between IJD 3939.34 and 3939.6 show a higher statistical error because they are derived from observations where the source was at the edge of the PCFOV. The statistical error on the corresponding slew data points is also higher, but the overall uncertainty is dominated by the systematic component. The qualitative but not quantitative agreement between slew and pointing light-curves confirms that the calibration procedure presented in section 4.6 needs to be improved with a larger data sample. It is important to remember that the procedure described in section 4.6 is to be intended as a validation of the method rather than a strict calibration, and the estimation of the proportionality parameters needs to be refined. It could be argued that a more accurate way to fully calibrate

the method would be applying back-projection on pointing data, and compare the count rates obtained with cross-correlation. However, this method would not take into account blurring effects due to the motion of the telescope axis, which would have to be evaluated separately.

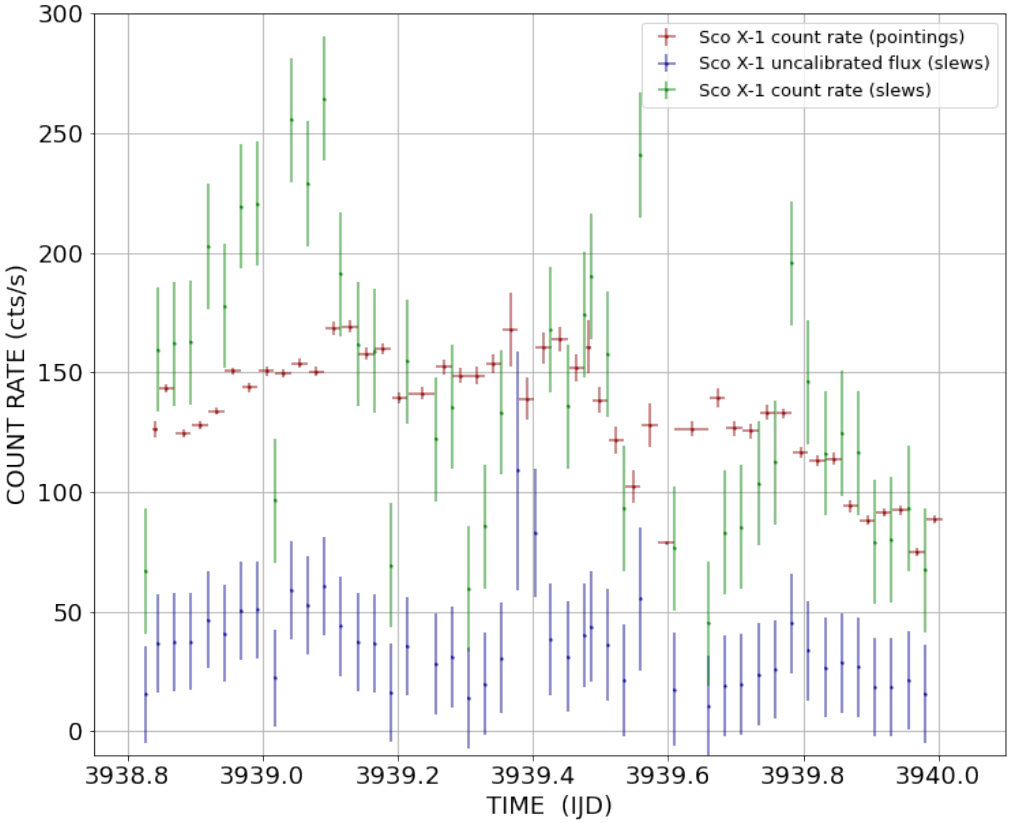

FIGURE 4.16: Light-curves of Sco X-1 from pointing data (red), derived from back-projection images (blue) and after application of the calibration parameters evaluated in section 4.6 (green)

This is an example of how slew data could be used to integrate pointing data and monitor the variability of known sources. An ideal scenario for this application would be if the telescope was slewing past a source not on the observation schedule, adding a data point to the long-term light curve of that source that would otherwise present a gap. This situation has not been found in the reduced data set presented in this work, but it is possible in a larger data set. Analysis of a larger data set will also improve the estimates for the sensitivity of the back-projection reconstruction (now empirically evaluated around 25 $\mathrm{cts}s^{-1}$) and its flux calibration for more accurate flux measurements.

4.8 Conclusions

For ISGRI, the full development of an analysis tool for slew science windows would enable the use for science of around 11% of the telescope data, which have never been analysed before. In regions of the sky that are not often visited, slew data constitute a significant fraction (up to 50%) of the total IBIS observing time. Moreover, this technique is potentially applicable to any present X- and gamma-ray mission based on coded-mask imagers to increase the observing time. The 'new' data sets available could be used for a variety of purposes, due to their intrinsic differences with the pointing data. The possibility to take data continuously could also guide the planning future missions with coded mask telescopes. Slew mode could be implemented as a fully valid observing mode for scanning and surveying purposes, instead of constituting a dead time in telescopes operation. This research project has proved that it is possible to reconstruct coded mask images of non-static observations and has lead to the development of a code that reads photon-by-photon data and produces sky maps from IBIS/ISGRI data and retrieves flux measurements from them.

Nonetheless, a number of upgrades are still necessary in order to enable this software to produce reliable scientific products that can be compared and combined with results from other existing X- and gamma-ray instruments. The first issue to address is the prominent structured noise present in the background of back-projection images which represents the main issue that needs to be addressed. A better strategy to deal with detector inactive areas need to be developed and implemented. Moreover, application of processing techniques similar to those used in OSA for image cleaning and ghost removal can significantly improve the quality of the end products of the software. Secondly, implementing a good estimate of the effective exposure, that correctly accounts for the off-axis response of the relescope is essential to produce precise count rates measurements. In fact, by not using the 'true' exposure calculated from OSA 10 onward, it is estimated that flux of off-axis sources could be underestimated by up to 50% in the PCFOV at energies around 20 keV(30).

From a software point of view, it is also necessary to consider the computational speed. Transferring the code to operate on an NVIDIA GeForce RTX 2080 GPU resulted in a speed of 90 ms to process each photon in the event list. This includes opening the event list, reading and calculating all the useful information, running the kernel and writing the output each sky map (intensity, significance, exposure). The kernel run takes just over half of this time, with about 50 ms per photon. This means that processing a single, average length slew science window with 30000 photons with a signle GPU will take around 45 minutes. During this research the

computing work was split between four computers equipped with the same model of GPU and working in parallel. This means that with the current computing capabilities, the current version of the back-projection code would process the of slew data in the INTEGRAL archive, consisting of around 9×10^9 detected photons, in just over 5 years. This might seem like an excessive length of time to access the slew data set. On one hand it is true that with the current analysis software and hardware the analysis of the slew data archive is impracticable. However, it is important to stress that this result was obtained without any particular optimization of the analysis software, apart from the parallel implementation, and with a relatively inexpensive hardware setup. Since the purchase of the graphics cards for the development of this project, new families of GPUs became available on the market, with a higher number of cores and bigger memory which are likely to reduce the computational time significantly.

A reduction on computing time needs to be obtained either by optimizing the execution of the code or increasing the computing power to be able to perform an analysis of larger data sets than the demo presented in this research. At the same time the efficiency of the algorithm could be improved by carrying out an analysis on the effect of the axis speed on the shape and amplitude of the PSF. An implementation of the algorithm could be developed where more than one photon could be processed at a time if the pointing axis of the telescope is moving slow enough between photon detections. Considering that the majority of slews are closed loop, this is probably the change that will improve the computing speed more dramatically.

Chapter 5

Coded Aperture Imaging for SPECT

The second part of this thesis focuses on the translation of the gamma-ray astronomy instrumentation and techniques presented in chapters 1 to 4 to gamma-ray emission tomography in medical imaging. This chapter starts with an introduction to single-photon emission computed tomography (SPECT) and its main applications in the medical field. Next, a review of the literature will outline the state of the art in the application of coded mask instrument to SPECT. Finally, the last section of this chapter will describe the design differences between telescopes for gamma-ray astronomy and cameras for near-field gamma-ray imaging and the additional parameters that need to be taken into consideration when designing a 3D gamma imaging system.

5.1 Nuclear Imaging

Nuclear imaging is a branch of medicine that produces images of a patient's organs and tissues using radioactive compounds administered to the patient, which emit radiation from within the patient's body. Nuclear imaging scans are normally performed in hospitals, predominantly for the diagnosis of different types of cancers. The risk associated with radiation exposure measured by a quantity called 'effective dose' and measured in Sieverts (Sv). The effective dose weights the effects of radiation exposure on all tissues and organs, and provides a number directly linked to the possible risks effects. To put the risks into perspective, in the UK, the average effective dose absorbed by members of the public only from exposure to background radiation is 2.2 mSv/year. A chest X-ray provides an average effective dose of 0.02

mSv, equivalent of three days of exposure to the background radiation. The effective dose resulting from nuclear imaging studies normally performed in hospitals typically varies between fractions of mSv and a few mSv per examination, which still leads to less than 0.1% of additional risk of fatal cancer compared to the rest of the population (42). In the cases where nuclear imaging is prescribed, the necessity of achieving a diagnosis and starting a course of therapy largely out weights the risks associated with radiation exposure. However, Every effort is always made to keep the absorbed dose as low as possible during these exams. This research project explores the possibility to apply coded masks to nuclear imaging techniques, to achieve increased sentitivity and further decrease the risks associated.

5.2 Single Photon Emission Computed Tomography

Positron emission tomography (PET) and Single-photon emission computed tomography (SPECT) are the two main nuclear imaging techniques currently used for the diagnosis of an array of different diseases. Both imaging modalities fall under the emission tomography (ET) umbrella, as opposed to transmission computed tomography (CT), where a radiation source is external to the patient and images are produced by studying the attenuation of X-rays as they travel through the body. In ET radiation emission occurs within the patient's body by means of drugs called radiopharmaceuticals, radiotracers or simply tracers. To produce tracers for both PET and SPECT, radionuclides are bound to different types of molecules that can be absorbed by the human body. PET tracers are positron emitting isotopes, SPECT tracers are generally gamma-ray emitters. In SPECT the radiotracer is usually administered to the patient orally or by means of an IV infusion. A diagram illustrating the SPECT image acquisition process is displayed in figure 5.2. After the administration of the radiotracer, the patient lies on a bed under the gamma camera. The imaging apparatus includes a detector system, normally composed of scintillation crystals coupled with photomultipliers tubes. The photons interact with and deposit energy into a scintillation crystal. The light output from the scintillator is then collected and converted into an electronic signal by an array of photomultiplier tubes. Some SPECT cameras use other types of detectors, such as direct detection in cadmium zinc telluride (CZT). A post processing apparatus interprets the detector signals produces an image of the patient's body. Each scan can last from 20 to 40 minutes, during which the patient is required to lie down still as the image is being formed. The image is then displayed on a screen and can be stored for future reference and inspections. Depending on the function that needs to be investigated different molecules are used that are absorbed and stored in different types of cells and are involved in different physiological processes. For example, orally administered ^{123}I-NaI is used

for thyroid studies, ^{99m}Tc-DTPA (diethylenetriaminepentaacetic acid) inhaled via aerosol is used for lung perfusion studies and ^{99m}Tc-MDP (methylene diphosphonate) IV infusions are used for whole-body bone studies. The gamma-rays that escape the body are then collected with an appropriate detector system and processed to obtain an image of the emission regions. Once the tracer has been administered, its radioactive component can be imaged using a properly designed gamma-camera (figure 5.1). The time between the administration of the tracer and the beginning of the data acquisition depends on the purpose of the imaging study and the nature of the tracer. The timescale of a scan depends on different factors: first of all, different types of tracers with different administration methods can take several minutes up to several hours to be taken up by the target tissues. Secondly, not only the half-life of the isotope needs to be taken into account, but also its biological half-life, which is the time required for an organism to eliminate 50% of the amount of a substance that has been administered.

One of the fields that has recently become popular in nuclear medicine is called "theragnostics" or "theranostics", and combines therapy and diagnostics with a single molecule or very similar molecules. The molecule is labeled with an alpha/beta and gamma emitter. Having a very short range inside the human body, the alpha and beta radiation transfer energy to cancerous tissues, leading to cellular damage. At the same time, the gamma radiation is used for imaging purposes, to monitor and optimise the therapy course according to the patient's response. These applications usually have a low gamma-ray yeld, and require high sensitivity systems to achieve imaging (43).

The possibility to label a wide variety of molecules allows SPECT to be a functional imaging technique, as opposed to CT scans which mainly investigates the anatomical structure of the body. ET techniques and X-ray CT are in fact often performed together and the resulting images combined to provide information about the anatomical structures surrounding the gamma-emitting region (45). The attenuation data obtained from the CT scan also helps make more quantitative ET reconstructions.

5.2.1 Collimator imaging

Most of the SPECT systems for clinical exams rely on collimators to reconstruct the emission of gamma photons. Figure 5.3 shows an example of a parallel-hole collimator, which is an array of parallel bores of uniform size surrounded by septa. The structure of collimators is usually made of highly absorbing material, such as alloys of lead or tungsten. Some types of collimators have bores that converge or diverge, in order to achieve a magnification or minimization of the image. The working principles of collimators is illustrated in the top panel figure 5.3: gamma-rays are emitted

FIGURE 5.1: An example of a Siemens SPECT camera that is currently used for different types of diagnostic studies(44). The bed slides between two detector planes equipped with collimators, which can rotate to collect multiple views of the patient. This camera is also equipped with a CT scan. In fact SPECT and CT are often carried out during the same scan

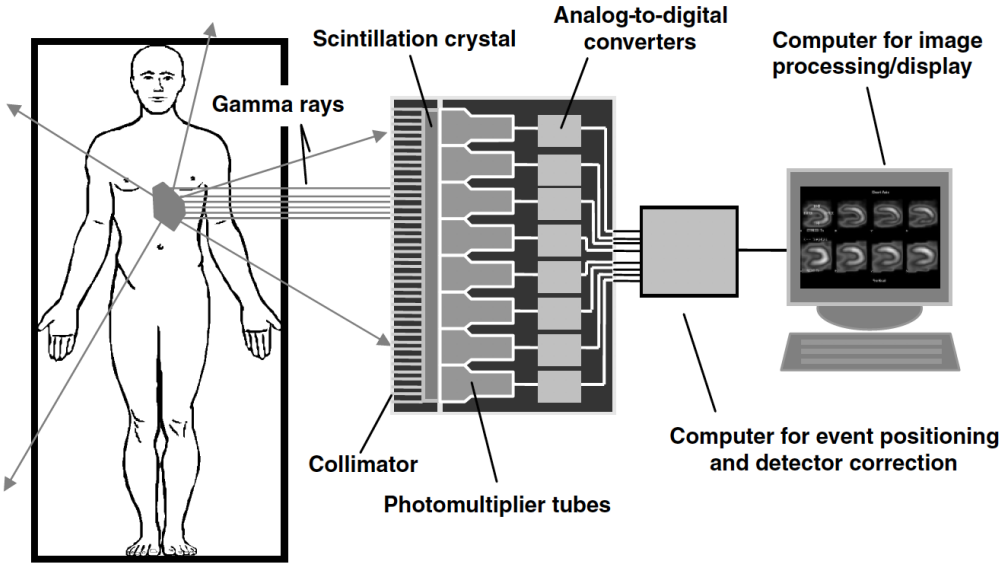

FIGURE 5.2: Diagram of a conventional gamma camera used in SPECT(45). After administration of the radiotracer, the patient is positioned on the SPECT machine bed. The radiation emitted by the radiotracer, which has been absorbed by organs, is detected with an imaging apparatus. An image is formed and can be visualised on a screen

Collimator type	Recommended Max. Energy (keV)	Efficiency	Resolution (FWHM at 10 cm)
Low-energy, high-resolution	150	1.84×10^{-4}	7.4 mm
Low-energy, general purpose	150	2.68×10^{-4}	9.1 mm
Low-energy, high-sensitivity	150	5.74×10^{-4}	13.2 mm
Medium-energy, high-sensitivity	400	1.72×10^{-4}	13.4 mm

TABLE 5.1: Performance characteristics of some commercially available parallel-hole collimators(49)

isotropically from within the patient's head. However, only gamma-rays traveling horizontally, in a direction close to the holes' axes, are able to penetrate the collimator and form a planar image on the detector, shown on the right. The size, depth and shape of the collimator holes as well as the thickness of the septa are designed to optimize the resulting image according to the sensitivity and resolution required and the energy of the radioisotopes used. The collimator sensitivity, defined as the fraction between selected and emitted gamma-rays, is strongly dependent on the collimator geometry. For a given septal thickness, efficiency can only be improved by increasing the hole diameter or reducing the collimator depth and thus negatively impacting its resolution. The geometric resolution of a collimator is defined as the radius $|r|$ such that $|r| > R_g$ implies that no ray can pass through the collimator without penetrating a septum. Figure 5.4 is a diagram of the cross section of a collimator imager. The detector plane is shown on the left. At a distance B, there is a collimator with thickness T and hole diameter D. Finally, a source is placed at a distance F from the collimator. The geometrice resolution of the collimator is expressed as:

$$R_g = \frac{D}{T} z = \frac{D}{T}(T + B + F) \approx \frac{D}{T} F. \tag{5.1}$$

Table 5.1 quotes typical values of some of the parameters that characterise commonly used collimators. The selection of the septal thickness according to the energy of the gamma-ray emission to be used is also critical for obtaining a high quality image. Septa that are too thin are transparent to high energy gamma-rays and would provide images with poor contrast. For this reason a choice of collimators with different specifications is available for clinical imaging depending on the applications. A pinhole collimator like the one showed in figure 5.5 can also be used in some instances where the volume under observation is only a few centimeters wide and close to the pinhole(46), such as thyroid (47) or small animal studies (48). In most cases the sensitivity of the collimator is between 10^{-2} and 10^{-4}. The selection of appropriate collimation determines the sensitivity and resolution of the whole SPECT image. As a general approximation high-resolution collimation (e.g. single pinhole)

often yield low sensitivity, while high-sensitivity collimations (e.g. parallel-hole) generate images with poorer resolution.

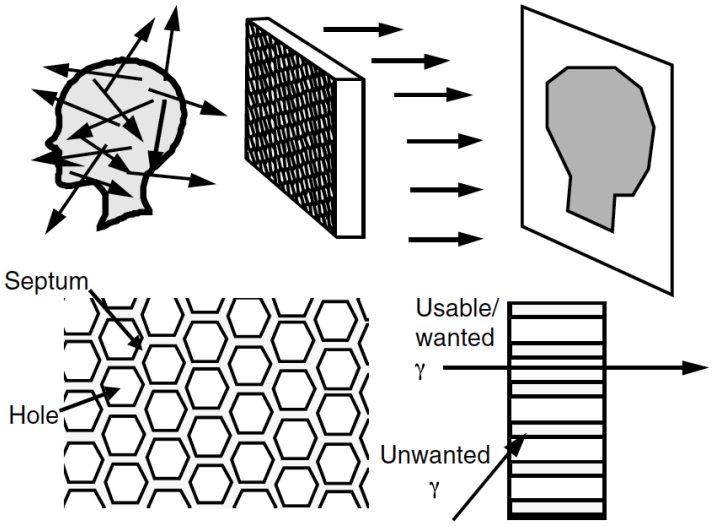

FIGURE 5.3: Top: Gamma rays are emitted in all direction from within the patient's body. A parallel hole collimator produces a planar projection of the gamma emission region. Bottom left: Example of hexagonal geometry collimator. Bottom right: Only gamma-rays traveling close enough to the hole axis are selected by the collimator(45)

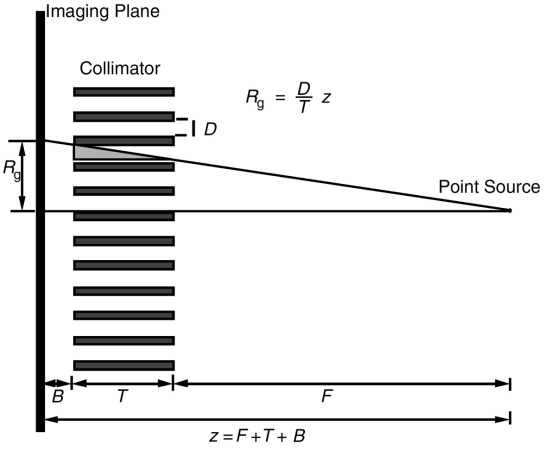

FIGURE 5.4: Estimation of the geometrical resolution of a collimator. A ray emitted by a point source enters the collimator at the edge of one hole and exits at the opposite edge. Rays with a greater inclination will hit a septum. R_g is a good estimator of the collimator resolution because all gamma-rays emitted by the point source must be detected within a radius R_g in the detector plane(45)

5.2.2 Tomographic Image Reconstruction

The image obtained from gamma-ray emission of the radiotracers can be planar or tomographic. A planar image is the 2D projection profile of the activity from a single

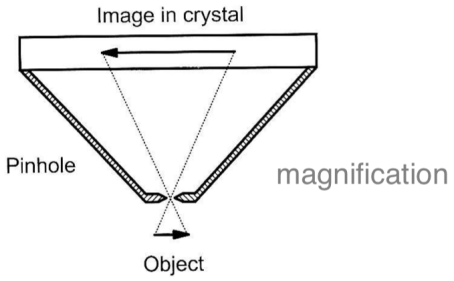

FIGURE 5.5: Diagram of a pinhole gamma camera. Single pinhole cameras have very high resolution but very low throughput. Additionaly, the FOV that can be achieved is generally small(50)

view, while a tomographic image, also called tomogram, is the cross section of a volumetric image of the radiotracer distribution. A tomography image is computed using multiple planar images acquired from different angles. Figure 5.6 illustrates the process of producing a tomographic image of a spherical object from several projection profiles. This operation is also called back-projection and includes several steps of filtering to remove unwanted blurring effects and optimise the final result to be useful for diagnostics (49). Some studies (e.g. oncology whole-body studies) rely only on planar images, while others use a number of planar images to compute tomographic images.

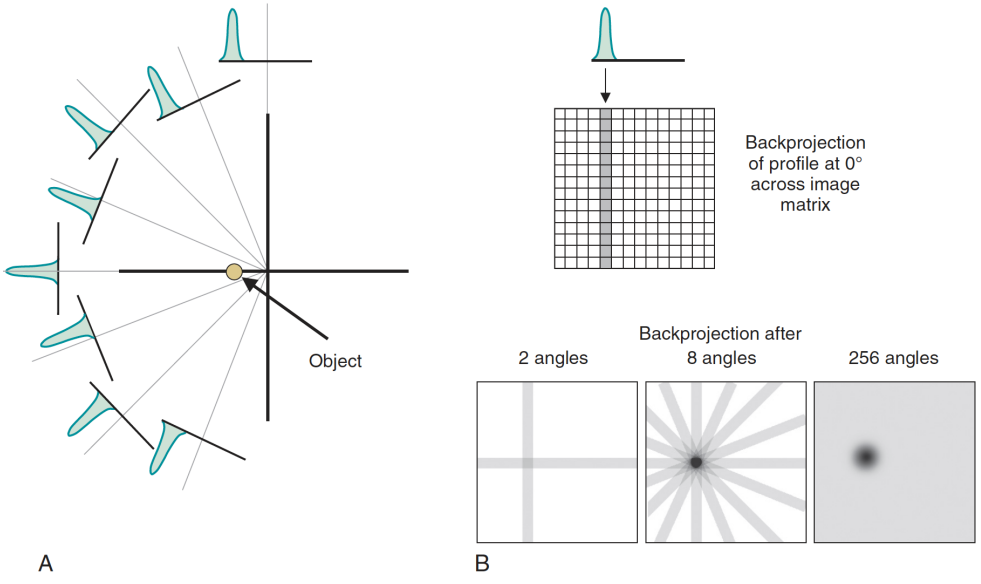

FIGURE 5.6: Illustration of the reconstruction of a 2D image of a point source from multiple planar projections. The object is observed under multiple angles (left). The projections are then combined to constrain the position of the object (49). The greater number of projections, the better the reconstruction of volumes with high activity

To achieve tomographic reconstruction, the gamma camera is rotated about the object and takes an image from usually 64 or 128 views over 360°. The greater the number of views, the more accurate the image reconstruction will be. To accomodate the mechanical components needed to rotate the collimators and detector system, most SPECT cameras have a considerable footprint, and require a dedicated room of sufficient size. The imaging system, if also equipped with a CT scan, can weight over 600 kg.

5.3 Motivation

The very low sensitivity attributed to collimators and the great success that coded apertures had in high energy astronomy suggests that coded masks could be translated to near-field imaging and overcome the sensitivity vs resolution trade off presented by collimators and pinholes. The detector flux expected on from a SPECT scan varies considerably depending on the organs under study, but is of the order of magnitude of a few cts/s cm^2. The expected background rate, generated from other parts of the patient's body, is similar. To put this numbers into perspective, the expected source flux in hard X-ray astronomy is approximately 0.2 cts/s cm^2, while the expected background rate is 0.5 cts/s cm^2. In Astronomy, coded masks have proved to perform well in a low-flux, high-background scenario, which also often occurs in SPECT imaging. In addition, the improved sensitivity and increased SNR with respect to collimators could in principle enable a more efficient use of radiation dose, with a series of benefits for the healthcare system. For example, one of the advancements that could be brought forward is the potential to safely open SPECT to a greater number of pediatric patients. In fact, since the biological tissues in children have a higher radiosensitivity compared to adults, all possible efforts are made to avoid or reduce the administration of radiation dose to the very young. Moreover, due to the size of the anatomical structures, pediatric imaging requires a high resolution, which is limited by sensitivity in current SPECT systems, but could be more easily achieved with coded masks. Coded aperture imaging could also drive the research for the production of new radiopharmaceuticals that were not detectable so far because of the low sensitivity of current systems.

The second potential advantage of coded masks with respect to collimator imagers are the intrinsic 3D capabilities of coded mask, which has been mentioned multiple times in literature, but not explored in detail. In theory, since sources placed at different distances will cast shadows with different magnifications on the detector plane, it would be possible to produce images at different depths by using differently magnified versions of the deconvolution array. This aspect is explored in detail in section 5.4. In this respect, it is worth mentioning that a few studies have been using hybrid

systems, which used both coded masks and several views around the object (51; 52). As an example, figure 5.7 shows a cross-sectional image of a micro hot rod phantom obtained in 2009 by Mu et al. with 60 angular projections and a MURA coded mask. In the medical field, a phantom is a standard object that is imaged to assess the response of a certain imaging system. For SPECT, phantoms are usually containers of different shapes and sizes filled with a water solution of the imaging isotopes to simulate the behaviour of organs and tissues after the absorption of the radiotracer. Specifically, a micro hot rod phantom is formed by a number of capillaries of different thicknesses, normally used to assess the spatial resolution of an imaging system. The system developed in this paper is able to obtain a number of high quality and high resolution images, but does not fully take advantage of the depth perception attainable with a single coded mask view.

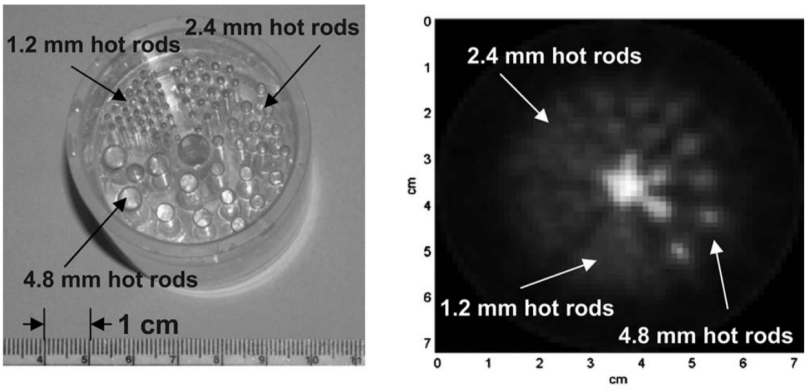

FIGURE 5.7: Experimental results of micro hot rod phantom. A total of 60 evenly distributed angular projections were acquired over a full 360° phantom rotation, each with a 2 min acquisition time. Left: picture of the phantom; right: cross-sectional image of the phantom. This image was obtained by a hybrid reconstruction method which makes use of a 3D version of the MLEM reconstruction and OSEM, an algorithm that is traditionally used to reconstruct slices from multiple views in different nuclear imaging techniques(51)

In contrast, making use of the depth perception provided by coded masks was one of the focal points of the research work presented in this thesis. A coded aperture camera was designed to obtain a $3D$ image from a single view of the target. Such a system has the potential to reduce total scan times by reducing the number of projections needed for 3D reconstruction and would be greatly advantageous in surgical environments (for example tumour excisions). Aiding surgical operations with real time 3D imaging of the surgical field is generally impracticable with current SPECT cameras that require the patient to slide through the rotating detectors.

5.3.1 Near-Field Imaging with Coded Masks

The first application of modulation techniques to near-field gamma-ray imaging was suggested by Barrett in 1972, who demonstrated the use of Fresnel zone plates for gamma-ray imaging, suggesting that this technique might obtain high detection efficiency in conjunction with high spatial resolution, which was impossible with the techniques of image formation available at the time (53). Only a couple of years later, the first multi-pinhole coded mask with a very low transmission was used to decode simulated and real thyroid phantoms by Chang et al (54) (figure 5.8). Random pinholes were placed on a lead sheet which acted as a coded mask. A very high resolution multi-wire proportional chamber was used to detect the modulated radiation, and the deconvolution was performed optically using an aluminium copy of the imaging mask.

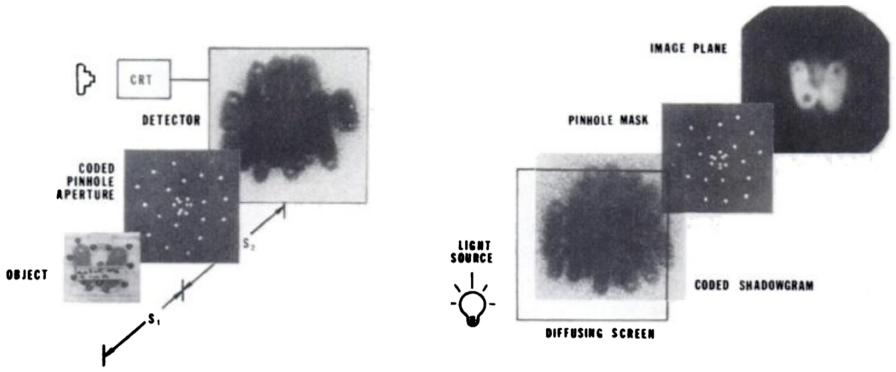

FIGURE 5.8: Left: diagram of the shadowgram formation of thyroid phantom with a coded mask made of 27 pinholes. Right: optical reconstruction of the final image(54)

These early studies already acknowledged the potential for this technique to be used for single-view 3D gamma-ray imaging, as well as its main issue: the high decoding noise associated with the presence of extended or multiple sources in the field of view. A study on a small group of patients was carried out already in 1979 (55). The thyroid was identified as an ideal target for this technique because of its small size and the high resolution needed to identify lesions. This study focused on the advantages of a translating multi-pinhole camera over a single-pinhole camera, which are lack of image distortion and the intrinsic tomographic capability of the coded aperture technique. The camera built for this study was composed of a pair of plates:

an aperture plate with a lattice of holes at a fixed distance and a code plate, containing multiple specific patterns of apertures. The code plate translated in steps in front of the aperture plate, in order to encode different images and increase the number of views of the sample. The coded aperture performed equally or better than a single pinhole camera, the main criticality being the long reconstruction time for a 3D image. Imaging of the heart was also attempted with this system, using both a ^{99m}Tc myocardial phantom and in-vivo tests, obtaining promising images (56). Once again, the authors recognised that the multiplexing of the information makes it extremely difficult to specify the sensitivity of a coded aperture imager. In fact, the signal-to-noise ratio in one point of the FOV depends on the entire source distribution, resulting in extended sources being imaged at lower sensitivity than point sources.

The application of coded masks to small animal studies for medical research has been investigated in a series of studies between 2000 and 2002 (57; 58). The small field of view and the intrinsic magnification of coded aperture imagers suits the needs for imaging small volumes with high resolution. A study carried out in 2002 included phantoms and in-vivo acquisition of tomographic gamma-ray images with coded aperture showed the improvement in resolution and sensitivity with respect to collimators(58). Figure 5.9 shows the hips and knees bone scan of a rat obtained with a coded aperture system. The details in the knees and the spine are well resolved with coded apertures, but not with the collimators. Nonetheless, the authors acknowledge that, in the case of sparse sources, the increase in sensitivity does not translate to an equal increase in SNR due to the multiplexing of the information. On the contrary, coded masks seem to outperform more conventional techniques when the activity is concentrated in a small volume, such as the body parts of a small animal. Research fields that could benefit from an improvement in imaging performance of small animal SPECT comprise radiopharmaceutical development and studying the pharmacology of new therapies.

A study carried in 2007 tried to apply coded mask imaging to breast scintigraphy. Breast scintigraphy is a gamma-ray imaging technique that detects cancerous lesions in the breast tissue. The scenario in this case is similar to point-like imaging in astronomy, which suggests that breast scintigraphy could benefit the most from the increase in sensitivity offered by coded apertures without suffering too much from the extended source coding noise. However simulations carried out in a series of publications by Analfea et al. show that the high background from the heart and torso would likely prevent the visibility of small lesions at clinically realistic activities(59).

More recent studies suggested an application of Coded Aperture techniques not for

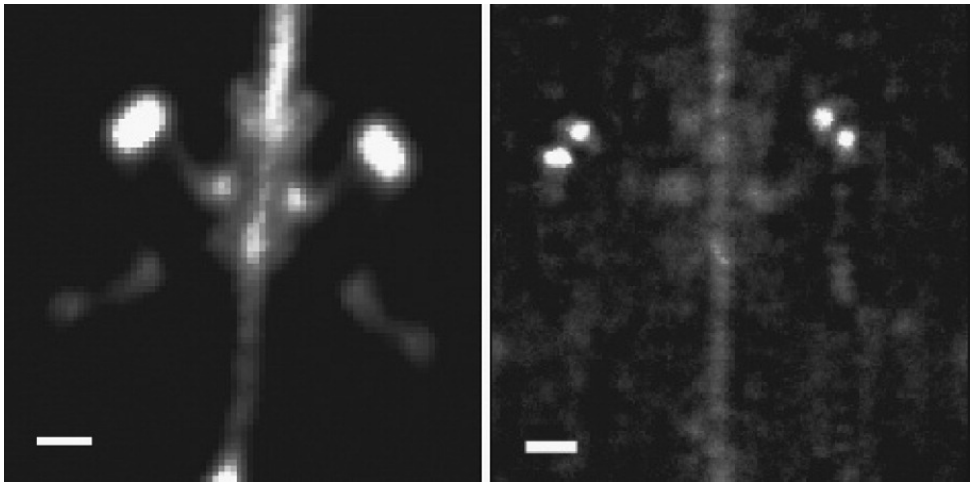

FIGURE 5.9: Bone scan of a rat. ^{99m}Tc-MDP (333 MBq) was injected intravenously, and the animal imaged at 90 min. The image shows the comparison between a 30 minutes collimator image (left, 6.2 million counts) and a 30 minutes coded aperture image (right, 62 million counts) done sequentially on the same animal. The scale bars on the bottom right corner of each image are 1 cm(58)

diagnostics, but to aide radiation therapy(60). Coded Aperture cameras with different parameters were simulated to image photons produced from Compton scatter of the the treatment beam by gold fiducial markers placed in the body. In medical imaging, a fiducial marked is an object which is placed on the body or implanted in the body of a patient to mark a target position before radiation therapy. Normally fiducial markers are small metal seed-like objects, which can be easily identified in an X-ray image. A diagram of the clinical system developed in this research is shown in figure 5.10. These image could be used to accurately track the involuntary movements of the body during radiation therapy and achieve a more effective dose delivery without administering additional radiation to the patient. The position of the fiducial markers was located with an accuracy better 3 mm.

In light of the work carried out and published on this topic over the years, it is possible to infer that an increase in sensitivity, although achievable, is highly dependent on the the tissues or disease that need to be investigated, which determine the morphology of the source under observation. In other words, the advantages that coded masks could bring about are likely to be very application specific and building a system that works for a broad spectrum of studies is unlikely. An extensive theoretical study of the potential for coded masks to be applied to medical and near-field gamma imaging in general was carried out by Accorsi(61). Accorsi's dissertation focused on building a strong theoretical formulation on the SNR and artifact formation in coded aperture imaging and a extensive verification based on Monte Carlo simulations. Papers published in this research were often consulted and referred to in the design part this thesis work.

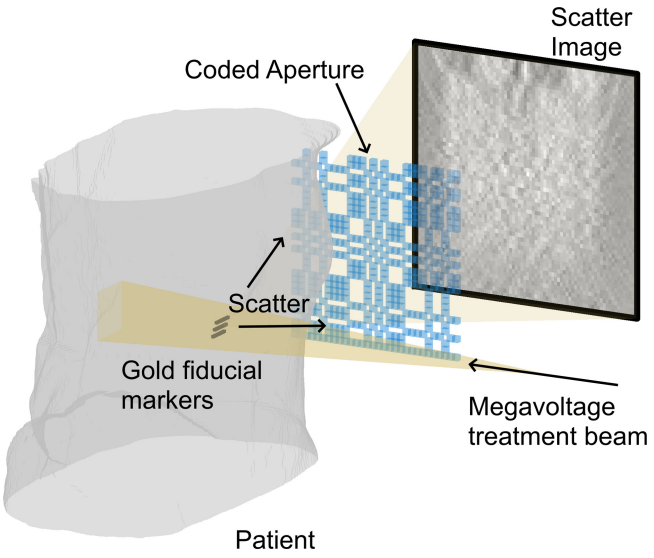

FIGURE 5.10: Mock clinical setup of the 2020 study from Mahl et al. The high-energy treatment beam enters the patient, scattering off of the fiducials and tissue. The coded aperture is placed between the patient and the imager which is orthogonal to the treatment beam direction. Radiation which is scattered through the coded aperture is recorded by the detector and decoded to produce a real-time image of the fiducials' location and motion(60)

5.4 Three-Dimensional Imaging with Coded Apertures

The most relevant parameters in the design of a coded aperture imaging system and their effect on the image quality in a near field three-dimensional scenario are described in this section. All these effects were taken into consideration in the design phase of this research, which lead to the production of a prototype camera which will be described in chapter 7.

5.4.1 Field of View

When reconstructing astronomical images, it is assumed that all the sources in the sky are located at the same distance (infinity) and therefore the field of view is expressed as the angle observed by a telescope. When the method is translated into near-field gamma-ray imaging, though, one dimension needs to be added to the observed space. The shape of the FOV in the 3D space is a truncated pyramid, as shown in figure 5.11. The depth of the FOV (z) is determined by different factors and effects. A source that is placed too close to the coded mask will project a very magnified shadow on the detector, to a point where the finite dimension of the detector is not large enough to sample a significant portion of the mask and produce a good quality image. The upper limit for the FOV depth is posed by the inverse

square law of radiation propagation, which limits the number of counts that can be obtained from sources that are far away from the detector plane.

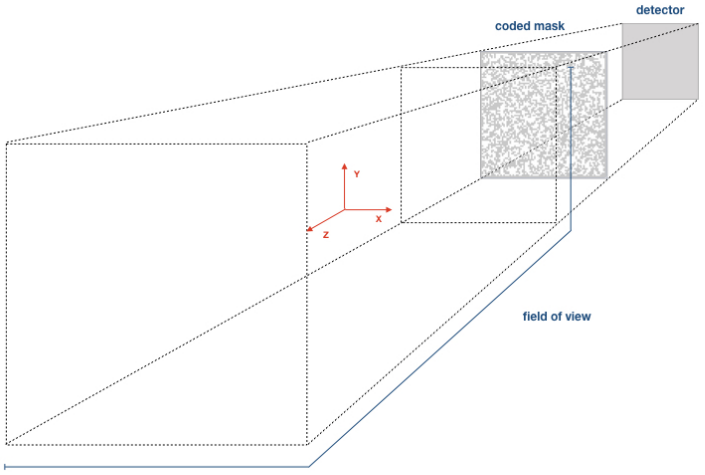

FIGURE 5.11: Diagram of shape of the 3D FOV of a coded aperture system with a square detector and coded mask. In this case the detector is smaller than the camera plane, in order to obtain a wide FOV. The FOV gets larger at greater distances from the mask

If the detector-mask distance is kept constant, the shape of the FOV depends on the relative size of the coded mask and the detector plane. The details of each configuration have been discussed in chapter 1. Equations 1.2 and 1.3 show that the size of the fully coded field of view increases as the mask size increases. Conversely, an increase in the detector size causes a decrease in the size of field of view. This does not necessarily mean that smaller detectors can be used to achieve large fields of view with a good image quality. In fact a small sensitive area affects the photon collection capability of the instrument and has a negative effect on the image SNR, due to the fact that only a fraction of the mask pattern can be projected on a smaller detector. The graph in figure 5.12 shows how the mask to detector distance affects the size of the FOV at a fixed distance from the coded mask.

5.4.2 Lateral Resolution

The resolution of a camera is an essential parameter to describe the quality of the images it produces. According to the Rayleigh criterion, widely used to define the

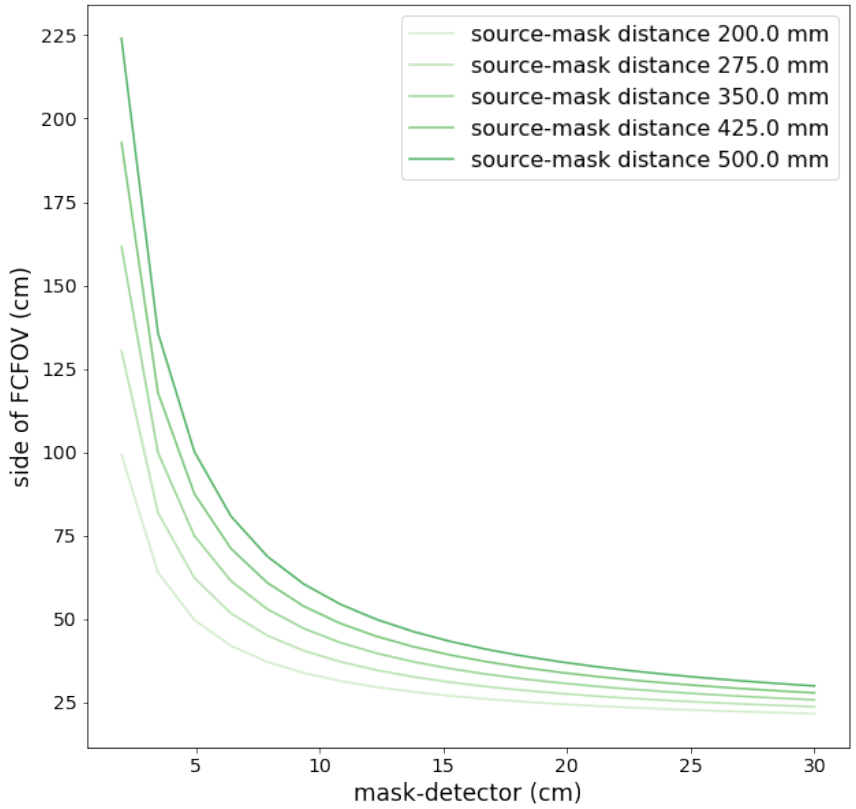

FIGURE 5.12: Length of the side of the FCFOV as a function of the detector-mask distance. The parameters used are: detector size 76.8 mm$\times$ 76.8 mm, mask size: 176$\times$176 mm^2. These parameters are the parameters of the prototype that was built during this research project

resolution of any imaging system, two sources are resolved if their distance is greater than one FWHM of the PSF apart. For coded aperture cameras, this condition is met when the angular distance between two sources is so that their projections on the detector plane do not overlap. This is illustrated in figure 5.13. Two sources placed at an angular distance λ_g produce two distinct projections of the same mask pixel on the detector plane. The distance between the centres of the projections is mp_m, where m is the magnification of the mask pixel projection, expressed in equation 5.4.

In the near-field scenario, the angular resolution of a coded mask system is

$$\lambda_g = \arctan \frac{OM + MD}{MD} p_m \tag{5.2}$$

As a result, the lateral resolution r at an object to mask distance OM is

$$r = (MD + OM) \tan \lambda_g \tag{5.3}$$

Equation 5.3 shows that the lateral resolution of a coded mask imager increases as the object distance from the camera increases. This effect is displayed in the plots in figure 5.14(a). A full derivation of equation 5.2 from the definition of angular resolution according to Rayleigh criterion can be found in Accorsi's dissertation (61)

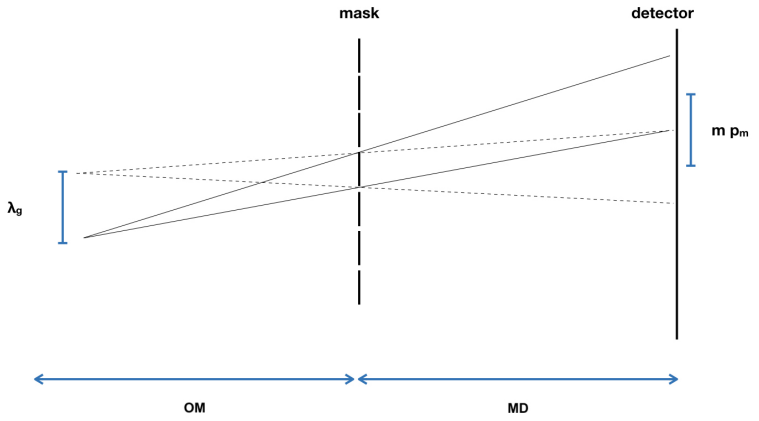

FIGURE 5.13: Calculation of the angular resolution of a coded aperture imager from Accorsi (61). λ_g is the minimum distance for which two sources are more than one FWHM of the PSF apart in the final image . The magnification of the shadow of a mask pixel projected onto the detector is m

It might be tempting to conclude that reducing the object to mask distance is the best way to improve the lateral resolution, but doing so will only work within certain limits. An excessive increase in the magnification factor would degrade the quality of the image, because a detector of finite size would only be able to capture a very small portion of the mask pattern. The specific value of the minimum object distance that a camera can optimally image also depends on the mask pattern chosen and needs to be assessed on a case-by-case basis. Figure 5.14(b) shows the degradation of the lateral resolution as the mask to detector distance MD decreases. In addition to the lateral resolution, the photon collection efficiency is also negatively affected by an increase in MD due to the inverse square law of flux propagation. The most effective way to improve the resolution of a coded aperture camera is actually reducing the size of the mask pixel as much as possible. In practice this can only be done within certain limits, posed by the self collimation effects introduced by the non zero thickness of the mask (see section 5.5.2) and not less significantly the precision achievable by the manufacturer of the mask. All these effects have been taken into account in the the design of the camera.

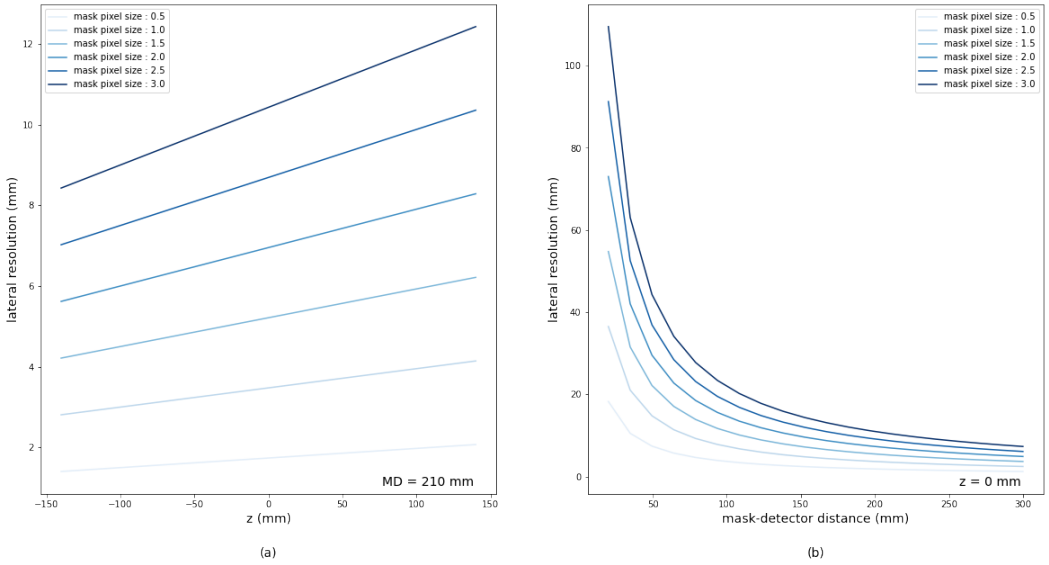

FIGURE 5.14: (a) Linear variation of lateral resolution along the z axis of the camera. The origin of the z axis of the system developed in this research is placed at 310 mm from the coded mask. (b) Dependence of the lateral resolution on the mask-detector distance MD. The lateral resolution of a coded mask image improves rapidly with increasing MD. However an increase in MD implies a greater distance between the source and the detector and consequently a decrease in detector flux

It is also important to note that these considerations are valid for an ideal detector with infinite resolution. The effective resolution of a coded mask camera is influenced by other physical factors such as the detector type and pixelization and the material and thickness of the mask (61).

5.4.3 Three-Dimensional Imaging and Depth Resolution

Based on purely geometric considerations it is possible to derive that the shadow of a mask pixel projected onto the detector plane will be magnified by a factor m:

$$m = \frac{OM + MD}{OM} \tag{5.4}$$

where OM is the source to mask distance and MD is the mask to detector distance. This magnification effect provides coded mask cameras with the ability to discriminate the distances of radiation sources from the mask with a single view.

The distance information, in fact, can be reconstructed by deconvolving the shadowgram using a properly magnified decoding array. The use of a certain value of the magnification factor corresponds to the reconstruction at a particular distance. In other words, a decoding array with the same magnification as the shadowgram

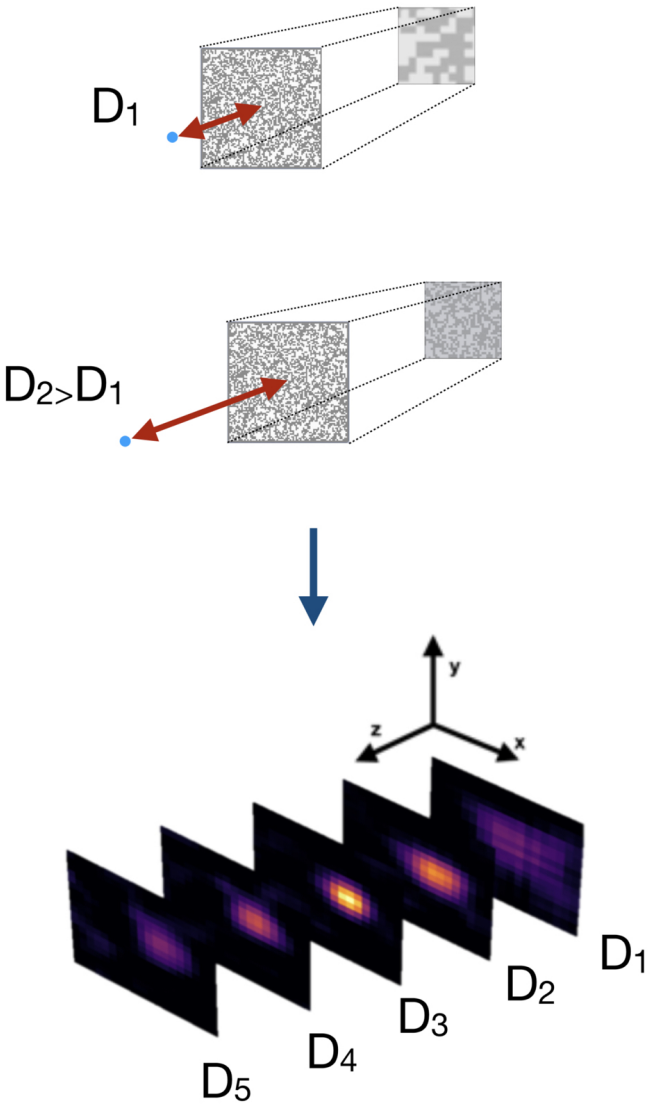

FIGURE 5.15: At the top, two sources at two different distances from the coded mask, cast two different shadows on the detector planes with different values of magnification. At the bottom, a 3D image of a single source reconstructed using deconvolution with magnified decoding array corresponding to planes at different distances D_1 to D_5

will produce an image of the source. Conversely, a decoding array with a different value of magnification will produce an image of pure (coding) noise. Therefore, a three-dimensional image can be reconstructed using an array of differently magnified decoding arrays, each corresponding to a particular plane along the camera axis, as represented in the diagram in figure 5.15. Experiments and simulations in literature(61) and during the course of this research project have proven that the depth resolution of a coded mask camera is about one order of magnitude worse than its lateral resolution, although the specific value can vary depending on camera design, position in the field of view and reconstruction method. Since the intrinsic depth perception of coded mask cameras is not sufficient to achieve a sub-cm resolution, a second camera was added to the system designed in this project, observing simultaneously at a 90 degrees angle from the first camera. This configuration will acquire two views of the the target at the same time, obtaining desired resolution without the need for a rotating gantry and with a significantly less large and heavy piece of equipment. It is important to point out that since the scale of the projected pattern varies greatly within the FOV, particular attention should be paid to the choice of the detector and its pixel size to ensure that, at each level of magnification, the mask pattern is sampled appropriately. Literature agrees that a sampling ratio $\geq$2 is sufficient to appropriately reconstruct a coded mask image (57).

5.5 Mask Designs for Near Field Imaging

The pattern chosen to manufacture the mask is a random pattern with some modifications, applied to make it self-supporting. This choice was led by the characteristics of the image to obtain.

5.5.1 Mask Patterns for Near Field Imaging

The main advantage of using a MURA pattern for 2D imaging is that if the coded mask imager is designed so that an integer number of repeats of the basic pattern is projected onto the detector, the sidelobes of the SACF are flat and can be balanced to obtain a zero background. These optimal properties, which made MURAs so popular for astronomy and far-field imaging, do not transfer to near-field 3D imaging, since the magnification of the mask pattern in the shadowgram varies with the source distance and the portion of the mask which is mapped on the detector does not always correspond to a full basic pattern. In the early stages of this project different detectors were considered to equip the prototype system and analyses were carried out to identify the best configurations. One of these detector units was a Direct Conversion cadmium telluride module with 1536×1944 pixel of $0.75\mu m$ side.

The rectangular shape of the detector showed some interesting properties in the imaging capabilities in simulations, which relate to the choice of the mask between MURA and random patterns. A coded mask camera was simulated, with the Direct Conversion detector and two versions of a square coded mask: a 61×61 random pattern and a mask formed by 4 repeats of a rank 31 MURA basic pattern after subtraction of a row and a column. The mask-detector distance is 100 mm and the mask pixel size is 2.5 mm

Five hundred source positions were selected randomly in each plane along the z axis of the camera between 50 and 300 mm from the mask. For each position the subsection of the mask projected on the detector plane was calculated. The SACF of this subsection is an indicator of the point source reconstruction capabilities of the system for that position in space. In particular, figure 5.16 shows the SNR, calculated as the amplitude of the signal in the SACF divided by the noise. The noise, calculated by the standard deviation of the SACF after removing the peak, varies with $\sqrt{n}$, where n is the number of active mask pixels. To compare the SACF SNR at different distances, it was normalised to a mask with 1000 pixels. The plot shows the average and the spread of the SNR values. The MURA performs really well for sources at 110 mm and 220 mm from the mask. At these distances, in fact, the size of a full basic pattern matches the size of one of the sides of the detector plane. At all other distances the SNR is lower and strongly dependent on which portion of the mask is used. The behaviour of a random pattern, shown in blue, is not dependent on distance, and the SNR, although on average lower than the MURA's, has a similar performance for sources along the camera axes. Moreover, the random mask shows smaller dispersion within each distance plane. Thus, the uniform response of the random mask was picked for the final design.

5.5.2 Auto Collimation of the Mask

The size of the mask pixel and mask thickness also pose a physical limit on the quality of the reconstructed image. An ideal mask is infinitely thin and blocks 100% of the incoming radiation. In practice, in order to obtain sufficient opacity to gamma-rays, coded apertures need to be manufactured from a sheet of tungsten or lead that is generally at least 5 mm thick. The thickness of the mask introduces a collimation effect on the incoming radiation, as illustrated in the diagram in figure 5.17. A really thick mask is very effective in blocking incoming radiation and reducing the background level in the shadowgram, but also causes a higher level of absorption of gamma rays from off-axis directions and a consequent decay in the instrumental response towards the edge of the FOV.

The effect of self-collimation on a coded mask camera was estimated by means of simple geometrical considerations. A test volume of cubic shape within the FOV and a test point source were considered. Figure 5.18 shows a 2D cross section of the system and the FOV. The detector plane is on the right, the mask is represented in the middle. The imaging volume is represented by the area at the right of the mask. The imaging volume was divided in voxels, and a test point source was placed in one of them. A line of sight or line of response was traced from the centre of each detector pixel to the centre of each mask pixel. Each of the lines was considered a valid line of response (LOR) if it intercepted the voxel containing the test point source. In addition to this, the effective mask pixel size was determined by calculating the angle between the corresponding LOR and the mask plane, which reduces the open surface of the mask pixel if the detector pixel is off-axis. The test point was moved along the x axis of the system and for each position the total number of valid LORs was counted. The number of valid LORs for each test source position was considered as an estimator for the efficiency of the mask compared to an ideal, infinitely thin and perfectly opaque mask. Figure 5.19 shows the result of this simulation. As the test voxel is moved laterally across the FOV, the number of LORs penetrating the mask falls due to the increasingly oblique angles. The 0.5 mm thick mask is a good representation of an ideal scenario. The response of the camera is relatively flat up to approximately 110 mm from the axis, which is the size of the FCFOV. Then the response falls to zero at the edge of the PCFOV, represented with a red dashed line, at 260 mm from the camera axis. The 5 mm thick mask shows a response that

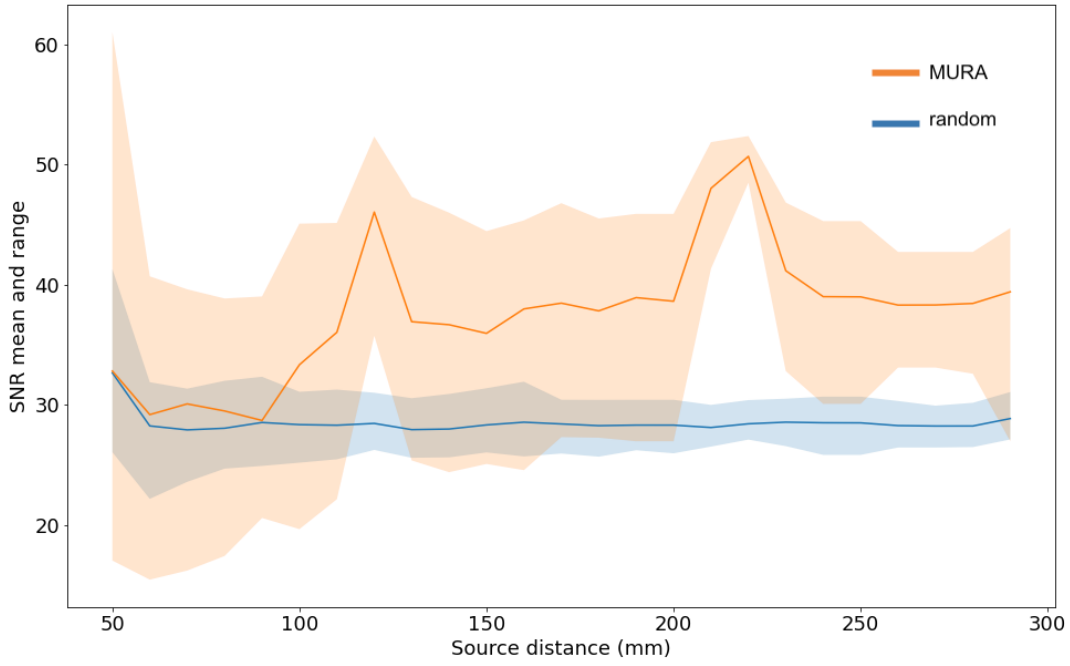

FIGURE 5.16: normalised SNR of the SACF for a random mask and a MURA for various distances between the source and the coded mask

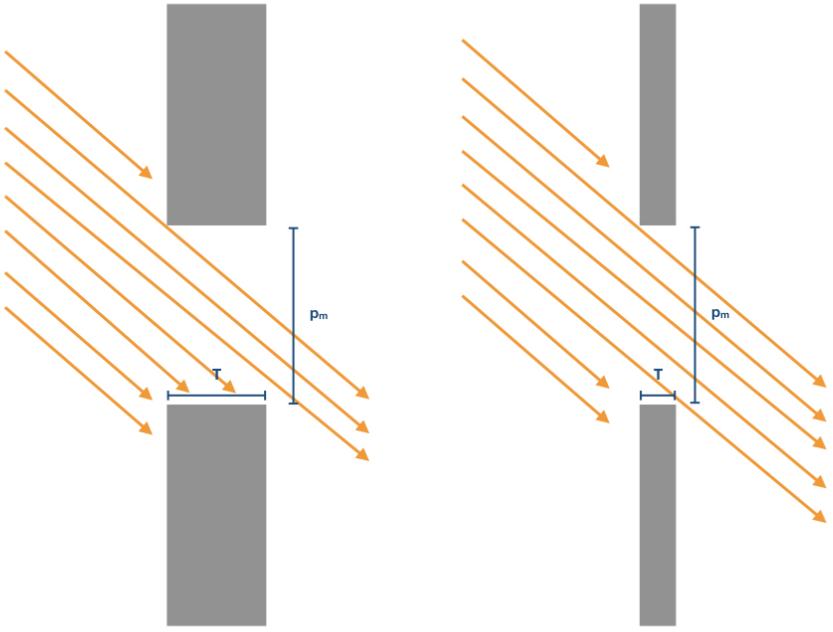

FIGURE 5.17: Effect of the mask pixel aspect ratio on the transmission of off-axis gamma rays. Neglecting the non zero transmission of the mask material, a thicker mask blocks a higher fraction of the incoming radiation at greater angles from the camera axis

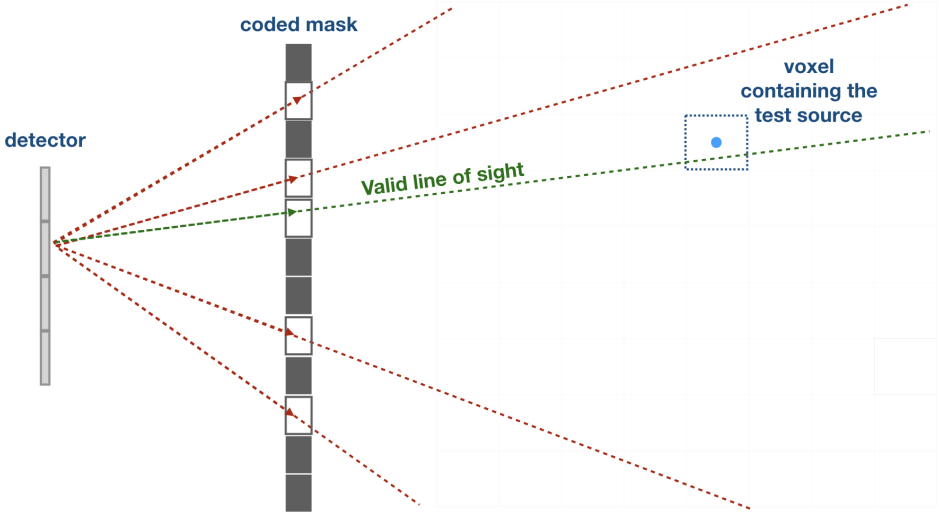

FIGURE 5.18: Geometrical calculation of the off-axis image degradation due to the collimation effect of a thick mask. The coded mask camera is represented on the right of the diagram, while the imaging volume, divided in voxels, is represented on the right. A test point source, represented in the diagram, was placed in one of the voxels. For each detector pixel-volume voxel pair, a line of sight is considered valid if it connects the detector pixel and the voxel containing the test source through an opening in the mask

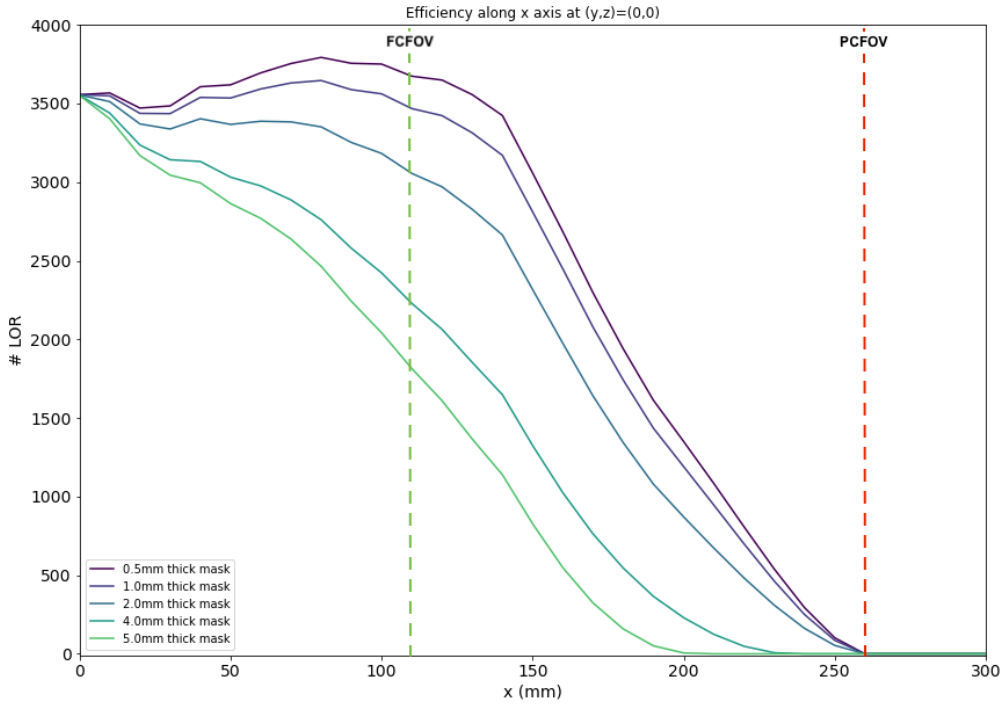

FIGURE 5.19: Effect of mask self-collimation on FOV size. The vertical axis of the plot represents the number of valid lines of response as the test sources is moved along the x axis of theh system towards the edges of the FOV. The thicker the mask, the faster the camera response falls towards the edges of the FOV

falls almost immediately as the test source is moved away from the camera axis. The modulations of the plateau in the central region of the imaging volume, at x between 0 and 110 mm, depend on the specific mask pattern used. Although this analysis is purely geometrical and represents a relatively crude estimate, the effects of mask self-collimation are clearly shown even in an ideal scenario where the gamma-ray transmission of the material of the mask is not taken into consideration.

5.6 Conclusions

This chapter has introduced the techniques and purposes of SPECT imaging and described the considerations that must be made when designing an extension of coded apertures to 3D imaging. In particular, the shape of the FOV and the definition of resolution for a 3D coded aperture system were discussed. Moreover, the challenges expected when using coded masks to image three-dimensional sources in a near-field scenario have been identified: first, the imaging capabilities depend somehow on the morphology of the object observed. Second, the poor resolution along the camera axis is an obstacle tho the construction of a high quality image with a single view of the target. Lastly, performing a cross-correlation reconstruction at multiple

distances/magnifications is unlikely to be efficient. The next chapters outline how the back-projection method described in chapter 3 was extended to a 3D setting, and the steps taken to address these challenges.

Chapter 6

Algorithms for Image Reconstruction and Optimization

This chapter describes the algorithms used to process the imaging data from the coded mask system. First, a 3D version of a back-projection algorithm that is derived from the IBIS/ISGRI slew-survey software was used. The back-projection software traces each detected photon back to all the regions of the 3D space where gamma emission could have taken place. The projection of detected photons to different planes in order to obtain a 3D image is even more computationally intense than the 2-D astronomical case. In order to speed up the reconstruction process from a computational point of view, 3D projections are pre-calculated and stored in memory to be accessed by the code. The shape and values of these projections depends on the geometry of the imaging system. This chapter first describes the these projections and how they are used to reconstruct 3D images. The second section introduces and explains a post-processing algorithm called CLEAN, which has been used to improve the SNR of coded mask images.

6.1 3D Back-Projection

The 3D back-projection software is an expansion of the code described in chapter 3. The reason behind the application of a photon-by-photon approach to this type of imaging is the idea that this imaging technique could enable the development of lightweight and possibly hand held real-time gamma imagers. These imagers could be used in dynamic studies, where the camera or the target of the observation is moving. Due to the equivalence between back-projection and cross-correlation, the imaging performances obtained in the experiments presented in this thesis are equivalent to those obtained with cross correlation images.

6.1.1 Single Pixel Projections

Single pixel projections (SPP) projections are 3D matrices that represent the visibility of the field of view by each detector pixel. Similarly to the projections used in the slew analysis software, each SPP represent the parts of the 3D FOV that can be seen by a specific detector pixel given a specific mask pattern and system geometry. For the SPECT camera developed in this research, the volume of space represented in the final image is a cube of 280mm $\times$ 280mm $\times$ 280mm. The centre of the imaging volume is placed 520mm from the detector plane. Considering that the nominal resolution of the SPECT camera varies between 7mm and and 12mm, the target resolution for the prototype system is around 5mm. Consequently the size of the voxels was set at 2mmx2mmx10mm in order to oversample the PSF which has an elongated shape. As a result, each SPP is a $140\times140\times28$ matrix. It is important to note that due to the shape of the FOV for coded mask instruments, approximately half of the voxels in the volume represented by the SPP are outside of the FOV and are assigned a value 0. There is a distinction between the camera's FOV, which was described in chapter 5 and the region of space described by the SPP, which is a 3D cube and includes part of the truncated pyramid shape that makes the FOV, but also the space around it. The construction of the SPP for 3D imaging follows the same steps as the construction of the SPP for the slew data analysis software. The only difference from its 2D version is that the reconstruction is repeated for a 28 planes at different distances from the coded mask.

6.1.2 3D Image Reconstruction

In order to prove the equivalence between back-projection and cross-correlation also in the 3D case, it is useful to keep z fixed and consider the reconstruction in a single plane at a certain distance z. The deconvolution formula using cross-correlation is:

$$I(i,j) = \sum_{l,m} G_{i+l,j+m} \cdot C_{l,m} \tag{6.1}$$

The indexes i and j represent the shift of the deconvolution array in units of the shadowgram pixels before its components are multiplied by the elements of the shadowgram C.

Figure 6.2 represents the cross section of $SPP^{l,m}$ at a certain value of z or, equivalently, the back projection of a single photon at a distance z The distance between the coded mask and the plane in figure 6.2 will be referred to as MZ. From the figure it is clear that the shift of the projected mask pattern with respect to the camera axis is equal to the distance of the detector pixel l, m from the centre of the detector plane,

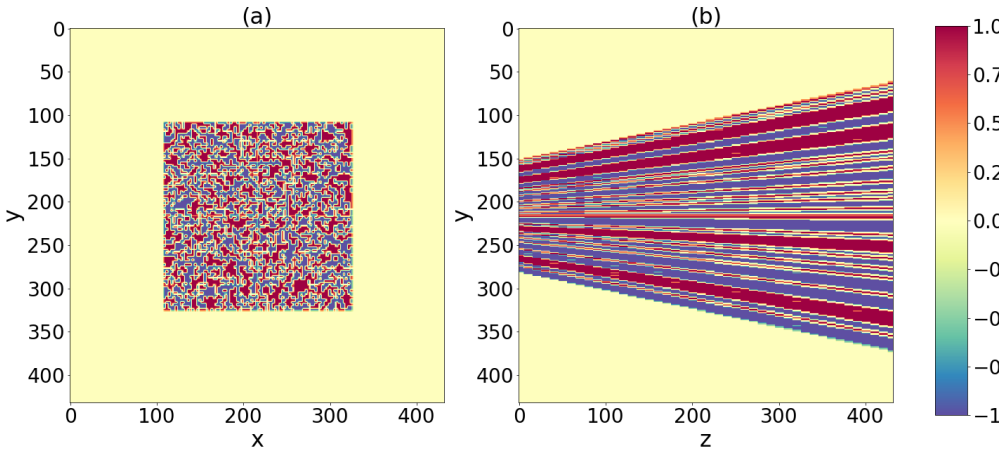

(A) x-y plane (left) and z-y plane (right) and cross section of the SPP for the central detector pixel 23-23. Notice how the FOV becomes larger with larger z

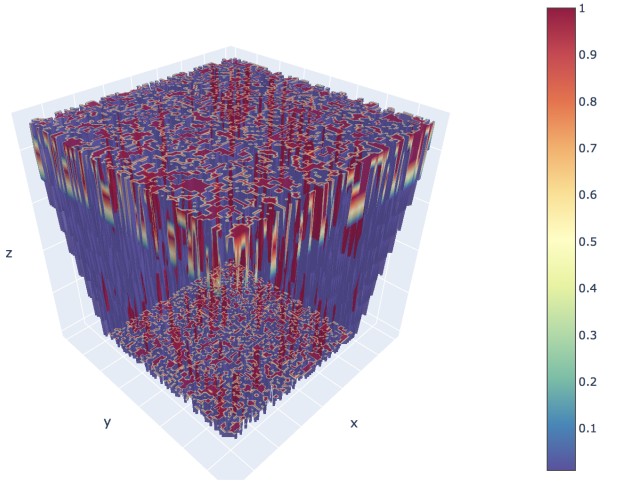

(B) Three-dimensional representation of the SPP for detector pixel 23-23. This 3D version of the SPP, computed to reconstruct images of a 3D field of view, have the same truncated pyramid shape as the FOV itself

FIGURE 6.1

multiplied by the magnification of the projection

$$m = \frac{DM + MZ}{DM} \tag{6.2}$$

In case of a near-field source at a distance MZ from the mask, the shadowgram will be characterised by the same magnification factor. As a consequence, the deconvolution array G also needs to be magnified by the same factor before the deconvolution and the shifts '+i' and '+j' in 6.1 are also in the same magnified units. Following from this discussion, it is possible to deduce that $SPP^{l,m}(i,j)$ at fixed k and $G(i+l, j+m)$ are the same array, and cross correlation and back projection as described by 3.4 are equivalent in the case of a static detector.

6.1.3 Balanced Back-Projection

It is necessary to apply to the 3D SPPs an appropriate normalization in order to obtain optimal background characteristics in the final images. In order to describe the normalization that was used for the SPPs, it is useful to make some considerations on proper balancing of coded mask images obtained via deconvolution, from which back-projection was derived and to which is equivalent. Balancing, described in depth in section 1.4, is a technique that consists of normalising the deconvolution array G so that the sidelobes of the PSF are zero, or as close as zero as possible.

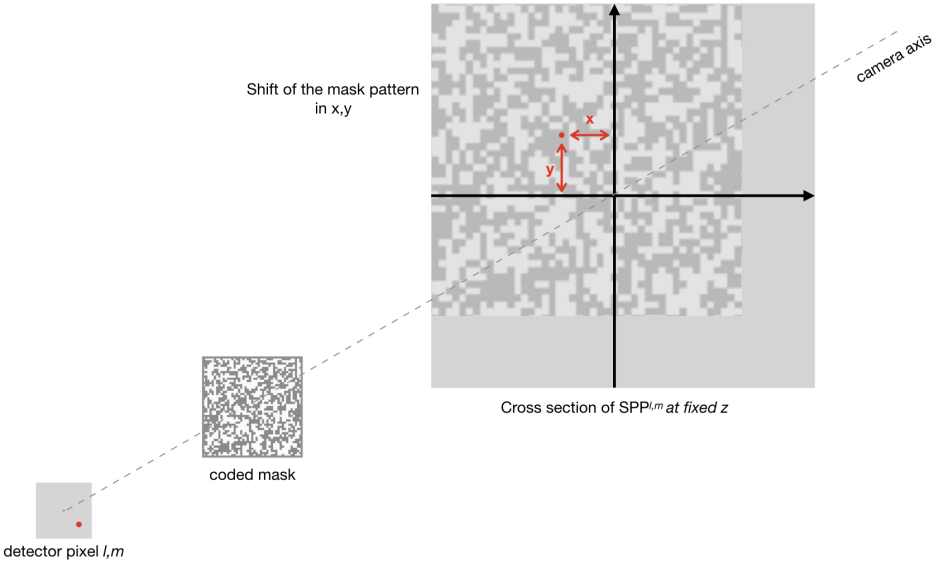

FIGURE 6.2: Back-projection of a photon at a fixed z. The magnified projection is shown on the right. This diagram shows that for a static system, back-projection and cross-corrrelation are equivalent

MURA patterns are so popular because they produce flat SACF sidelobes. The sidelobes are also equal to zero if the mask pattern is correlated with the appropriate deconvolution array G constructed with equation 1.12 (32). It is important to consider that when translating the correlation properties of MURA patterns, or any pattern in general, to imaging, additional effects need to be taken into account. One of these effects arises when the source under observation does not project the shadow of one basic pattern on the detector plane. This occurs when either of these conditions is met:

- The source is at such a distance that the magnified projection onto the detector plane is only a portion of the basic pattern.
- The source is not in the FCFOV.

In these cases the image background is not flat, but presents some structures. These structures caused the lower SNR at some values of z in figure 5.16. This effect is shown in figure 6.3. the top panel of figure 6.3 shows three different scenarios: In (a), one full basic MURA pattern is projected on the detector plane. In (b), due to the source being off-axis, only a portion of the MURA basic pattern is projected onto the detector plane. Finally, in (c), the source is closer to the coded mask, projecting a magnified shadow of the mask on the detector plane. The central panel of figure 6.3 shows the shadowgrams corresponding to these three scenarios. Finally, the bottom panel of figure 6.3 shows the images deconvolved from the shadowgrams using equation 1.12 as a deconvolution array. It can be observed that, while the correlation of the full basic pattern with the deconvolution array produces a 'perfect' image with 0 background, some artifacts are clearly visible in the images obtained by deconvolving only a portion of the basic pattern corresponding to a source in the PCFOV (6.3 b) or a source that produces a 2x magnification on the detector plane (6.3 c).

It is interesting to examine how a random mask behaves in similar situations. Assuming the coded mask has a random nature at every scale, a random-looking background is created even when only part of the mask pattern is sampled by the detector. This effect is shown in figure 6.4. The top panel of figure 6.4 shows, similarly to the central panel of figure 6.3, the shape of the shadowgrams that a source would create on a detector plane in three different cases, but this time using a random pattern for the coded mask. On the left, the entirety of the pattern is projected on the detector. In (b) a source in the PCFOV only projects a part of the full pattern on the detector plane. In (c) the source projects a magnified pattern on the detector plane and, as a consequence, only the central portion of the pattern is recorded by the detector. The bottom panel of figure 6.4 shows the images obtained by cross-correlation

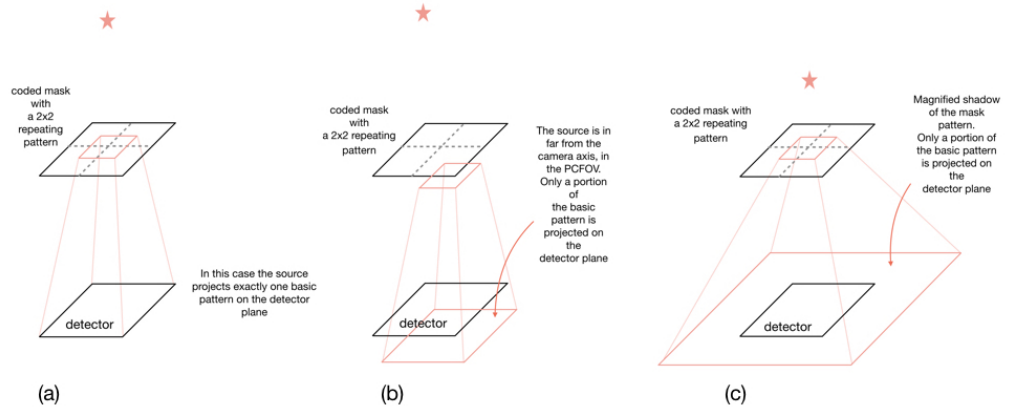

Diagram representing source and coded mask system in different configurations: (a) a source is on-axis and projects one full basic pattern on the detector plane. (b) The source is positioned off-axis. Only a portion of the basic pattern is projected on the detector plane. (c) The source is closer tho the detector than in (a), and produces a magnified shadow of the mask pattern on the detector plane

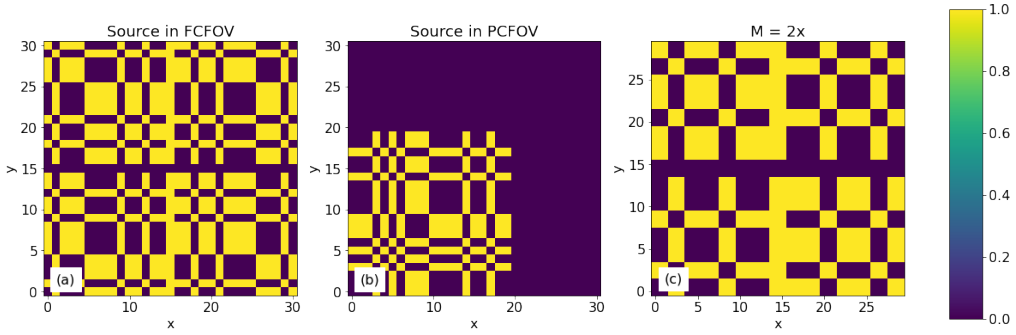

Shadowgrams corresponding to the three different scenarios described in the top panel of this figure: (a) one full basic pattern is projected on the detector plane. (b) only part of the pattern is projected on the detector plane. (c) a magnified mask pattern is projected on the detector plane. In this case, the magnification factor is 2

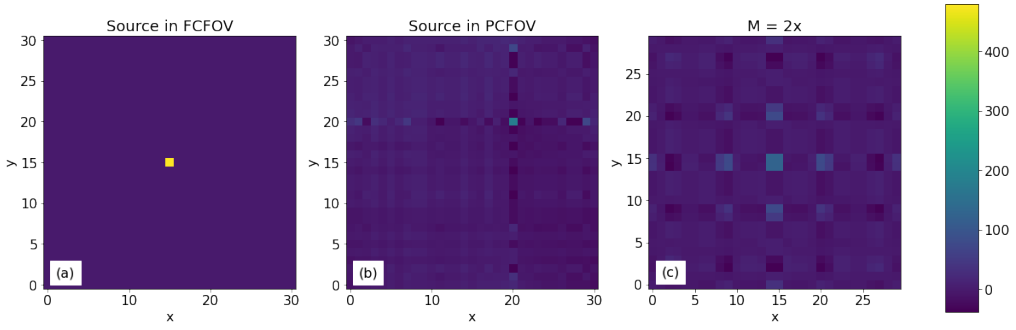

The shadowgrams represented in the central panel of this figure have been deconvolved using a standard MURA deconvolution pattern, constructed using equation 1.12

FIGURE 6.3

with the deconvolution array 1.14. In both cases with MURA and random patterns the height of the peak depends on the sum of the values in the portion of the mask pattern used (the 'number of counts' in the shadowgram).

The main difference between optimised arrays like MURAs and random arrays

comes into play in real world scenarios, where the shadowgrams are characterised by background counts in the detector pixels. To illustrate this scenario, a flat 'background' of 0.5 was added to the zero pixels in figures 6.3b(a) and 6.4a (a) to simulate a situation when a shadowgram from a point source has a number of background counts equal to 50% of the number of counts in the illuminated pixels. The cross correlation between these arrays and the appropriate deconvolution arrays extended to the PCFOV is displayed in figure 6.6. Both images have been normalised to show a unity peak height, and the peak has been masked to enable the comparison of the background features or absence thereof: if we only consider the FCFOV, while the MURA image presents a flat background, equal to the number of background counts in the shadowgram, the random image has clear artefacts that do not depend on the source position and which amplitude can reach 10% of the peak value. Artefacts, in the form of a horizontal and a vertical bands crossing the image, are also visible in the PCFOV of the MURA image.

These structures are created by an incorrect balancing. In fact, while the choice of the deconvolution array normally used for MURA images assumes a 50% transmission, this is not true for regions of space that project something different than one basic pattern onto the detector plane.

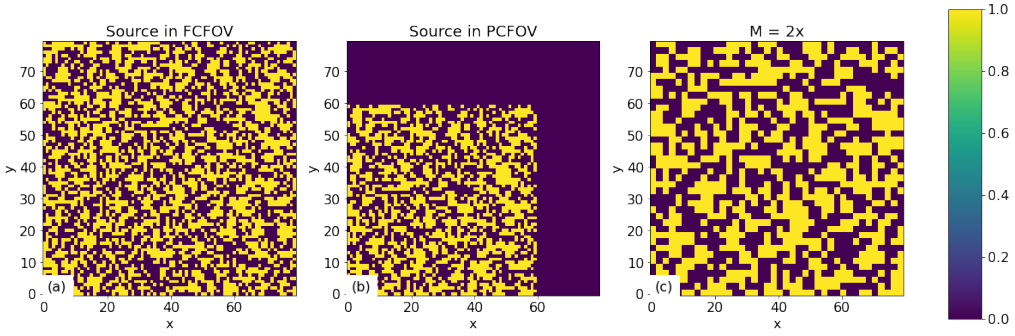

Portions of a 80x80 random pattern corresponding to: (a) a source projecting one full basic pattern on the detector plane. (b) a source in the PCFOV. (c) a source producing a magnified mask pattern shadow on the detector plane with magnification 2.

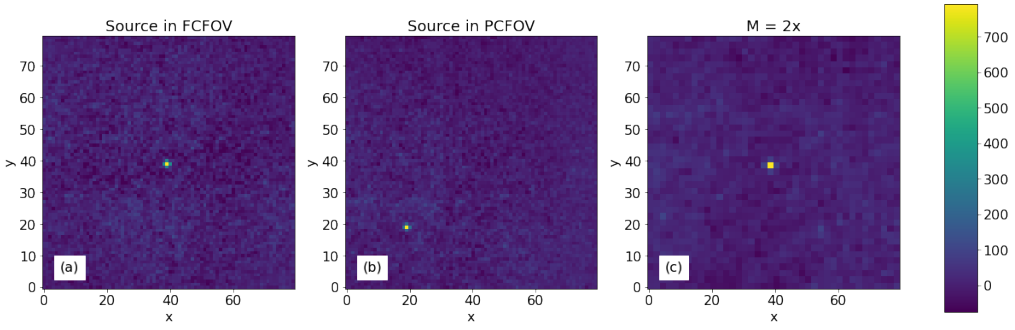

Cross-correlation of the patterns above with a random deconvolution array(18)

FIGURE 6.4

In order to restore a flat background in absence of sources, the negative part of the deconvolution array needs to be normalised. The normalisation or balancing factor is

$$B_{i,j,k} = \sum_{i,j,k} \frac{n^{+}_{i,j,k}}{n^{-}_{i,j,k}}, \tag{6.3}$$

where n^{+} is the number of detector pixels that can see the position of the voxel i, j, k through an opening in the mask, while n^{-} the number of detector pixel that do not have voxel i, j, k on a line of sight because the closed elements of the mask are blocking its view. The value B is a property of the position in the field of view that

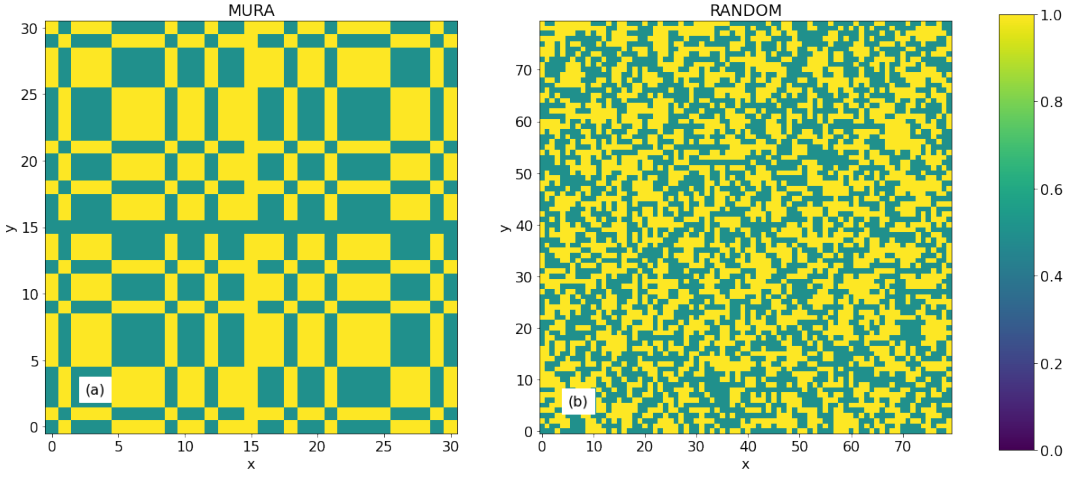

FIGURE 6.5: Simulated shadowgrams of a point source with a MURA (left) and a random mask pattern (right). Both shadowgrams have a non-zero background level in non illuminated pixels

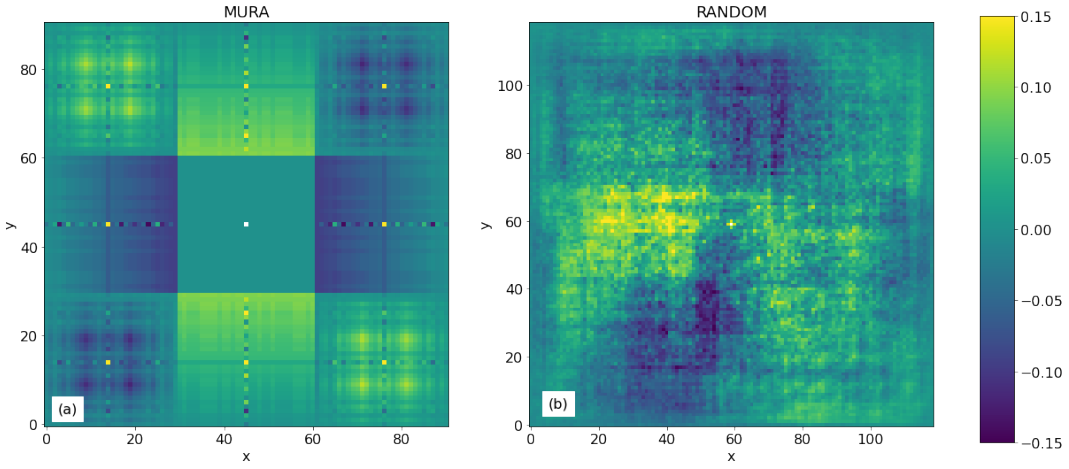

FIGURE 6.6: Simulated images of a point source with a MURA and a random mask pattern without image balancing. The images are normalised to the peak intensity and the source has been masked to highlight the background features

depends on the geometry of the system and represents the local transparency of the mask, or the transparency of the subportion of the mask projected on the detector plane by a source in that position. Figure 6.7 shows the cross correlations of the patterns in figure 6.5 with a deconvolution array balanced as follows(26):

$$I_{i,j} = \sum_{k,l} G^{+}_{i+k,j+l} D_{k,l} - B_{i,j} \sum_{k,l} G^{-}_{i+k,j+l} D_{k,l} \tag{6.4}$$

This normalisation will affect the final image by flattening the background and removing the artefacts. The same correction can be applied to the SPP in order to obtain a flat background in the 3D images. With reference to section 3.2.1, each 3D SPPs was constructed as:

$$SPP^{d,m}_{i,j,k} = \begin{cases} 1, & \text{if voxel i, j ,k is in region A} \\ 0.5, & \text{if voxel i, j, k is in region B} \\ 0.25, & \text{if voxel i, j, k is region C} \\ -B_{i,j,k}, & \text{if m is closed} \end{cases} \tag{6.5}$$

The only difference between balanced and unbalanced SPPs is that the balancing will modulate the negative part of the SPPs to account for the local transparency of the mask. The sum of $SPP^{d,m}$ as described by equation 3.4 will generate a 3D image where the background is zero both in the FCFOV and in the PCFOV.

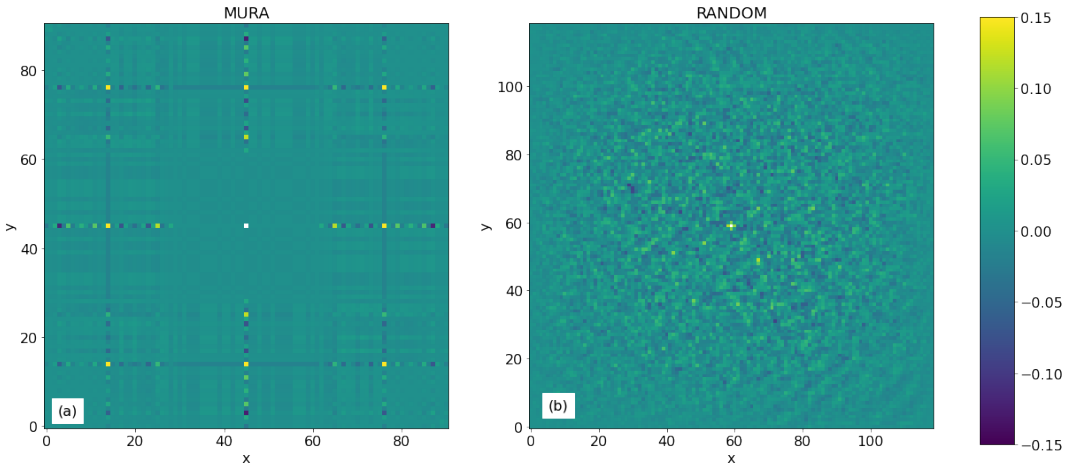

FIGURE 6.7: Simulated balanced images of a point source with a MURA and a random mask pattern after image balancing. The images are normalised to the peak intensity and the source has been masked to highlight the background features

6.2 The CLEAN Algorithm

After reconstruction, images obtained by back-projection are processed with a version of an algorithm called CLEAN. CLEAN is a family of algorithms devised by J.A. Högbom(62), which are normally used to process radio interferometry maps to reduce or eliminate sidelobes in the images. The knowledge of the response of the instrument is used to identify and remove these systematic artifacts in radio images. The same algorithm can be applied to suppress the coding noise in coded mask images. The CLEAN algorithm acts on the raw image resulting from equation 3.4 in the 3D FOV and produces a clean image. The correct application of CLEAN is based on two assumptions: any source in the field FOV can be described as composed of a certain number of point sources, for which the PSF of the imaging instrument is known, and the position of the voxel with highest intensity in the image is part of the source.

Figure 6.8 is a flow-chart describing each step of CLEAN that also includes the illustration of its application to a simple 1D case. CLEAN was implemented as a python code with the following inputs:

- **R** - The raw image resulting from equation 3.4
- **C** - An empty 3D array of the same size as the raw image which will store the final cleaned image

CLEAN is then implemented through the following steps:

- In the raw image, find the voxel $R_{i,j,k}$ with highest value I_{max} and calculate its position in the FOV.
- Compute $PSF^{i,j,k}$, which is the point spread function of the instrument for a point source in voxel i, j, k. Note that $PSF^{i,j,k}$ is characterised only by coding noise and does not have noise deriving from counts statistics or detector noise.
- Normalise $PSF^{i,j,k}$

$$PSF^{i,j,k}_{norm} = PSF^{i,j,k} \frac{I_{max}}{max(PSF^{i,j,k})} \tag{6.6}$$

- Subtract $gPSF^{i,j,k}_{norm}$ from R. The factor g is known as loop gain and is fixed at an arbitrary value between 0.01 and 0.1. The loop gain is the fractional value of the PSF that is subtracted at each iteration.

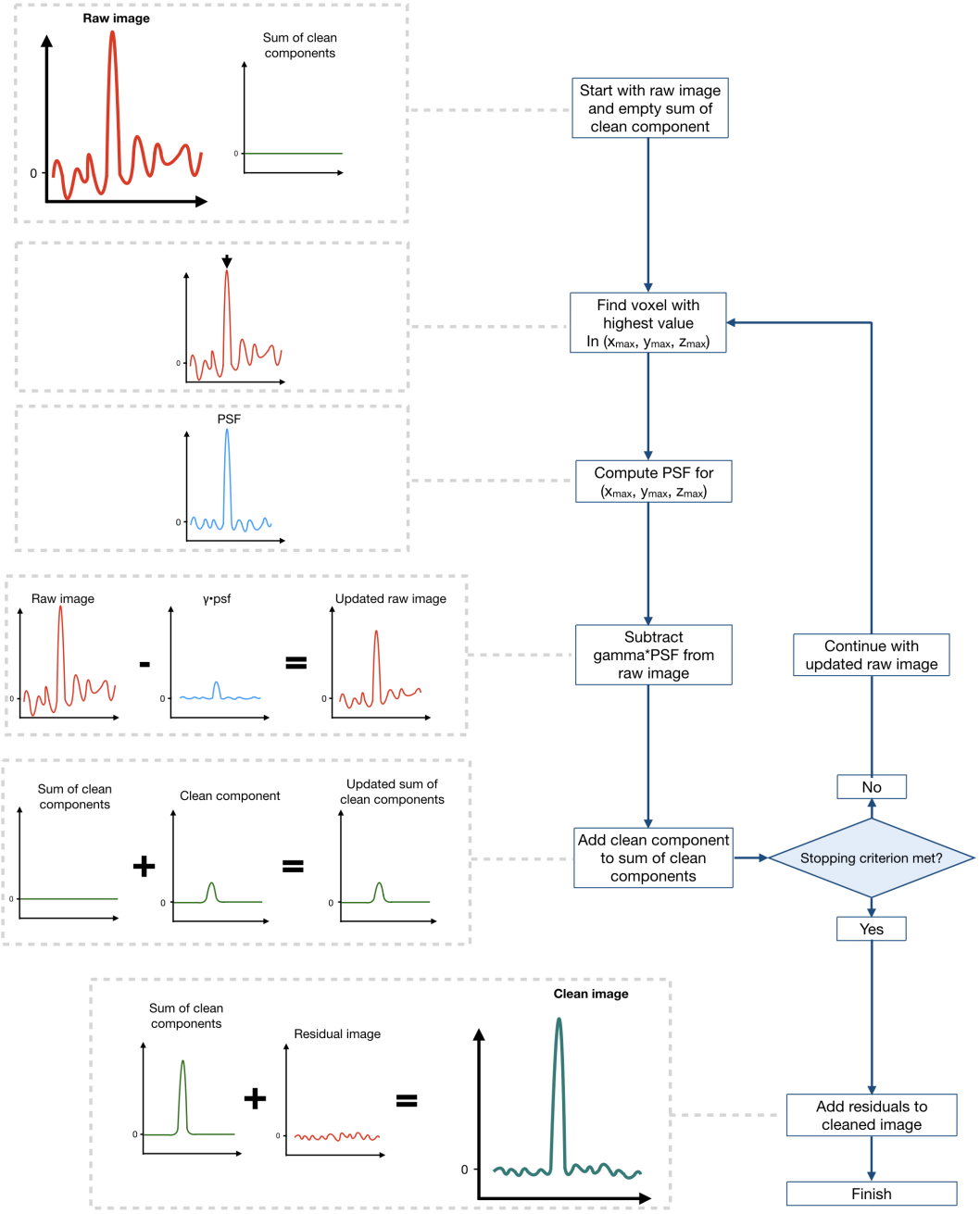

FIGURE 6.8: Flow chart of the CLEAN algorithm, with a one dimensional representation of each stage. Clean identifies and removes the coding noise from the back-projected images, producing a cleaned image with reduced background

- Add a clean component to C. This component is the point source that would generate $PSF^{i,j,k}_{norm}$ as an image, after being convolved with the know space resolution of the camera.

The above steps are repeated iteratively as R gets updated at every subtraction. The process is terminated when a stopping condition is met. The stopping condition can be one of the following, where the superscript n indicates the iteration number:

1. $I^n_{max} - I^{n+1}_{max}$ is smaller than a set threshold.
2. $max(C^{n+1}) - max(C^n)$ is smaller than a set threshold.
3. I^n_{max} is less than a determined number of σ_{R_n} (standard deviations in the raw image)

Clean operates by iteratively subtracting smaller and smaller components from the source in R while adding equally small components to C. Stopping criteria 1 and 2 consider the process over when the change in the peak in R or C is negligible. Stopping criterion 3 stops the iterations when the peak in R is considered indistinguishable from the noise. After the process is stopped, the residual noise in R is added back to C, which is the final output of CLEAN.

The value of the loop gain can be chosen between 1% and 10%. A high gain completes the cleaning process faster, but the components subtracted form R and added to C at each iteration have greater values. As a consequence the process is less conservative in case at some point the brightest pixel is a noise feature and not part of the source.

6.2.1 Calculation of $PSF^{i,j,k}$

The $PSF^{i,j,k}$ are calculated using a piece of code written in python and ran on a GPU by means of Numba. With a ray tracing method the code calculates which detector pixels of each camera are fully or partially illuminated by a point source in i, j, k. An 'image' of the detector is then produced where the detector pixels have an intensity value ranging from 0 to 1 according to their PIF. These images are then processed with back projection to reconstruct $PSF^{i,j,k}$. To save computing time, once computed, $PSF^{i,j,k}$ is stored in memory for later access.

One of the limitations of the algorithm is the case when the image is so noisy that the brightest pixel is part of the features resulting from the coding artifacts. In this situation the second assumption no longer holds, and the cleaned image will present

a source in the position of the coding artifacts. Experimental tests will show that this occurs when extended sources are in the FOV and the total level of noise in R is quite high. Byard(63) also presented a version of this algorithm that determines the 3D position of point-like sources and treats the artifacts in the image operating on the detector shadowgram rather than in the final image.

6.3 Conclusions

This chapter has described the methods used to produce 3D coded mask images in a near-field scenario. The modifications made to the back-projection algorithms and a post-processing algorithm used to enhance the sources and suppress the noise have been described. These methods, which will be applied to experimental data in the next chapter, are computationally expensive and may pose an obstacle to real time imaging in the near future. However, moderate processing times are achievable with a relatively inexpensive hardware setup.

Chapter 7

The Dual-View Coded Aperture Mask Camera

This chapter applies the methods and techniques described in chapter 6 to a prototype coded mask imaging system that was designed and developed in this project. Trials with different types of isotopes were carried out and the results are summarised in this chapter. Sections 7.1 to 7.4 describe the design features of the camera and the parameters taken into account in the development of the prototype. Section 7.5 reports the calibration phase of the detectors. The experimental phase of the project is described in section 7.6. Tests were carried out at the Nuclear Medicine Departments of the Royal Surrey County Hospital and the Southampton General Hospital. The time available for the test was 24 hours, divided into three days of trials. Given the time constraints, it was decided to carry out three tests, imaging three different sources in the FOV: point sources, a hollow sphere phantom, and one extended cylindrical source. Sections 7.7 and 7.9, finally, presents the images obtained, the results obtained and the final remarks on the experiments.

7.1 The Imaging System

The Dual-View Coded Aperture Mask camera (2V-CAM) is the prototype that was designed, assembled and tested in this research project. Figure 7.1 shows pictures of the finished camera, which was built using commercially available as well as custom-made components. The main feature of the camera is the presence of two orthogonal arms that observe the source simultaneously. Each arm is assembled on an aluminum rail system by means of custom made mounts and is represented in the diagram in figure 7.2. This makes the prototype extremely flexible for adjustments in the geometry of the system and potential upgrades of the detector module

or mask. The design of this particular model was guided by two criteria, which were necessary for the validation of the technique. First, the the field of view must be sufficiently large to image the phantom planned for the experiment (about 10 $\times$10$\times$10 cm). Larger field of view can be achieved by increasing the detector or mask area according to the clinical needs of the camera. Second, the 3D spatial resolution across the imaging volume must be similar or better than the one of current SPECT systems, which is 7-12mm.

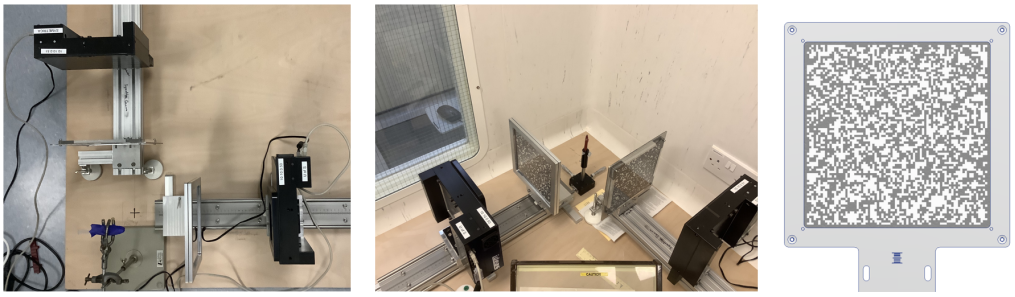

FIGURE 7.1: (a) and (b): Pictures of the imaging system during the experiments The two detectors in their black casings and the coded masks are fixed on two metal rails placed at a 90 degree angle. The source is placed where the axes of the two cameras meet, which is the centre of the FOV. (c) A drawing of the coded mask with the chosen pattern in its supporting frame

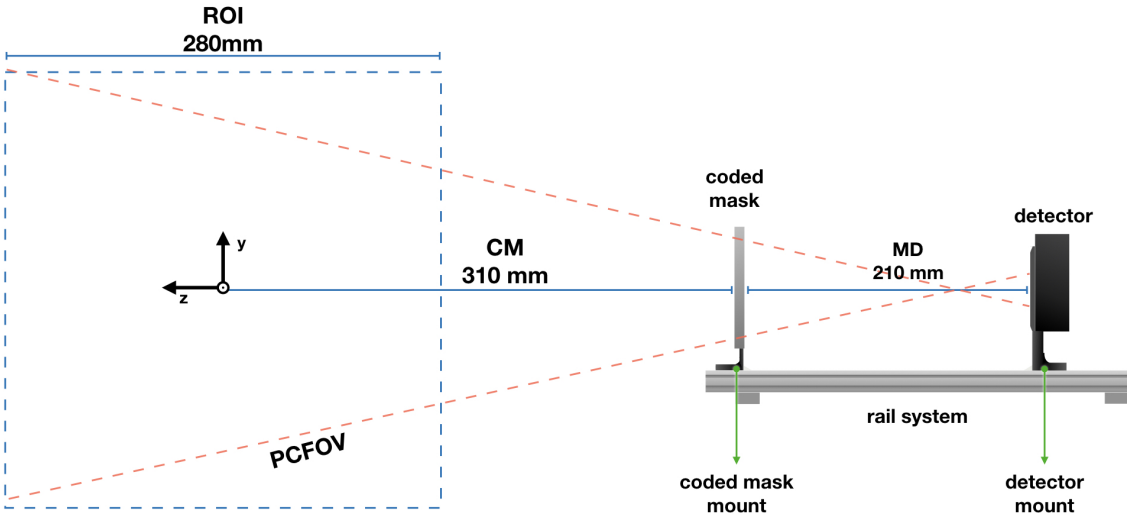

FIGURE 7.2: Each head of the 2V-CAM is composed of a detector assembly and a mask assembly mounted on a rail. Each part of the system can be moved independently to change the specification of the imager

7.2 The Detector Assembly

Two IDEAS gamma camera modules (64) were used to equip the camera heads. The sensing layer of the camera is composed of a number of modules which are pixelated CZT mono-crystals, each connected to 256 front end channels, giving an area of 16x16 pixels. Figure 7.3a shows a picture of the detector case, where each module has been marked. Modules 4,5,7,8 were purchased at first and the cameras were upgraded in the course of the project by adding modules 1,2,3, 6 and 9 to increase the sensitive area. After the upgrade, each camera has 3×3 modules, each consisting of 16x16 1.6mm $\times$ 1.6mm 5mm thick pixels for a total active area of 26.21cm^2. In the detector front-end, the sensor signal generated by the gamma-ray is amplified, pulse-shaped and compared to a threshold configurable by the user. The energy information is then converted to an ADC value and recorded together with the pixel location. The detector bias voltage is set to the default value $-522V$. Imaging data are transmitted to a computer via the Ethernet port shown in figure 7.3b. The gamma camera was set by the manufacturer in its low-energy configuration, which is sensitive to gamma photons up to 350 keV.

7.2.1 The Input/Output Software

The IDEAS gamma cameras that equip 2V-CAM communicate via Ethernet connection using a TCP protocol for control and monitoring and a UDP protocol for read-out data. A network switch was used to connect both cameras to the PCs used for data acquisition. A software written in Python was used to control both cameras and interpret the data packets received by the instrument to obtain images and spectra.

7.3 The Coded Mask

The coded mask used to build the camera is made of a 2mm thick layer of lead. Figure 7.4 shows the absorption properties of lead compared to tungsten for 140 keV photons. A 2mm thick layer of lead blocks 99.5% of the photons, while the same thickness of tungsten blocks 99.9%. The disadvantage of a lower absorption is compensated by a much easier manufacturing process of a lead mask, which does not require advanced techniques like metal laser-cutting and could be produced at the mechanical workshop in the Physics Department at University of Southampton. The coded mask mounted on 2V-Cam is consists of an 80x80 pixel random pattern with a pixel size of 2.2 $\times$ 2.2 mm^2. This value is small enough to fulfill the requirements

(A) Modules of the 9x9 IDEAS camera

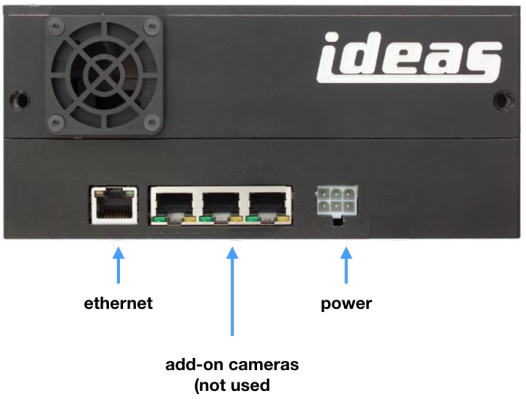

(B) Side view of the IDEAS CZT camera. Connections are to power and computer are indicated

FIGURE 7.3

for lateral resolution, without being affected by effects self-collimation in the central 10 cm $\times$ 10cm $\times$ 10cm of the FOV.

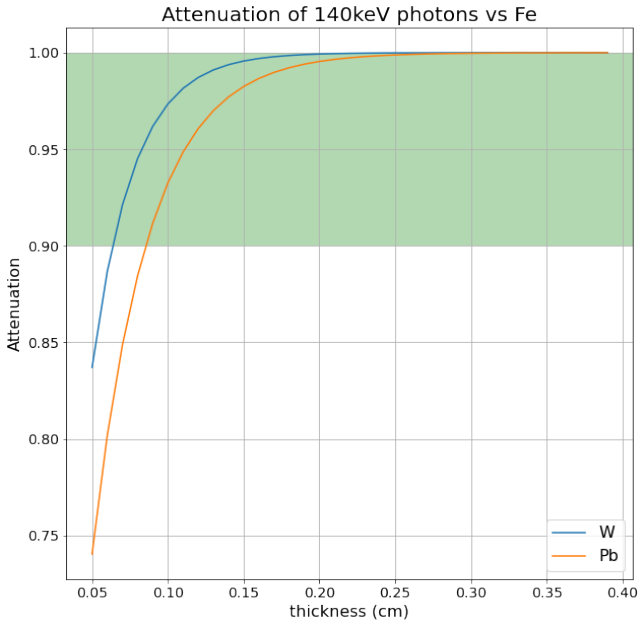

FIGURE 7.4: Absorption of 140 *keV* photons in tungsten and lead. The green area highlights absorption greater than 90%

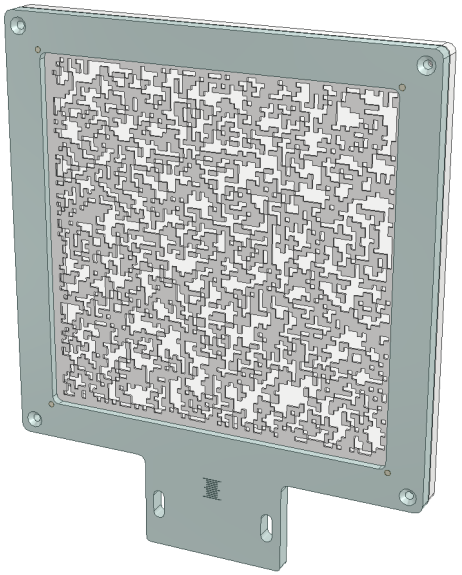

FIGURE 7.5: Drawing of the coded mask used for the prototype camera in its support. Two layers of perspex was used to hold the coded mask in the aluminium frame

7.3.1 A Modified Random Pattern

The small pixel dimension makes the construction of a supporting structure for the coded mask impractical. For this reason a compromise was reached between true randomness of the coded aperture pattern and its capability to support itself. Figure 7.6a represents a randomly generated 2D pattern. This is characterised by the presence of islands, which are pixels or groups of pixels which are not connected to the external frame. Each mask pixel is considered supported if at least one of its corners is connected to the main structure. In order to obtain a self supporting structure, these islands were repositioned in order to be supported. Figure 7.6b shows that, in a sample of 10000 randomly generated patterns, the average number of islands is around 20, and the average area of islands is corresponds to 41 pixels. Since this is only 0.64% of the mask area, it was concluded that the randomness of the mask is not compromised by changing the value of a small number of pixels. The modified random pattern chosen to equip the 2V-CAM, detector is shown on the right in figure 7.6a.

7.4 The Geometry of 2V-CAM

This section will describe how the prototype camera was assembled, in the light of the design requirements and considerations made in chapters 5 and 6.

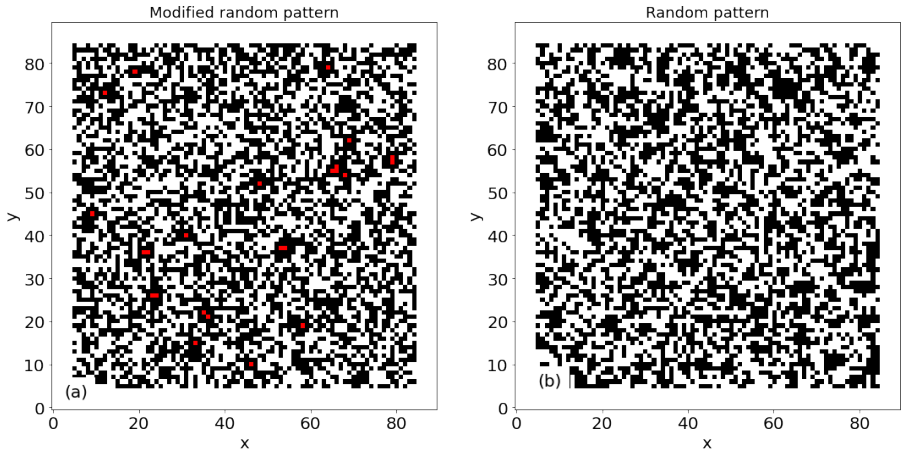

(A) (a) An example of a random coded mask pattern. Island pixels are highlighted in red. (b) The modified random pattern used to equip both 2V-CAM heads. The random pattern was slightly modified to be made self-supporting. Islands were moved by hand to be connected to the main structure of the coded mask.

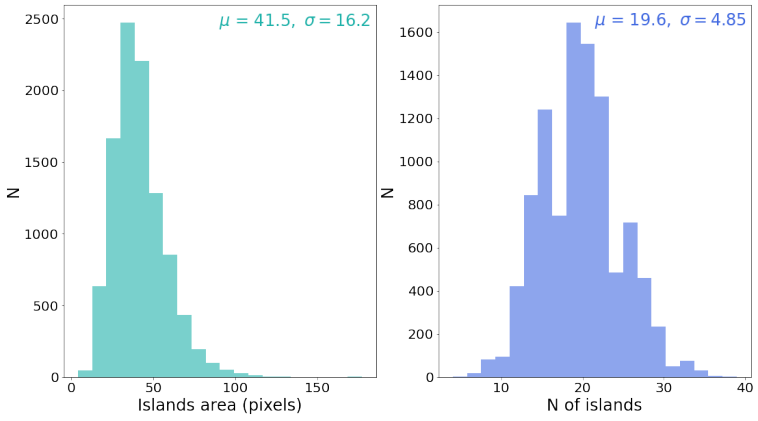

(B) Distributions of the total area of the islands (right) and the number of islands expressed in units of pixels (left) in a sample of 10000 random patterns.

FIGURE 7.6: The design of the mask pattern was developed to obtain a reasonably random mask that was also self supporting

7.4.1 Field of View

The FOV of the dual-head camera is the region of space that is visible by both cameras. Figure 7.7 shows a diagram the top view of 2V-CAM, where the boundaries of each arm's FOV are marked in a red dashed line. The resulting FOV is composed of the regions of space where the two single arm PCFOVs overlap. The FOV is enclosed in an imaging volume of 280mm $\times$ 280mm $\times$ 280mm which is drawn in a blue dashed line and is the space represented in the SPPs. Figure 7.7 also shows the frame of reference used for image reconstruction and post-reconstruction processing. Each camera is placed at a distance of 210mm from the coded mask, which is at 310mm from the centre of the FOV.

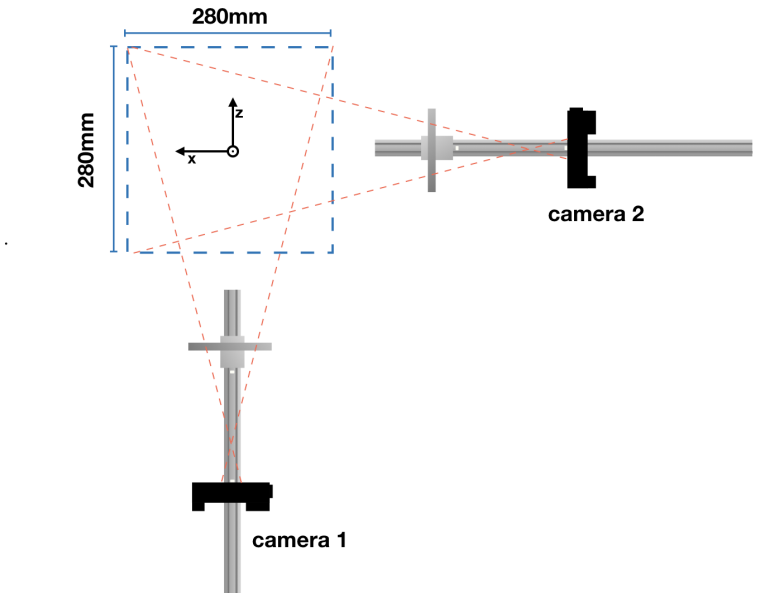

FIGURE 7.7: Top view of the 2V-CAM imaging system . The red dashed lines represent the PCFOV of each camera system and show their intersection

7.4.2 Transversal and Longitudinal Resolution

The diagram in figure 7.7 represents the top view of the 2V-CAM system, composed of two identical arms observing the target from two different angles. In order to explain this design choice it is useful to resort to point source simulations, in order to understand the effect that adding a second camera has on the overall resolution of the system. A sample of 1000 PSFs was computed as described in section 6.2.1 by selecting a random set of positions in the FOV from a uniform distribution. An example of a single-head PSF is shown in figure 7.8. The poor resolution along the camera axis is clearly visible in this image. The PSF shape is elongated along the axis that connects the centre of the detector and the source position. The FWHM of the PSF was calculated by finding the voxels enclosing the surface with intensity $\geq$ 50% of the peak value of the PSF. The largest distance between couples of boundary voxels is an estimates of the longitudinal FWHM of the PSF. The transversal FWHM of the PSF was estimated as twice the shortest distance between the centroid and each of the boundary voxels. Figures 7.9a and 7.9b represents the distributions of the transversal and longitudinal FHWM in the whole sample of PSFs. The transversal and longitudinal resolution of 2V-CAM were estimated as the mean value of these distributions. The mean value of the transversal size of the PSF is 9.1mm with a standard deviation of 0.8mm. The longitudinal size of the PSF is approximately one order of magnitude higher, with an average value of 94.2mm and a standard deviation of 12.3mm.

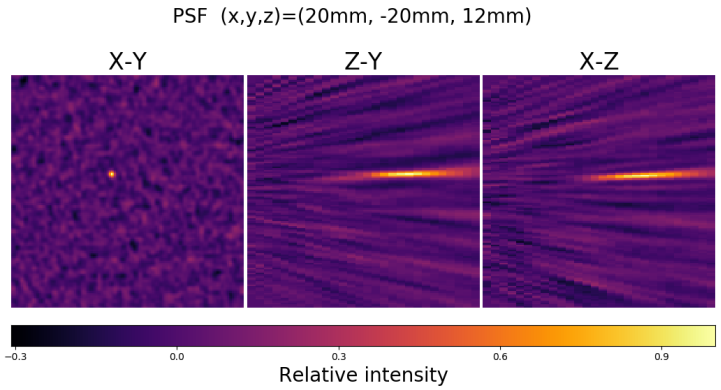

(A)

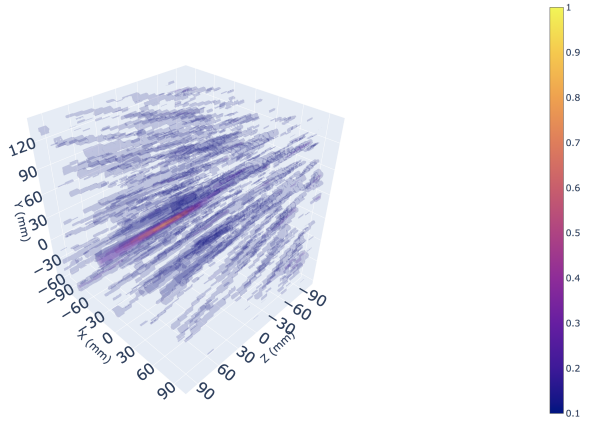

(B)

FIGURE 7.8: 2D (A) and 3D (B) plot of the PSF of a source at x=20mm, y=-20mm, z=12mm. The plots show the typical elongated shape for a single view of the source

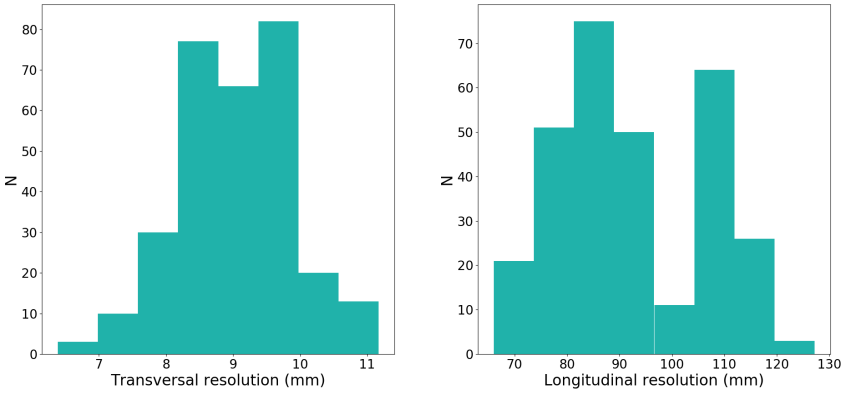

(A) (B)

FIGURE 7.9: Histograms of the transversal (A) and longitudinal (B) FWHM of the 2V-CAM PSF for 100 random positions in the PCFOV. The PSF is characterised by its elongated shape, due to the lower resolution along the camera axis.

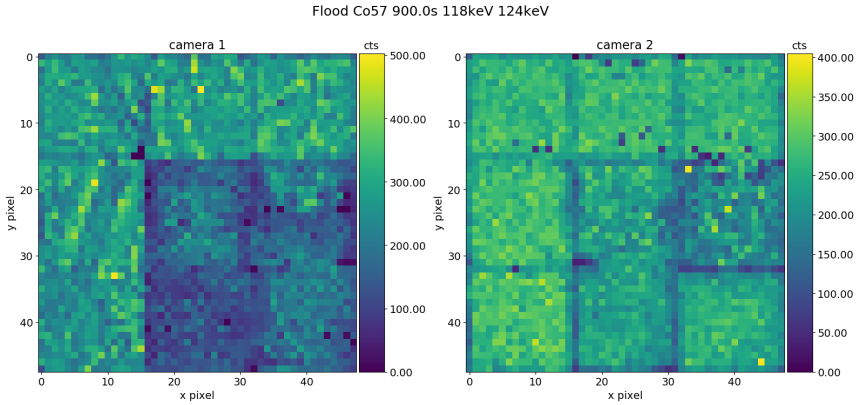

FIGURE 7.10: Detector image of the flood illumination with ^{57}Co

Isotope	Acquisition time (s)	Activity (MBq)	Total counts detector 1	Total counts detector 2
^{57}Co	900	3.7	2342029	2283222
^{99m}Tc	900	1.017	2527911	2317284
^{177}Lu	300	58.4	9286287	8968501
^{123}I	300	66.7	11020200	9537886

TABLE 7.1: Parameters of the calibration exposures. The Activity of each source is referring to the start of the acquisition

A single coded mask camera provides lines of response through the field of view that are spread over a relatively narrow range of angles. As a result, although a single camera does produce a 3D image, the resolution along the camera's axis can be up to an order of magnitude worse that the lateral resolution. The axial resolution can be improved by using two cameras, each observing the source from a different angle, in a stereoscopic observation. The combination of images from both cameras produces a 3D image with an optimised lateral resolution along the axes of both cameras with a single view of the target.

7.5 Detector Calibration

Both detectors include a factory calibration. Nonetheless, each pixel in the detector was energy calibrated. The image in the detector plane was also corrected for uniformity defects using flood exposures with various sources. Before data acquisition, both detectors have been exposed with flood illuminations of ^{57}Co, ^{99m}Tc, ^{177}Lu and ^{123}I. The coded masks were removed from the rails and each source was positioned at the centre of the field of view for an extended exposure. Table 7.1 shows the details of each acquisition.

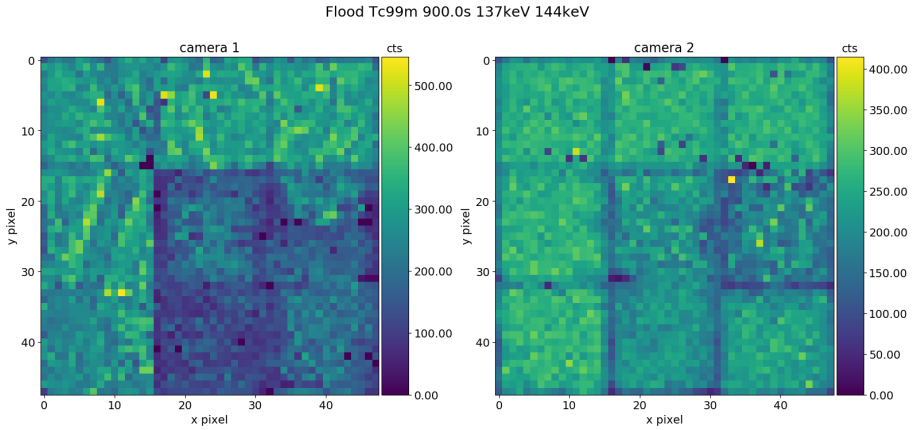

FIGURE 7.11: Detector image of the flood illumination with ^{99m}Tc

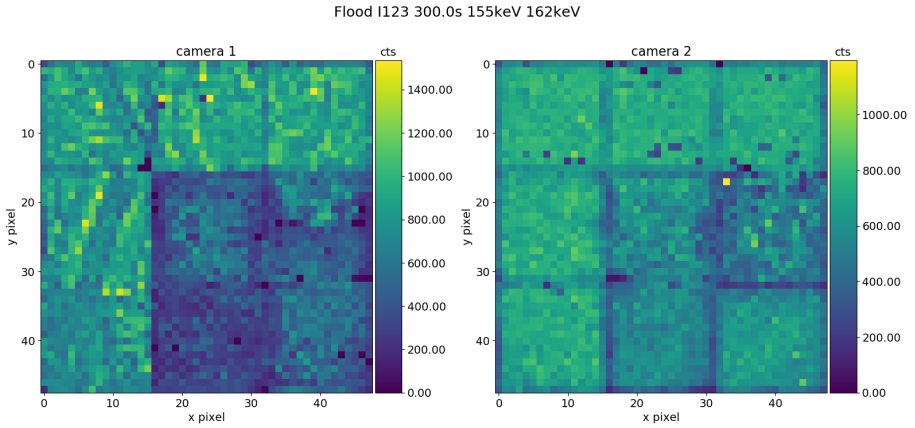

FIGURE 7.12: Detector image of the flood illumination with ^{123}I

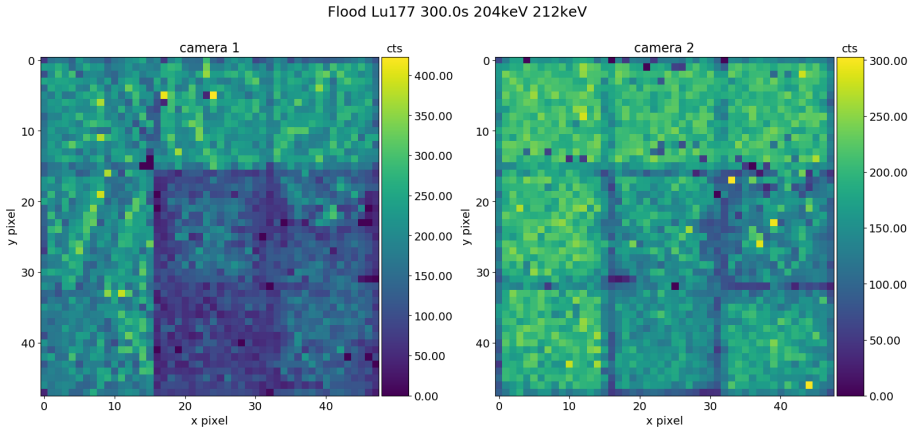

FIGURE 7.13: Detector image of the flood illumination with ^{177}Lu

7.5.1 Uniformity Calibration of the CZT Detectors

Figures 7.10, 7.11, 7.12 and 7.13 show the flood illumination maps of both detectors with the four isotopes. Camera 1 appears to have a different detection efficiency between the modules that were first purchased and the ones that were added a few months later. This difference have been attributed to differences in the CZT of the upgrade modules which were sourced from a different supplier than the original modules. In addition, some modules in camera 1 show variations in brightness within the module. Camera 2, on the other hand, shows a lower detection efficiency along the borders of each module. It is unclear whether these effects are attributed to the CZT crystal or the readout system. Both cameras also show 'noisy' pixels, with a number of counts disproportionately high with respect to the rest of the detector plane. To take the uniformity variations into account the high statistics flood exposures were used to build uniformity maps of the detector in the same energy windows used for image reconstruction. Uniformity maps were calculated dividing the counts in each detector pixel by the highest number of counts recorded in a single pixel in the whole detector. This ratio is calculated after applying a sigma-clipping algorithm to the detector image, in order to exclude the noisy pixels. To apply the uniformity correction, the counts in each shadowgram pixel are divided by the corresponding value in the uniformity map before the image reconstruction stage.

7.5.2 Energy Calibration of the CZT Detectors

Each detector pixel was calibrated using the 122 keV peak of ^{57}Co, the 159 keV peak of ^{123}I, the 140.5 keV peak of ^{99m}Tc and the ^{177}Lu peaks at 113 keV and 208 keV. Figures 7.14a and 7.14b show the raw spectra of all the calibration sources. While all the characteristic peaks are visible, their FWHM is impacted by the slight variation of gain and baseline of each detector pixel. After the acquisition of a high statistics flood image with each one of the calibration isotopes, the spectra from each pixel were searched for their characteristic peaks, which were used to calibrate each pixel individually. The peak energy-DAQ channel plot for a selection of pixel is shown in figure 7.16. Figures 7.15a and 7.15b show the whole detector spectra after calibration: the FWHM of all the peaks is lower, showing that the dispersion around the true emission energy of the photons is reduced.

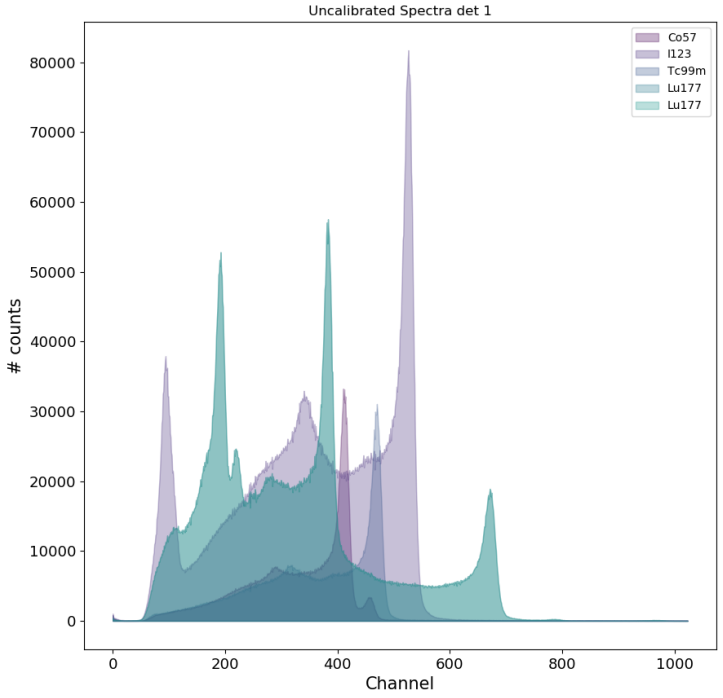

(A)

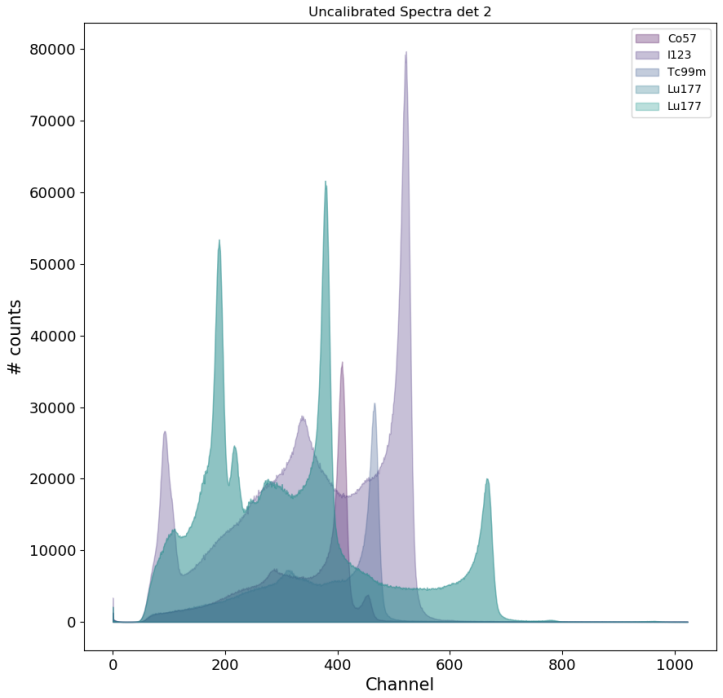

(B)

FIGURE 7.14: Spectra of the calibration sources from detector 1 (A) and detector 2 (B) with factory calibration

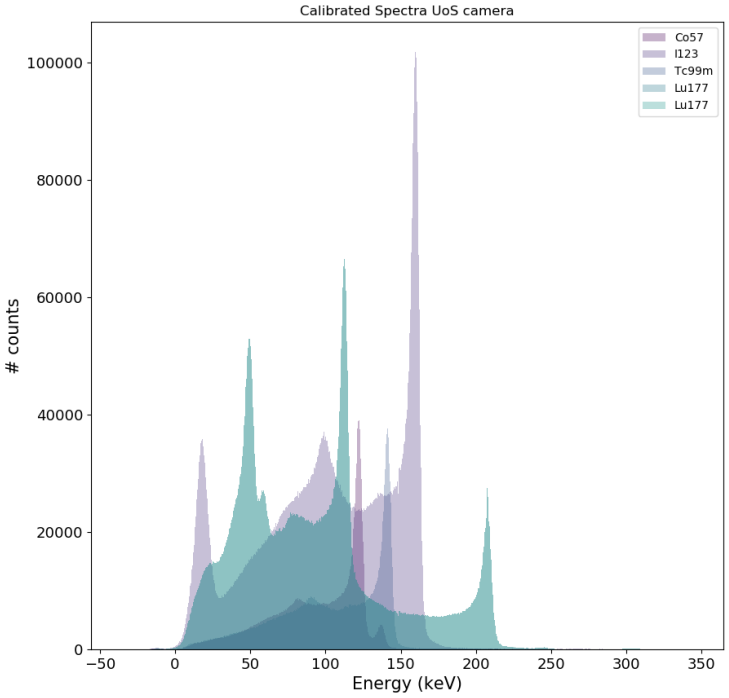

(A)

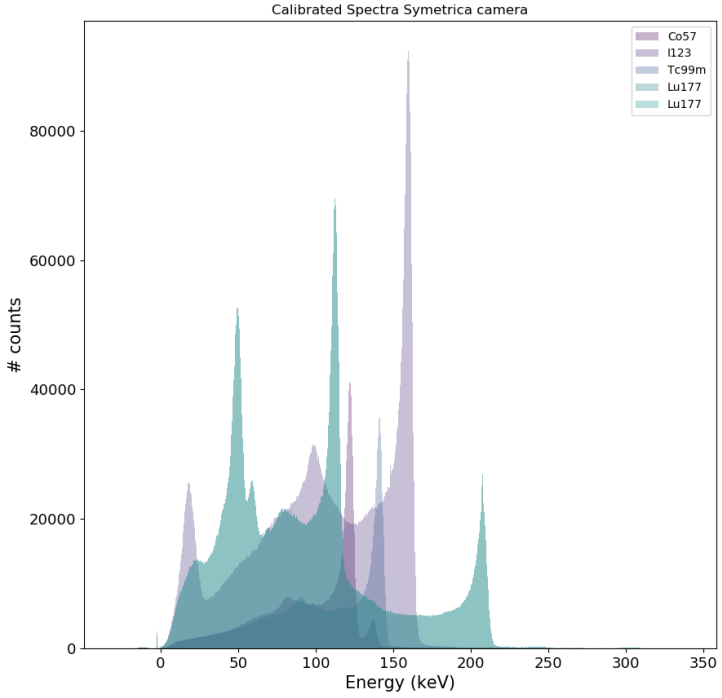

(B)

FIGURE 7.15: Spectra of the calibration sources from detector 1 (A) and detector 2 (B) after energy calibration. The application of appropriate calibration parameters to each single pixel improves the dispersion of the measured energy around the emission line and decreases the FWHM of the peak in the detector spectra

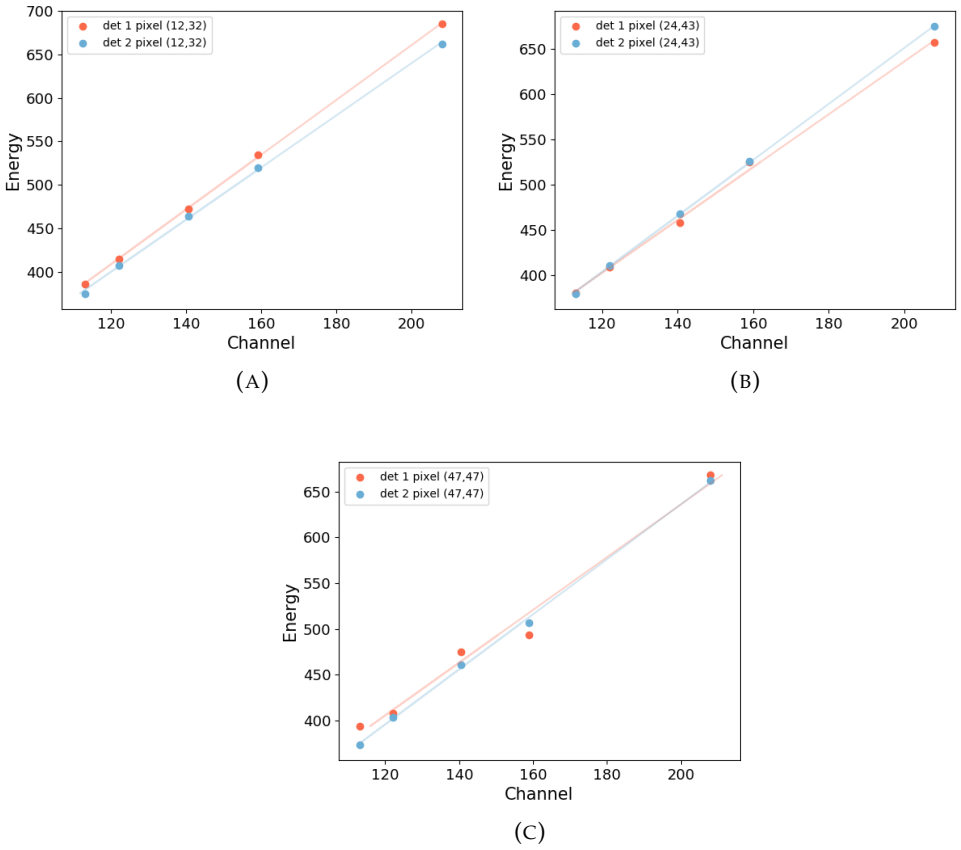

FIGURE 7.16: Energy calibration plots for three pixels of both detectors. Each pixel has a slightly different value of gain and offset and therefore needs to be calibrated individually

7.6 Data Acquisition

2V-CAM was tested with different types of sources in the laboratories of the Nuclear Medicine Departments of the Royal Surrey County Hospital and the Southampton General Hospital. The tests involved single and pairs of point sources, a single extended source, and a hollow sphere phantom.

7.6.1 Imaging Point Sources

The point source tests were carried out at the Nuclear Medicine Department of the Royal Surrey County Hospital. The point sources imaged during the tests were of three different isotopes, ^{57}Co, ^{99m}Tc and ^{123}I. The ^{57}Co source was a commercially available spot marker, ^{99m}Tc and ^{123}I were obtained by filling the tip of a 10 ml syringe with the isotope in water solution, forming a source with a cross-section of less than 1mm. Figure 7.17 is a picture of the set up of 2V-CAM during an image acquisition of a single ^{99m}Tc source.

FIGURE 7.17: 2V-CAM during the acquisition with a single ^{99m}Tc point source. The point source was obtained by filling the tip of a 10 ml syringe with a ^{99m}Tc in solution

Three images of point sources were collected: the single ^{99m}Tc point source and two images of pairs of sources, respectively ^{99m}Tc with ^{57}Co, and ^{99m}Tc with ^{123}I. The details of each acquisition are summarised in table 7.2. Energy cuts were applied to all data before image reconstruction. The energy bands used are 118-124 keV for ^{57}Co, 137-144 keV for ^{99m}Tc and 155-162 keV for ^{123}I. Figure 7.18 shows the shadowgrams of the three acquisition from camera 1 (top row) and camera 2 (bottom row). The left column represents the two shadowgrams of the single ^{99m}Tc source, which clearly show the shape of the mask pattern. The exposure with ^{99m}Tc and ^{57}Co point sources is shown in the middle column. The presence of two mask pattern shadows is barely noticeable. Lastly, the right-hand column shows the shadowgrams from the exposure with ^{99m}Tc and ^{123}I.

7.6.2 Imaging an Extended Source

The images of a single extended source were acquired at the Nuclear Medicine Department at the Southampton General Hospital. An extended source, pictured in figure 7.21, was prepared by filling a 5 ml syringe with a ^{99m}Tc solution in water. The source has a cylindrical shape with a base diameter of 12mm and a height of 25mm. Figure 7.20 shows the shadowgrams obtained by scanning the syringe in three different configurations: standing vertically, horizontally with the axis parallel to the axis of camera 1, and horizontally at an angle of 45 degrees to both camera axes. The details of the acquisition are shown in table 7.3. Although the mask pattern is not clearly recognisable, the orientation of the source relatively to each camera appears in the features in each shadowgram.

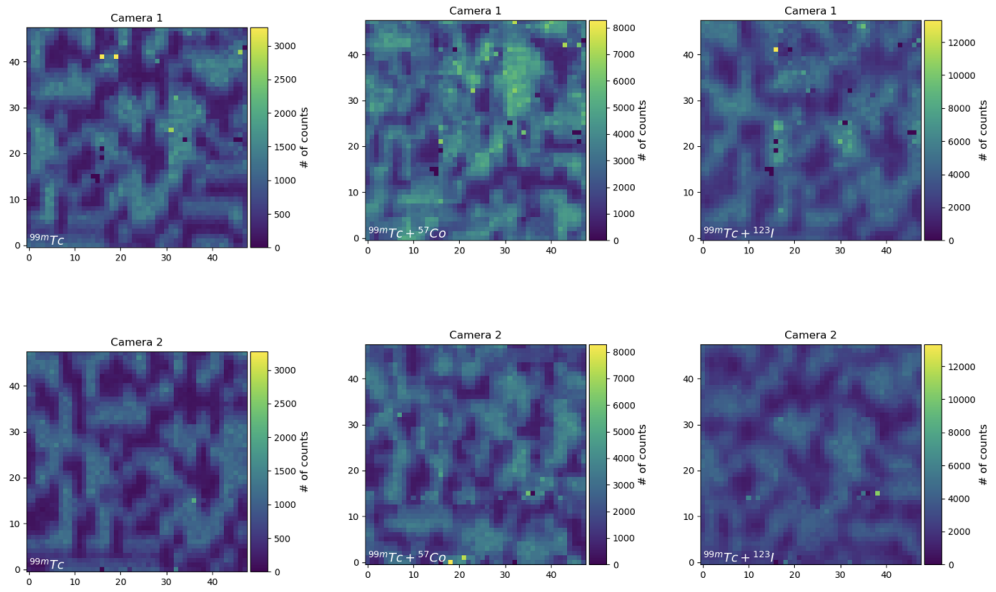

FIGURE 7.18: Detector images for point sources in 3 different configurations. (a) Single ^{99m}Tc point source. (b) ^{99m}Tc and ^{57}Co point sources. (c) ^{99m}Tc and ^{123}I point sources.

7.6.3 Imaging a Hollow Spheres Phantom

Gamma-ray images of a hollow sphere phantom were acquires in the Nuclear Medicine Department of the Royal Surrey County Hospital. The hollow sphere phantom shown in figure 7.21 is an ∼8.2 cm cylinder with a base of ∼4cm diameter. Four hollow spheres of diameter 3.95 mm, 4.95 mm, 6.23 mm and 7.86 mm can be placed inside the cylinder, approximately 1.3 cm off the center and 5.3 cm from the lid of the cylinder. The spheres were filled with a ^{123}I solution, while the cylinder was filled with ^{99m}Tc solution. The activity of each source is shown in table 7.3. The phantom was positioned at the centre of the FOV for the acquisition. The shadowgrams and the spectra recorded from both detector are displayed in figure 7.22.

7.7 Results

The back-projection reconstruction has been applied to the shadowgrams from all the exposures. After the reconstruction, the CLEAN algorithm with a 2% gain has been applied to the images. In this study CLEAN was applied with a fixed number of iterations. The evaluation and implementation of an optimal stopping criterion

Isotope	Activity (MBq)	Acquisition time (s)	Detector counts	
			Detector 1	Detector 2
^{99m}Tc	0.82	3600	1.78 $\times 10^6$	1.49 $\times 10^6$
^{99m}Tc	0.19	21600	2.15$\times 10^6$	2.77$\times 10^6$
^{57}Co	0.20		3.36$\times 10^6$	2.22$\times 10^6$
^{99m}Tc	8.03	2700	5.35$\times 10^6$	4.22$\times 10^6$
^{123}I	6.5		2.61$\times 10^6$	2.21$\times 10^6$

TABLE 7.2: Isotopes and activity of the sources used for the point source imaging tests. The counts displayed in column 6 are relative to the energy band selected for each source

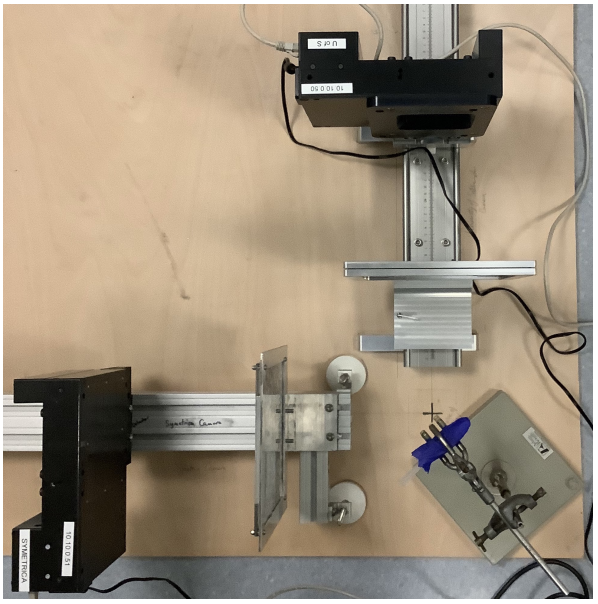

FIGURE 7.19: Photograph taken during the exposure with a cylindrical source of a ^{99m}Tc solution. In this acquisition, the source was placed horizontally at an angle of 45 degrees to both camera axes

for CLEAN is a topic that will be explored in a later study. The processed 3D images are presented in this section.

7.7.1 Point Sources

Single or multiple point sources represent an ideal scenario for the best performance of both coded apertures and CLEAN. The technique performed very similarly to

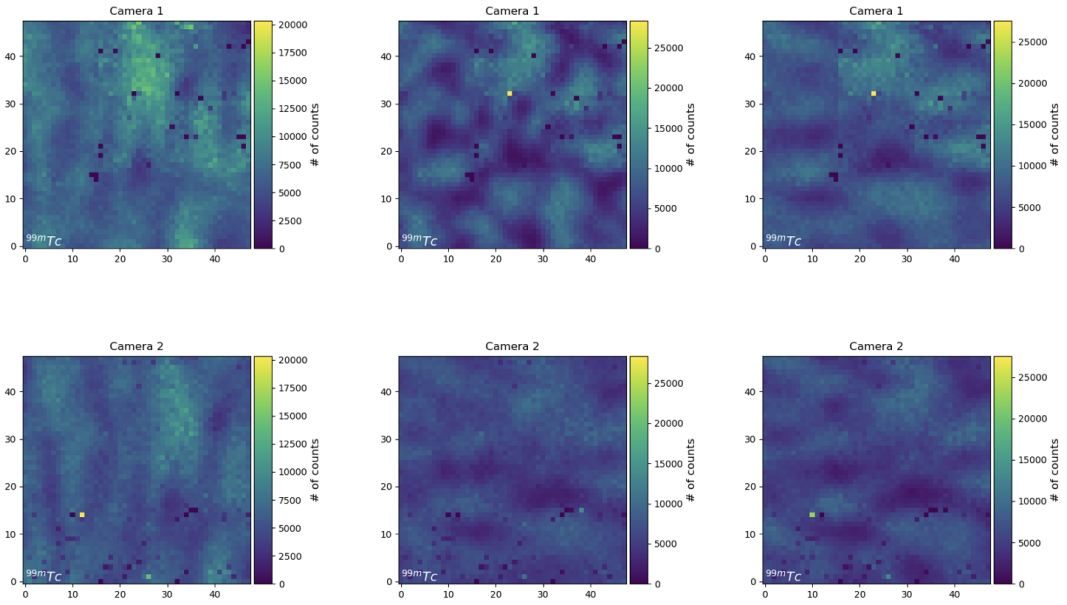

FIGURE 7.20: Shadowgrams of the ^{99m}Tc cylindrical source in 3 different configurations. Left: Vertical. Center: Parallel to the axis of camera 1. Right: at a 45 degrees angle to both camera axes. In each configuration, the source was placed at the centre of the FOV

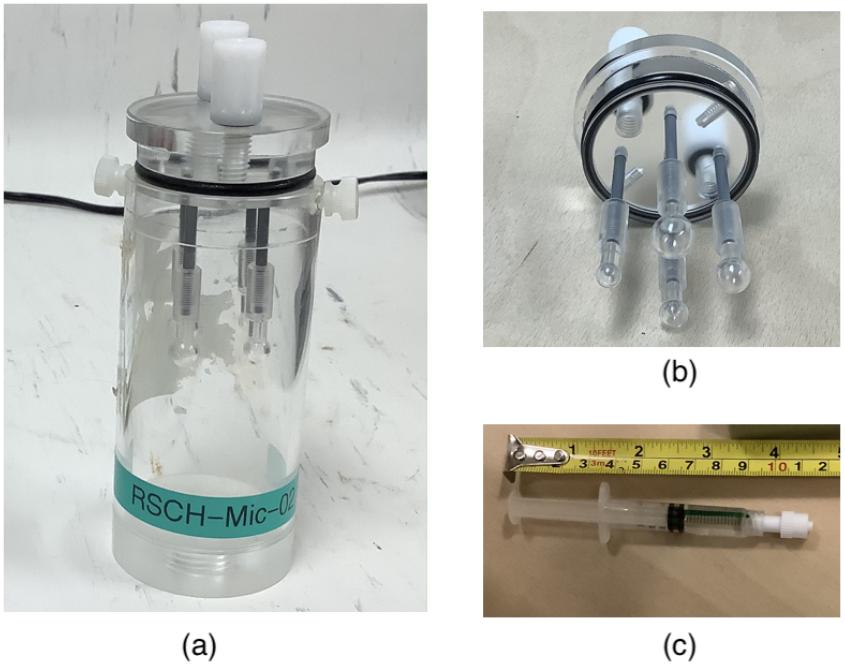

FIGURE 7.21: The extended sources used in the experiments. (a) The hollow sphere phantom. (b) The sphere components of the hollow sphere phantom. (c) A 5 ml syringe full of ^{99m}Tc solution (cylindrical source)

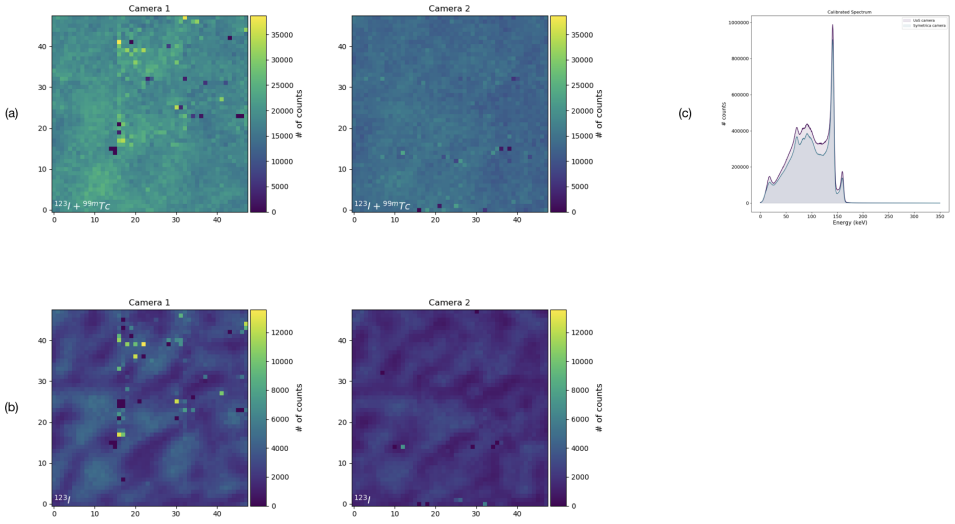

FIGURE 7.22: (a) Shadowgrams of the hollow sphere phantom in the energy windows 137 - 144 keV and 155 -162 keV. (b) Shadowgrams of the hollow sphere phantom in the energy window 155 -162 keV. (c) Spectra of the emission from the phantom recorded by both detectors

Source	Isotope	Activity(MBq)	Acquisition time (s)	Detector counts	
				Detector 1	Detector 2
Cylinder (vertical)	^{99m}Tc	34.46	900	16.60×10^6	13.64×10^6
Cylinder (horizontal)	^{99m}Tc	32.69	900	15.74×10^6	13.93×10^6
Cylinder (horizontal 2)	^{99m}Tc	30.92	900	17.43×10^6	13.17×10^6
Hollow spheres phantom	^{123}I	16.11	3600	4.42×10^6	6.78×10^6
	^{99m}Tc	71.96		37.48×10^6	26.75×10^6

TABLE 7.3: Sources, activity and acquisition times of extended source scans

what was predicted by the simulations in both cases. Figure 7.23 shows the raw images of all three point source configurations, along with the images after 50 and 300 CLEAN iterations. If only one source is present in the FOV, most of the background noise is suppressed after 50 iterations. In the images with two sources, significant background noise is still visible after 50 iterations, but after 300 CLEAN iterations only residuals from the elongated PSF of a single camera are still present in the image with an intensity of around 10% of the image peak. In both cases the advantage of using a dual-head system is visible: The addition of the second camera constrains the position of the point source. Adding a second source to the FOV makes CLEAN slower: in fact CLEAN will operate on both sources, subtracting components from one of them in each loop. In figure 7.23, images show that the ^{123}I point source is not clearly visible, in the raw image and in the image after 50 iterations and becomes distinguishable from the noise only after iteration 300. A quantitative intensity or source activity measurement was not attempted at this stage, but it is confirmed that

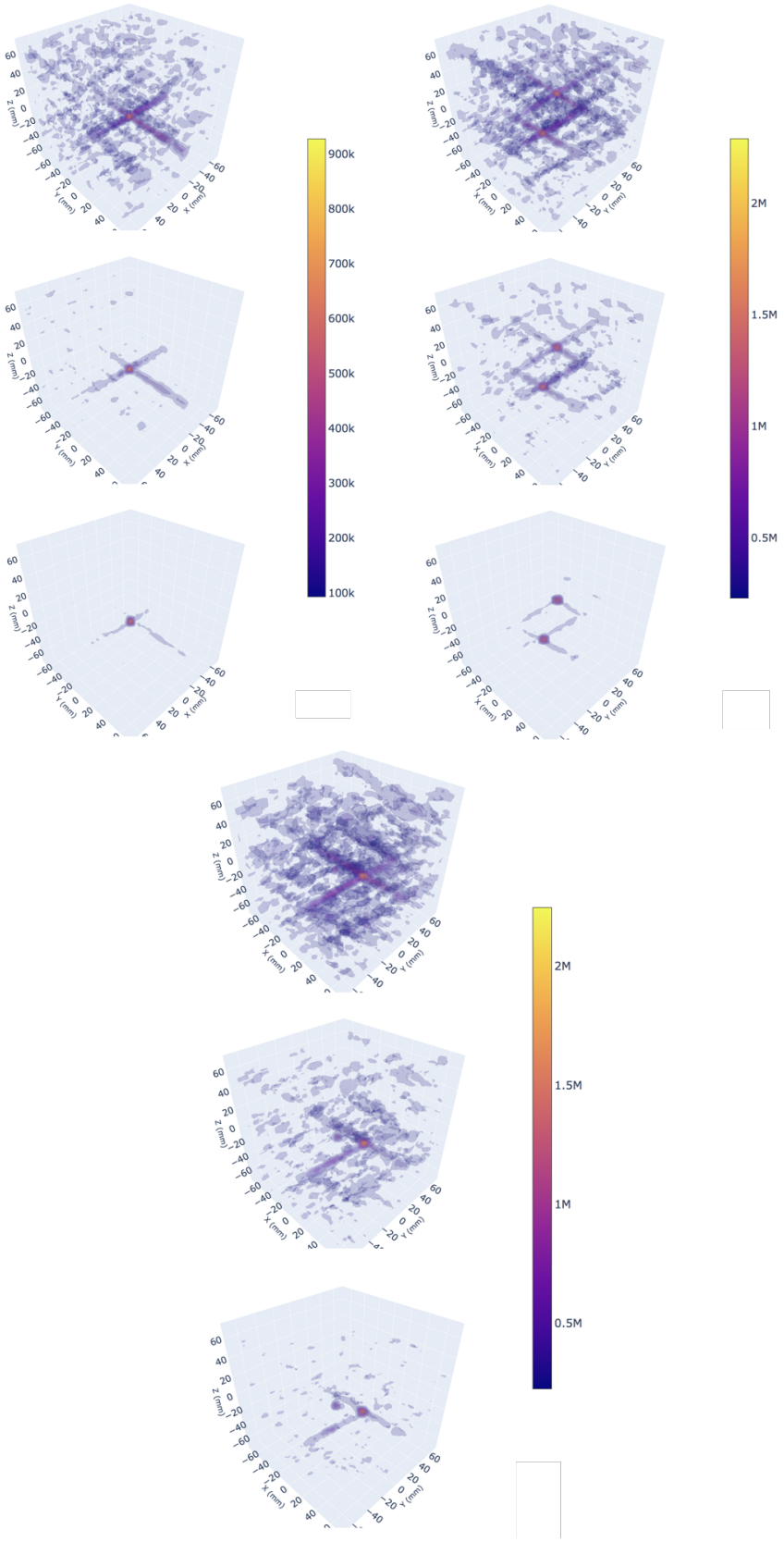

FIGURE 7.23: Top left: Images of a single point source of ^{99m}Tc. Top right: Image of ^{57}Co and a ^{99m}Tc point sources. Bottom: Image of ^{99m}Tc and a ^{123}I. In each case, the graphs display the raw image at the top, the cleaned image after 50 CLEAN iterations at the centre and after 300 CLEAN iterations at the bottom

the relative intensity of the sources is conserved after the application of CLEAN and for each image correctly corresponds to the detector counts. It should be pointed out that the peak value of the image is proportional to the total number of counts present in the shadowgram for each selected energy band. This depends, among other factors, on the distance of the source from each of the detector planes and a possible variation in detection efficiency of the instrument at different evergy. These effects are not taken into account in this study, but must be considered in order to perform an accurate activity measurement.

7.7.2 Extended Source

Figure 7.24 displays the 3D images of the cylindrical source. Each pair of plots shows the raw images before CLEAN was applied and the same images after 500 CLEAN iterations respectively at the top and bottom. While a hot region in the centre of the FOV is present in all three cases, the shape of the extended source is clearly recognisable only when the source was placed in vertical position, in the top left section of figure 7.24. This suggests that the deconvolution algorithm is not as effective in the reconstruction of sources that extend along one of the axes of the camera, which happens in the other configurations.

7.7.3 Hollow Sphere Phantom

Finally, the raw image of the hollow sphere phantom in the energy range $137 - 144$keV is presented in the top-left corner of figure 7.25. Figure 7.25 also shows the same image after 100 and 500 iterations of CLEAN respectively. After 100 iterations of CLEAN, most of the background noise was suppressed, with the exception of the residual extended shape from the PSF of the image of each sphere. While only the three bigger spheres were distinguishable in the raw image, applying CLEAN for 300 iterations made the smaller sphere distinguishable from the background in the cleaned image.

7.8 Computing Performance

The computing performance of back-projection can be divided in its main components: the back-projection itself and the CLEAN stage.

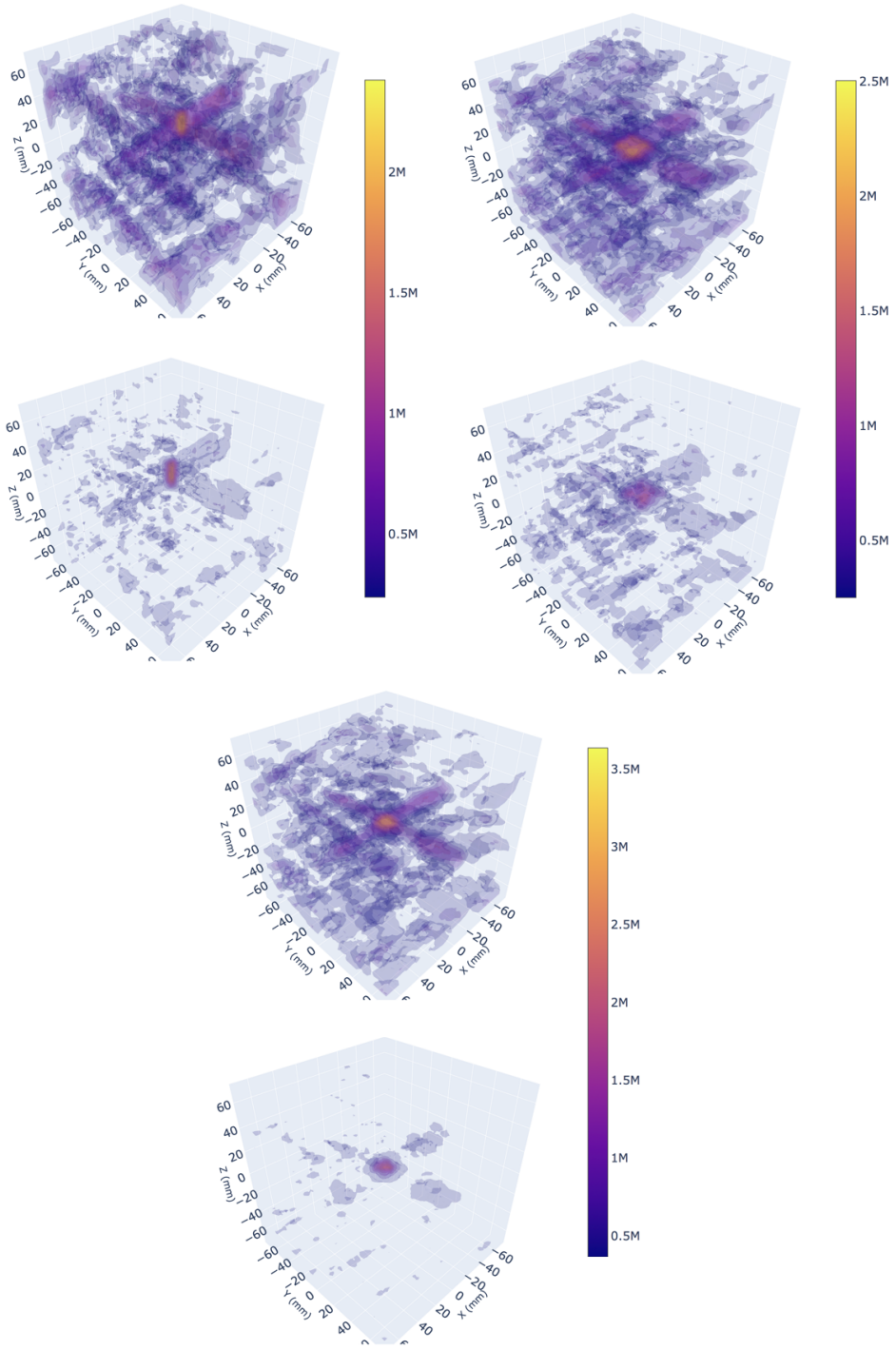

FIGURE 7.24: Images of the cylindrical source in configuration 1 (top left), configuration 2 (top right) and configuration 3 (bottom row). The raw images are shown at the top, while the images processed with CLEAN after 500 iterations are at bottom

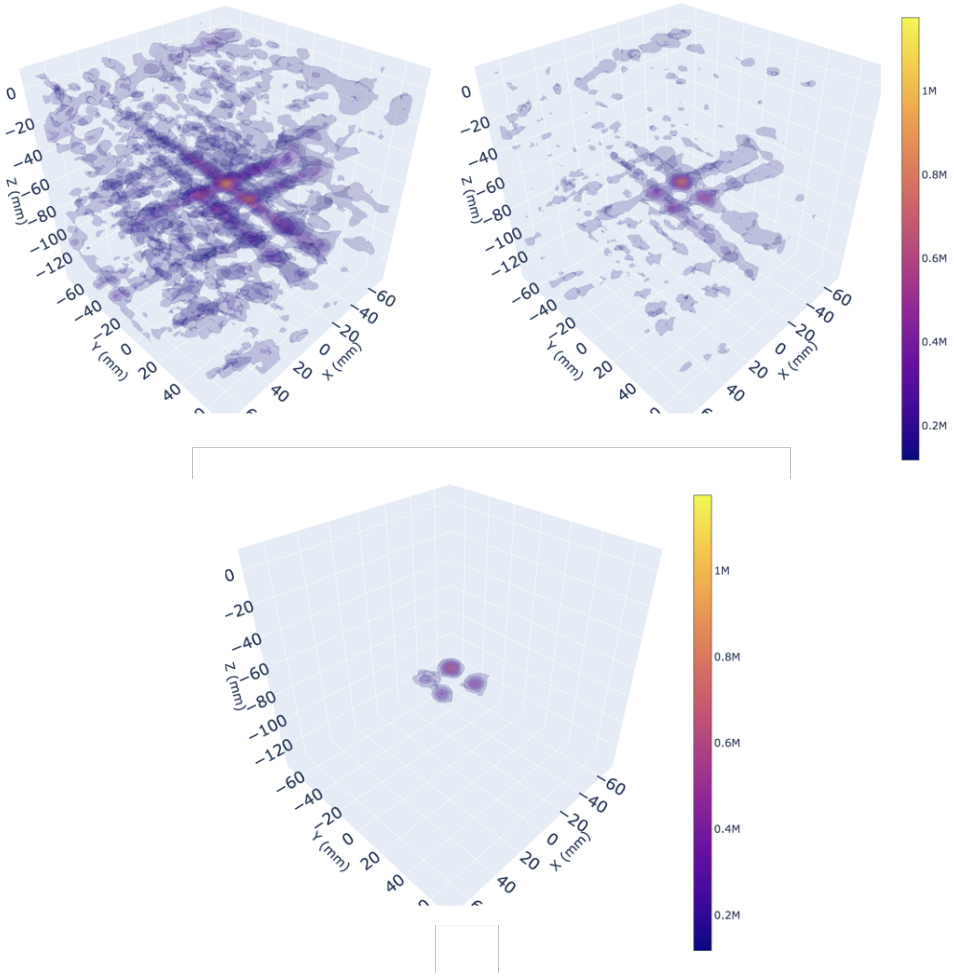

FIGURE 7.25: Top left: raw image of the hollow spheres phantom. Top right: image of the hollow spheres phantom after 100 CLEAN iterations. bottom: image of the hollow spheres phantom after 300 CLEAN iterations

7.8.1 Computing Performance of Back-projection

In this stage of the experiments the real-time capabilities of the reconstruction method have not been yet explored. In order to reduce the computing time to a minimum and focus on the imaging capabilities of the system in a static setting, data have not been recorded and processed photon-by-photon, but as a detector count histogram. All the photons detected in a single pixel have been processed at the same time, simply by multiplying the SPPs by the number of counts in each detector pixel before back-projection. The average time for the reconstruction of a single 3D image is around 50 seconds. This includes loading each SPP from memory and adding it to a running sum. It is estimated that around 65% of the processing time was employed to reading in the SPP, which are 72Mb for the whole field of view. The computing time for this method could therefore be improved massively by using a machine with a very large RAM, which could hold the SPPs necessary for back projection.

7.8.2 Computing Performance of CLEAN

From paragraph 7.8.1 it is clear that the factor that slows down the performance of CLEAN is the reconstruction of the ideal PSF for each possible source position. The reconstruction of the PSF requires the same computing time as the reconstruction of any other image. For this reason CLEAN stores the computed ideal PSFs in memory after computing them, to avoid computing them again in later iterations. When the PSFs are already in memory and CLEAN does not have to compute them on the fly, each iteration takes around 30ms, again mostly used to read in the pre-computed PSFs.

7.9 Conclusions

Chapters 5, 6 and 7 have demonstrated the application of a back-projection approach to near-field 3D imaging.

The design of the experiments was guided by the possibility to apply this technology to aid in the resolution of some challenges of current nuclear imaging techniques. The first challenge is imaging sources in the 3D space with a single view of the target. This would reduce the footprint of SPECT machine, which would not need to have a rotating gantry around the patient. The second improvement that could be brought forward is the development of lighter and possibly hand-held SPECT devices for diagnostics or surgical applications, as opposed to the current large and heavy SPECT machines. A version of a photon-by-photon approach like back projection would be the only way to apply coded aperture imaging to situations where the camera or the target of the observation is moving.

The images obtained in three different experimental settings indicate that the Dual-View Coded Aperture Mask camera and the back projection algorithm are indeed able to successfully reconstruct the shape and position of different types of sources in the 3D space with a single acquisition. However, there are areas that still need investigation to prove the suitability of the SPECT application of coded apertures and their potential to improve the performance of collimator scanners.

For example, it is well known that the performance of coded aperture images decreases if the source is extended, as a result of the multiplexing of the information performed by the mask, and in the limit where the source extends across the whole field of view, it can't be reconstructed(57). It is necessary to further explore the limits of the technique in terms of the size and morphology of the sources that can be detected with different families of mask pattern. On the other hand, it would be useful to narrow down the branches of Nuclear Imaging that would benefit from

the application of coded apertures, where it is likely to have small sources concentrated in a small volume and a high background. One of these applications, which has just started to be explored during this project, is parathyroid imaging for surgical applications. Parathyroids are four glands that are located behind the thyroid. Depending on the treatment plan, they may need to be removed or preserved during thyroid excision. Their identification is particularly difficult without nuclear medicine techniques, and almost impossible to be carried out during surgery(65). A system similar to 2V-CAM, for example, would be optimal to identify and preserve them during thyroid excision, improving the patients' outcome.

Another area that needs further investigation is the performance of the technique in terms of quantitative reconstruction of the activity of the source. Once again a problem that seems of straightforward resolution for point sources, is made much more complicated by the introduction of extended sources.

Finally, it is necessary once again to address the computing performance of back-projection. Although in theory able to produce real-time images as the camera or the patient are moving, the high resolution needed for medical applications poses a limit to how fast images can be processed. The problem is made worse by the 3D nature of the images with respect to the astronomy applications. It would be interesting to investigate whether the algorithm could be implemented more efficiently, in order to make real-time or near real-time imaging practicable. The imaging capabilities of coded masks have a great potential to make surgical probes, but real-time production of images is required for this application. Alternatively, other imaging methods should be explored, such as MLEM. G.Daniel also recently achieved coded aperture images of extended planar sources using artificial intelligence techniques(66).

The investigation of all the limitations of the method is fundamental to assess the areas of nuclear imaging where coded aperture could provide a breakthrough. This project, as well as the body of literature that preceded it, suggests that it seems unlikely that coded mask can offer versatility for a variety of SPECT applications the way that collimators do. However, for scenarios with a small concentrated sources and high background levels, the higher detection efficiency of codes mask translates to an improved imaging performance with a reduced instrument size with respect to currently used SPECT systems.

Chapter 8

Conclusions

This research has demonstrated the application of a new image reconstruction approach to coded-mask data in two very different fields: gamma-ray astronomy and nuclear imaging.

The first application has been the creation of a tool for image construction and flux measurements of images obtained with IBIS/ISGRI slew data, opening the the way for the analysis of 65Ms of observations which have never been processed before. An all-sky map with a prototype data set was produced with 150ks of observation carried out during a period of one month. Six sources were detected in the map with a source location accuracy estimated at 4.56 arcminutes. The faintest source detected in the all-sky slew map was MAXI J1659-152, which had an average flux of around 100 mCrab during the observation period. MAXI J1659-152 was detected at a 20.7σ significance with 6.6ks of observation. Pointing observations from the same period were used to cross-calibrate the method and extract count-rate measurements from slew observations. The quality of the calibration is affected by a high level of noise, which is partially due to the motion of the telescope axis and partially to the coding noise, not yet fully suppressed in the analysis process. Calibration with the current data set suggests that these effect combine to produce a factor of 0.24 between slews and pointings flux measurements, but further developments and a larger data set are needed to confirm these numbers.

The second application has been the development of 2V-CAM, a coded mask system for near-field 3D imaging, to be used in a medical setup and take advantage of the increased detection efficiency of coded masks with respect to collimators. Using a 3D version of the back-projection algorithm developed for astronomy, sources of different nature and made of different isotopes were imaged in a FOV of approximately $15 \times 15 \times 15$ cm^3. Multiple point sources were imaged successfully. 2V-CAM easily resolved small spherical sources 18mm apart, although the system has

been designed to provide 6mm resolution at the centre of the FOV. The biggest challenge encountered was the correct reconstruction of the morphology of an extended source, confirming that the high throughput of a coded mask system would be fully exploited for applications where a small FOV and high resolution are required, such as small animal studies or thyroid studies. A particularly attractive field of development lies in theranostics, where the low photon yield of alpha and beta emitters used for therapy could be very efficiently captured by coded mask systems. The tests have been carried out in a static setting, but a photon-by-photon approach like back-projection was applied because it presents the prospect to develop lightweight and potentially hand held SPECT systems. Such systems could lead the way for SPECT being used in ways never explored before, for example to aide tumor excision during surgical procedures or for real-time imaging. With this wide range of applications in mind, a lightweight, modular and versatile coded mask system was designed and assembled, that and can be easily modified and optimised for further studies in different directions.

References

tocchapterReferences

[1] R. A. Remillard and J. E. McClintock, "X-ray properties of black-hole binaries," *Annual Review of Astronomy and Astrophysics*, vol. 44, 2006.

[2] U. R. M. E. Geppert, "M. S. Longair,high energy astrophysics, vol. 1,particles photons and their detection, Cambridge University Press, Cambridge, 1992," *Astrophysics and Space Science*, vol. 201, no. 1, 1993.

[3] B. Banerjee, M. Joshi, P. Majumdar, K. E. Williamson, S. G. Jorstad, and A. P. Marscher, "Time-dependent spectral modelling of Markarian 421 during a violent outburst in 2010," *Monthly Notices of the Royal Astronomical Society*, vol. 487, no. 1, 2019.

[4] A. M. Levine, F. L. Lang, W. H. G. Lewin, F. A. Primini, C. A. Dobson, J. P. Doty, J. A. Hoffman, S. K. Howe, A. Scheepmaker, W. A. Wheaton, J. L. Matteson, W. A. Baity, D. E. Gruber, F. K. Knight, P. L. Nolan, R. M. Pelling, R. E. Rothschild, and L. E. Peterson, "The HEAO 1 A-4 catalog of high-energy X-ray sources," *The Astrophysical Journal Supplement Series*, vol. 54, 1984.

[5] S. S. Holt, "RESULTS FROM THE ARIEL 5 ALL-SKY MONITOR." *Proc R Soc London Ser A*, vol. 350, no. 1663, 1976.

[6] F. Jansen, D. Lumb, B. Altieri, J. Clavel, M. Ehle, C. Erd, C. Gabriel, M. Guainazzi, P. Gondoin, R. Much, R. Munoz, M. Santos, N. Schartel, D. Texier, and G. Vacanti, "XMM-Newton observatory. The spacecraft and operations," 2001.

[7] M. C. Weisskopf, B. Brinkman, C. Canizares, G. Garmire, S. Murray, and L. P. Van Speybroeck, " An Overview of the Performance and Scientific Results from the Chandra X-Ray Observatory ," *Publications of the Astronomical Society of the Pacific*, vol. 114, no. 791, 2002.

[8] W. Voges, B. Aschenbach, T. Boller, H. Bräuninger, U. Briel, W. Burkert, K. Dennerl, J. Englhauser, R. Gruber, F. Haberl, G. Hartner, G. Hasinger, M. Kürster, E. Pfeffermann, W. Pietsch, P. Predehl, C. Rosso, J. H. Schmitt, J. Trümper, and H. U. Zimmermann, "The ROSAT all-sky survey bright source catalogue," *Astronomy and Astrophysics*, vol. 349, no. 2, 1999.

[9] F. A. Harrison, W. W. Craig, F. E. Christensen, C. J. Hailey, W. W. Zhang, S. E. Boggs, D. Stern, W. R. Cook, K. Forster, P. Giommi, B. W. Grefenstette, Y. Kim, T. Kitaguchi, J. E. Koglin, K. K. Madsen, P. H. Mao, H. Miyasaka, K. Mori, M. Perri, M. J. Pivovaroff, S. Puccetti, V. R. Rana, N. J. Westergaard, J. Willis, A. Zoglauer, H. An, M. Bachetti, N. M. Barrière, E. C. Bellm, V. Bhalerao, N. F. Brejnholt, F. Fuerst, C. C. Liebe, C. B. Markwardt, M. Nynka, J. K. Vogel, D. J. Walton, D. R. Wik, D. M. Alexander, L. R. Cominsky, A. E. Hornschemeier, A. Hornstrup, V. M. Kaspi, G. M. Madejski, G. Matt, S. Molendi, D. M. Smith, J. A. Tomsick, M. Ajello, D. R. Ballantyne, M. Baloković, D. Barret, F. E. Bauer, R. D. Blandford, W. N. Brandt, L. W. Brenneman, J. Chiang, D. Chakrabarty, J. Chenevez, A. Comastri, F. Dufour, M. Elvis, A. C. Fabian, D. Farrah, C. L. Fryer, E. V. Gotthelf, J. E. Grindlay, D. J. Helfand, R. Krivonos, D. L. Meier, J. M. Miller, L. Natalucci, P. Ogle, E. O. Ofek, A. Ptak, S. P. Reynolds, J. R. Rigby, G. Tagliaferri, S. E. Thorsett, E. Treister, and C. M. Urry, "The Nuclear Spectroscopic Telescope Array (NuSTAR) high-energy X-ray mission," *Astrophysical Journal*, vol. 770, no. 2, 2013.

[10] M. Matsuoka, K. Kawasaki, S. Ueno, H. Tomida, M. Kohama, M. Suzuki, Y. Adachi, M. Ishikawa, T. Mihara, M. Sugizaki, N. Isobe, Y. Nakagawa, H. Tsunemi, E. Miyata, N. Kawai, J. Kataoka, M. Morii, A. Yoshida, H. Negoro, M. Nakajima, Y. Ueda, H. Chujo, K. Yamaoka, O. Yamazaki, S. Nakahira, T. You, R. Ishiwata, S. Miyoshi, S. Eguchi, K. Hiroi, H. Katayama, and K. Ebisawa, "The MAXI mission on the ISS: Science and instruments for monitoring All-sky X-ray Images," *Publications of the Astronomical Society of Japan*, vol. 61, no. 5, 2009.

[11] S. D. Barthelmy, L. M. Barbier, J. R. Cummings, E. E. Fenimore, N. Gehrels, D. Hullinger, H. A. Krimm, C. B. Markwardt, D. M. Palmer, A. Parsons, G. Sato, M. Suzuki, T. Takahashi, M. Tashiro, and J. Tueller, "The burst alert telescope (BAT) on the SWIFT midex mission," *Space Science Reviews*, vol. 120, no. 3-4, pp. 143–164, 12 2005.

[12] R. Terrier, F. Lebrun, A. Bazzano, G. Belanger, A. J. Bird, C. Blondel, P. David, P. Goldoni, A. Goldwurm, A. Gros, P. Laurent, G. Malaguti, A. Sauvageon, A. Segreto, and P. Ubertini, "In-flight calibration of the ISGRI camera," 11 2003.

[13] V. Bhalerao, D. Bhattacharya, A. Vibhute, P. Pawar, A. R. Rao, M. K. Hingar, R. Khanna, A. P. Kutty, J. P. Malkar, M. H. Patil, Y. K. Arora, S. Sinha, P. Priya, E. Samuel, S. Sreekumar, P. Vinod, N. P. Mithun, S. V. Vadawale, N. Vagshette, K. H. Navalgund, K. S. Sarma, R. Pandiyan, S. Seetha, and K. Subbarao, "The Cadmium Zinc Telluride Imager on AstroSat," 2017.

[14] W. B. Atwood, A. A. Abdo, M. Ackermann, W. Althouse, B. Anderson, M. Axelsson, L. Baldini, J. Ballet, D. L. Band, G. Barbiellini, J. Bartelt, D. Bastieri, B. M. Baughman, K. Bechtol, D. Bédérède, F. Bellardi, R. Bellazzini, B. Berenji, G. F. Bignami, D. Bisello, E. Bissaldi, R. D. Blandford, E. D. Bloom, J. R. Bogart, E. Bonamente, J. Bonnell, A. W. Borgland, A. Bouvier, J. Bregeon, A. Brez, M. Brigida, P. Bruel, T. H. Burnett, G. Busetto, G. A. Caliandro, R. A. Cameron, P. A. Caraveo, S. Carius, P. Carlson, J. M. Casandjian, E. Cavazzuti, M. Ceccanti, C. Cecchi, E. Charles, A. Chekhtman, C. C. Cheung, J. Chiang, R. Chipaux, A. N. Cillis, S. Ciprini, R. Claus, J. Cohen-Tanugi, S. Condamoor, J. Conrad, R. Corbet, L. Corucci, L. Costamante, S. Cutini, D. S. Davis, D. Decotigny, M. Deklotz, C. D. Dermer, A. De Angelis, S. W. Digel, E. Do Couto E Silva, P. S. Drell, R. Dubois, D. Dumora, Y. Edmonds, D. Fabiani, C. Farnier, C. Favuzzi, D. L. Flath, P. Fleury, W. B. Focke, S. Funk, P. Fusco, F. Gargano, D. Gasparrini, N. Gehrels, F. X. Gentit, S. Germani, B. Giebels, N. Giglietto, P. Giommi, F. Giordano, T. Glanzman, G. Godfrey, I. A. Grenier, M. H. Grondin, J. E. Grove, L. Guillemot, S. Guiriec, G. Haller, A. K. Harding, P. A. Hart, E. Hays, S. E. Healey, M. Hirayama, L. Hjalmarsdotter, R. Horn, R. E. Hughes, G. Jóhannesson, G. Johansson, A. S. Johnson, R. P. Johnson, T. J. Johnson, W. N. Johnson, T. Kamae, H. Katagiri, J. Kataoka, A. Kavelaars, N. Kawai, H. Kelly, M. Kerr, W. Klamra, J. Knödlseder, M. L. Kocian, N. Komin, F. Kuehn, M. Kuss, D. Landriu, L. Latronico, B. Lee, S. H. Lee, M. Lemoine-Goumard, A. M. Lionetto, F. Longo, F. Loparco, B. Lott, M. N. Lovellette, P. Lubrano, G. M. Madejski, A. Makeev, B. Marangelli, M. M. Massai, M. N. Mazziotta, J. E. McEnery, N. Menon, C. Meurer, P. F. Michelson, M. Minuti, N. Mirizzi, W. Mitthumsiri, T. Mizuno, A. A. Moiseev, C. Monte, M. E. Monzani, E. Moretti, A. Morselli, I. V. Moskalenko, S. Murgia, T. Nakamori, S. Nishino, P. L. Nolan, J. P. Norris, E. Nuss, M. Ohno, T. Ohsugi, N. Omodei, E. Orlando, J. F. Ormes, A. Paccagnella, D. Paneque, J. H. Panetta, D. Parent, M. Pearce, M. Pepe, A. Perazzo, M. Pesce-Rollins, P. Picozza, L. Pieri, M. Pinchera, F. Piron, T. A. Porter, L. Poupard, S. Rainò, R. Rando, E. Rapposelli, M. Razzano, A. Reimer, O. Reimer, T. Reposeur, L. C. Reyes, S. Ritz, L. S. Rochester, A. Y. Rodriguez, R. W. Romani, M. Roth, J. J. Russell, F. Ryde, S. Sabatini, H. F. Sadrozinski, D. Sanchez, A. Sander, L. Sapozhnikov, P. M. Parkinson, J. D. Scargle, T. L. Schalk, G. Scolieri, C. Sgrò, G. H. Share, M. Shaw, T. Shimokawabe, C. Shrader, A. Sierpowska-Bartosik, E. J. Siskind, D. A. Smith, P. D. Smith, G. Spandre,

P. Spinelli, J. L. Starck, T. E. Stephens, M. S. Strickman, A. W. Strong, D. J. Suson, H. Tajima, H. Takahashi, T. Takahashi, T. Tanaka, A. Tenze, S. Tether, J. B. Thayer, J. G. Thayer, D. J. Thompson, L. Tibaldo, O. Tibolla, D. F. Torres, G. Tosti, A. Tramacere, M. Turri, T. L. Usher, N. Vilchez, V. Vitale, P. Wang, K. Watters, B. L. Winer, K. S. Wood, T. Ylinen, and M. Ziegler, "The large area telescope on the Fermi gamma-ray space telescope mission," *Astrophysical Journal*, vol. 697, no. 2, 2009.

[15] F. Aharonian, J. Buckley, T. Kifune, and G. Sinnis, "High energy astrophysics with ground-based gamma ray detectors," *Reports on Progress in Physics*, vol. 71, no. 9, 2008.

[16] R. H. Dicke, "Scatter-Hole Cameras for X-Rays and Gamma Rays," *The Astrophysical Journal*, vol. 153, p. L101, 8 1968.

[17] E. E. Fenimore and T. M. Cannon, "Coded aperture imaging with uniformly redundant arrays," *Applied Optics*, vol. 17, no. 3, p. 337, 2 1978.

[18] E. Caroli, J. B. Stephen, G. Di Cocco, L. Natalucci, and A. Spizzichino, "Coded aperture imaging in X- and gamma-ray astronomy," *Space Science Reviews*, vol. 45, no. 3-4, 1987.

[19] P. M. Charalambous, A. J. Dean, J. B. Stephen, and N. G. S. Young, "Aberrations in gamma-ray coded aperture imaging," *Applied Optics*, vol. 23, no. 22, 1984.

[20] "Mission Information." [Online]. Available: MissionInformation

[21] L. E. Kopilovich, "Construction of nonredundant masks over square grids using difference sets," *Optics Communications*, vol. 68, no. 1, 1988.

[22] E. Moore and H. Pollatsek, "Difference Sets. Connecting Algebra, Combinatorics, and Geometry," 2013.

[23] R. Gottesman, Stephen and E. Fenimore, Edward, "New family of binary arrays for coded aperture imaging," *Applied Optics*, vol. 28, no. 20, pp. 4344–4352, 1989.

[24] G. Vedrenne, J. P. Roques, V. Schönfelder, P. Mandrou, G. G. Lichit, A. Von Kienlin, B. Cordier, S. Schanne, J. Knödlseder, G. Skinner, P. Jean, F. Sanchez, P. Caraveo, B. Teegarden, P. Von Ballmoos, L. Bouchet, P. Paul, J. Matteson, S. Boggs, C. Wunderer, P. Leleux, G. Weidenspointner, P. Durouchoux, R. Diehl, A. Strong, M. Cassé, M. A. Clair, and Y. André, "SPI: The spectrometer aboard INTEGRAL," *Astronomy and Astrophysics*, vol. 411, no. 1, 2003.

[25] Chernyakova M., Neronov A., Pavan L., and Turler M., *IBIS Analysis User Manual*, 2015.

[26] A. Goldwurm, P. David, L. Foschini, A. Gros, P. Laurent, A. Sauvageon, A. J. Bird, L. Lerusse, and N. Produit, "The INTEGRAL/IBIS scientific data analysis," *Astronomy and Astrophysics*, vol. 411, no. 1, 11 2003.

[27] P. L. Jensen, K. Clausen, C. Cassi, F. Ravera, G. Janin, C. Winkler, and R. Much, "The INTEGRAL spacecraft - In-orbit performance," *Astronomy and Astrophysics*, vol. 411, no. 1, 2003.

[28] M. Chernyakova, A. Frankowski, L. Pavan, and M. Turler, "Introduction to the INTEGRAL Data Analysis," INTEGRAL Science Data Centre, Tech. Rep., 2020.

[29] Z. Mu, L. W. Dobrucki, and Y. H. Liu, "SPECT imaging of 2-D and 3-D distributed sources with near-field coded aperture collimation: Computer simulation and real data validation," *Journal of Medical and Biological Engineering*, vol. 36, no. 1, 2016.

[30] P. Barr, L. Bassani, and A. Bazzano, "IBIS Observer's Manual ," Tech. Rep., 2021.

[31] "INTEGRAL Science Data Centre (ISDC) - https://www.isdc.unige.ch/integral/ osa/11.2/issues_osa." [Online]. Available: https://www.isdc.unige.ch/integral/osa/11.2/issues_osa

[32] E. E. Fenimore, "Time-resolved and energy-resolved coded aperture images with URA tagging," *Applied Optics*, vol. 26, no. 14, 1987.

[33] R. Mukherjee, D. L. Bertsch, S. D. Bloom, B. L. Dingus, J. A. Esposito, C. E. Fichtel, R. C. Hartman, S. D. Hunter, G. Kanbach, D. A. Kniffen, Y. C. Lin, H. A. Mayer-Hasselwander, L. M. McDonald, P. F. Michelson, C. von Montigny, A. Mucke, P. L. Nolan, M. Pohl, O. Reimer, E. Schneid, P. Sreekumar, and D. J. Thompson, "EGRET Observations of High-Energy Gamma-Ray Emission from Blazars: An Update," *The Astrophysical Journal*, vol. 490, no. 1, 1997.

[34] "Modified Julian Dates - https://core2.gsfc.nasa.gov/time/."

[35] A. Costantino and A. J. Bird, "Constructing an IBIS/ISGRI slew survey," in *Memorie della Societa Astronomica Italiana - Journal of the Italian Astronomical Society*, vol. 90, no. 1-2. Societa Astronomica Italiana, 2019, pp. 107–109.

[36] A. Jimenez, "INTEGRAL Announcement of Opportunity for AO-15 Cycle Observation Proposals," 2015. [Online]. Available: https://www.cosmos.esa.int/web/integral/ao15

[37] A. J. Bird, A. Bazzano, L. Bassani, F. Capitanio, M. Fiocchi, A. B. Hill, A. Malizia, V. A. McBride, S. Scaringi, V. Sguera, J. B. Stephen, P. Ubertini, A. J. Dean, F. Lebrun, R. Terrier, M. Renaud, F. Mattana, D. Götz, J. Rodriguez, G. Belanger,

R. Walter, and C. Winkler, "The fourth ibis/isgri soft gamma-ray survey catalog," *Astrophysical Journal, Supplement Series*, vol. 186, no. 1, 2010.

[38] A. J. Bird, A. Bazzano, A. Malizia, M. Fiocchi, V. Sguera, L. Bassani, A. B. Hill, P. Ubertini, and C. Winkler, " THE IBIS SOFT GAMMA-RAY SKY AFTER 1000 INTEGRAL ORBITS ," *The Astrophysical Journal Supplement Series*, vol. 223, no. 1, 2016.

[39] A. Gros, A. Goldwurm, M. Cadolle-Bel, P. Goldoni, J. Rodriguez, L. Foschini, M. Del Santo, and P. Blay, "The INTEGRAL IBIS/ISGRI System Point Spread Function and Source Location Accuracy," *Astronomy and Astrophysics*, vol. 411, no. 1, 2003.

[40] S. Scaringi, A. J. Bird, A. B. Hill, D. J. Clark, V. A. McBride, A. J. Dean, A. Bazzano, L. Natalucci, and J. B. Stephen, "A new determination of the INTEGRAL/IBIS point source location accuracy," *Astronomy and Astrophysics*, vol. 516, no. 22, 2010.

[41] A. J. Bird, E. J. Barlow, L. Bassani, A. Bazzano, G. Belanger, A. Bodaghee, F. Capitanio, A. J. Dean, M. Fiocchi, A. B. Hill, F. Lebrun, A. Malizia, J. M. Mas-Hesse, M. Molina, L. Moran, M. Renaud, V. Sguera, S. E. Shaw, J. B. Stephen, R. Terrier, P. Ubertini, R. Walter, D. R. Willis, and C. Winkler, "The Second IBIS/ISGRI Soft Gamma-Ray Survey Catalog," *The Astrophysical Journal*, vol. 636, no. 2, 2006.

[42] "Patient Dose Information: Guidance," 2008.

[43] L. M. Davis, A. L. Smith, M. D. Aldridge, J. Foulkes, C. Peet, S. Wan, J. E. Gains, J. B. Bomanji, and M. N. Gaze, "Personalisation of molecular radiotherapy through optimisation of theragnostics," 2020.

[44] "Symbia Intevo (Product page) - https://www.siemens-healthineers.com/en-uk/molecular-imaging/xspect/symbia-intevo-bold." [Online]. Available: https://www.siemens-healthineers.com/en-uk/molecular-imaging/xspect/symbia-intevo-bold

[45] M. N. Wernick and J. N. Aarsvold, *Emission Tomography: The Fundamentals of PET and SPECT*, 2004.

[46] A. Seret and F. Bleeser, "Intrinsic uniformity requirements for pinhole SPECT," *Journal of Nuclear Medicine Technology*, vol. 34, no. 1, 2006.

[47] P. M. Wanet, A. Sand, and J. Abramovici, "Physical and clinical evaluation of high-resolution thyroid pinhole tomography," *Journal of Nuclear Medicine*, vol. 37, no. 12, 1996.

[48] E. Miot-Noirault, A. Vidal, P. Auzeloux, J. C. Madelmont, J. Maublant, and N. Moins, "First in vivo SPECT imaging of mouse femorotibial cartilage using 99mTc-NTP 15-5," *Molecular Imaging*, vol. 7, no. 6, 2008.

[49] S. Cherry, J. Sorenson, and M. Phelps, *Physics in Nuclear Medicine*, 2012.

[50] J. T. Bushberg, J. A. Seibert, E. M. Leidholdt, J. M. Boone, and E. J. Goldschmidt, "The Essential Physics of Medical Imaging," *Medical Physics*, vol. 30, no. 7, 2003.

[51] Z. Mu, B. Hong, S. Li, and Y. H. Liu, "A novel three-dimensional image reconstruction method for near-field coded aperture single photon emission computerized tomography," *Medical Physics*, vol. 36, no. 5, 2009.

[52] Z. Mu, L. W. Dobrucki, and Y. H. Liu, "SPECT imaging of 2-D and 3-D distributed sources with near-field coded aperture collimation: Computer simulation and real data validation," *Journal of Medical and Biological Engineering*, vol. 36, no. 1, 2016.

[53] H. H. Barrett, D. T. Wilson, and G. D. Demeester, "The use of half-tone screens in Fresnel zone plate imaging of incoherent sources," *Optics Communications*, vol. 5, no. 5, 1972.

[54] L. T. Chang, S. N. Kaplan, B. Macdonald, V. Perez-Mendez, and L. Shiraishi, "A method of tomographic imaging using a multiple pinhole coded aperture," *Journal of Nuclear Medicine*, vol. 15, no. 11, 1974.

[55] K. F. Koral, J. E. Freitas, W. L. Rogers, and J. W. Keyes, "Thyroid scintigraphy with time-coded aperture," *Journal of Nuclear Medicine*, vol. 20, no. 4, 1979.

[56] W. L. Rogers, K. F. Koral, R. Mayans, P. F. Leonard, J. H. Thrall, T. J. Brady, and J. W. Keyes, "Coded-aperture imaging of the heart," *Journal of Nuclear Medicine*, vol. 21, no. 4, 1980.

[57] R. Accorsi, F. Gasparini, and R. C. Lanza, "A coded aperture for high-resolution nuclear medicine planar imaging with a conventional anger camera: Experimental results," *IEEE Transactions on Nuclear Science*, vol. 48, no. 6 III, 2001.

[58] D. Schellingerhout, R. Accorsi, U. Mahmood, J. Idoine, R. C. Lanza, and R. Weissleder, "Coded aperture nuclear scintigraphy: A novel small animal imaging technique," *Molecular Imaging*, vol. 1, no. 4, 2002.

[59] M. Alnafea, K. Wells, N. M. Spyrou, and M. Guy, "Preliminary Monte Carlo study of coded aperture imaging with a CZT gamma camera system for scintimammography," *Nuclear Instruments and Methods in Physics Research, Section A: Accelerators, Spectrometers, Detectors and Associated Equipment*, vol. 573, no. 1-2, 2007.

[60] A. Mahl, B. Miller, M. Miften, and B. L. Jones, "Optimizing Coded Aperture Imaging techniques to allow for online tracking of fiducial markers with high-energy scattered radiation from treatment beam," *Medical Physics*, vol. 47, no. 9, 2020.

[61] R. Accorsi, "Design of near-field coded aperture cameras for high-resolution medical and industrial gamma-ray imaging," *Mit*, 2001.

[62] J. A. Högbom, "APERTURE SYNTHESIS WITH A NON-REGULAR DISTRIBUTION OF INTERFEROMETER BASELINES JA HOG-BOM," *Astronomy and Astrophysics Supplement Series*, 1974. [Online]. Available: http://adsabs.harvard.edu/full/1974A%26AS...15..417Hfile:///Users/aaronew/Dropbox/Papers/Articles/1974/Hogbom/AstronomyandAstrophysicsSupplementSeries1974Hogbom.pdfpapers2://publication/uuid/A7771835-03E0-48B9-A596-4D84D237575B

[63] K. Byard, "Application of the CLEAN algorithm to three dimensional coded aperture imaging," *Nuclear Instruments and Methods in Physics Research, Section A: Accelerators, Spectrometers, Detectors and Associated Equipment*, vol. 986, 2021.

[64] "IDEAS CZT Gamma camera - https://ideas.no/products/gamma-spect-2x2/." [Online]. Available: https://ideas.no/products/gamma-spect-2x2/

[65] E. Hindié, Ugur, D. Fuster, M. O'Doherty, G. Grassetto, P. Ureña, A. Kettle, S. A. Gulec, F. Pons, and D. Rubello, "2009 EANM parathyroid guidelines," 2009.

[66] G. Daniel and O. Limousin, "Extended sources reconstructions by means of coded mask aperture systems and deep learning algorithm," *Nuclear Instruments and Methods in Physics Research, Section A: Accelerators, Spectrometers, Detectors and Associated Equipment*, vol. 1012, 2021.